

**An X-ray diffraction investigation of the charge
density wave transition at the NbSe₂ surface**

Dissertation
zur Erlangung des Doktorgrades
der Mathematisch-Naturwissenschaftlichen Fakultät
der Christian-Albrechts-Universität
zu Kiel

vorgelegt von

Bridget M. Murphy

Kiel 2003

Referent: Prof. Dr. W. Press
Korreferent: Prof. Dr. W. Depmeier
Tag der mündlichen Prüfung: 17. Februar 2004
Zum Druck genehmigt:

Prof. Dr. W. Depmeier
Dekan

Abstract

Niobium diselenide 2H-NbSe₂ is a van der Waals bonded layered structure, which undergoes a charge density wave transition. We have investigated the charge density wave transition in NbSe₂ using grazing incidence X-ray diffraction. The evolution of a satellite reflection associated with the charge density wave has been observed above and below the critical angle of total external reflection in order to carry out a direct comparison between the surface and bulk behaviour. We successfully isolated the surface charge density wave structure on a high quality single crystal. The central finding of this thesis is that the behaviour of the surface charge density wave satellite differs from that in the bulk: At the surface, the charge density wave transition occurs at a higher temperature than in the bulk; also, the transition appears to be continuous. It is likely that we observe the unusual case defined as a “surface transition” and not the usual case of an “ordinary transition”.

The critical exponents for the surface sensitive and the bulk geometry have been determined from the X-ray diffraction data. The exponents are consistent with the occurrence of a continuous phase transition at the surface and in the case of the bulk a second order or very near second order phase transition in the bulk.

A novel experimental method, grazing incidence inelastic X-ray scattering, has been demonstrated. A first successful experiment on 2H-NbSe₂ where surface phonons are measured is reported.

Zusammenfassung

Niob-Diselenid $2H-NbSe_2$ ist ein van-der-Waals gebundener Schichtkristall mit einem Ladungsdichtewellen-Phasenübergang. In Rahmen dieser Arbeit wurde dieser Phasenübergang mittels Röntgenbeugung unter streifendem Einfall untersucht. Um direkt das Verhalten im Volumen und an der Oberfläche vergleichen zu können, wurde die temperaturabhängige Intensität eines Satellitenreflexes der Ladungsdichtewellen-Phase ober- und unterhalb des kritischen Winkels für externe Totalreflexion der Röntgenstrahlung gemessen. Die Ladungsdichtewellen-Struktur konnte erfolgreich bei einem Einkristall hoher Qualität isoliert werden. Das wichtigste Ergebnis dieser Arbeit ist der gefundene Unterschied des Ladungsdichtewellen-Übergangs im Volumen und an der Oberfläche: An der Oberfläche tritt der Phasenübergang bei einer höheren Temperatur als im Volumen auf; außerdem ist der Übergang offenbar kontinuierlich. Es ist sehr wahrscheinlich, daß der seltene Fall eines sogenannten „Oberflächen-Übergangs“ vorliegt und nicht der übliche Fall eines „gewöhnlichen Übergangs“.

Aus den Röntgenstreudaten wurden weiter kritische Exponenten für den Phasenübergang bestimmt. Die Exponenten sind in Übereinstimmung mit einem kontinuierlichen Phasenübergang an der Oberfläche und einem Übergang 2. Ordnung oder nahe 2. Ordnung im Volumen.

Schließlich wird in dieser Arbeit eine neuartige experimentelle Methode, inelastische Röntgenstreuung unter streifendem Einfall, vorgestellt. In einem ersten erfolgreichen Experiment an $NbSe_2$ wurden Oberflächen-Phononen gemessen.

Contents

1	Introduction	1
2	Structure and properties of layered crystals	5
2.1	NbSe ₂ – a layered crystal.....	5
2.2	Charge density waves	7
2.3	Previous NbSe ₂ studies.....	9
3	Theory of phase transitions	13
3.1	Introduction to Phase transitions	13
3.2	Thermodynamics of Phase transitions	14
3.3	Classes of phase transitions	16
3.4	Landau theory	17
3.5	Universality	20
3.6	Mean Field theory	21
3.7	Ising Model.....	22
3.8	Critical phenomena at surfaces	24
4	Theory of X-ray diffraction	32
4.1	X-ray diffraction	32
4.2	Bragg diffraction	33
4.3	Scattering from atoms and three-dimensional crystals	34
4.4	Surface X-ray diffraction	38
4.5	Reflectivity	40
4.6	Grazing incidence diffraction.....	42
5	Experimental set-up	45
5.1	Introduction	45
5.2	Sample preparation.....	45
5.3	Cryogenic temperatures.....	46
5.4	Laboratory X-ray sources	48
5.5	Synchrotron radiation	48
5.6	XMaS	49
5.7	BW2	50
5.8	ID1	53

6	Experiments and analysis	57
6.1	Introduction	57
6.2	Samples	57
6.3	Sample characterisation	59
6.4	Data from BW2.....	62
6.5	Ultra high vacuum preparation.....	63
6.6	Data from BW2: Further GID measurements	64
6.7	ID1	73
6.8	Discussion.....	83
6.9	Summary	88
7	Grazing incidence Inelastic X-ray scattering	91
7.1	X-ray diffraction	91
7.2	Experimental method	93
7.3	Results	95
8	Conclusions and outlook	97
	References	101

1 Introduction

There is considerable interest in low-dimensional materials in solid state physics. The reason for this is that reduced dimensionality has an influence on the electronic properties of a solid. In addition to designed systems such as heterostructures of binary and ternary III/V- semiconductors, natural layered crystals play an important role. Examples of such layered materials are graphite as well as the high temperature superconductors and the group of transition metal dichalcogenides.

The transition metal dichalcogenide family ranges from semiconductors through semimetals to metals. They exhibit fascinating properties due to their van der Waals bonded layered structure; particularly they display a quasi two-dimensional behaviour. Many of the metallic layered compounds exhibit charge density wave (CDW) instabilities^{1,2,3}. The conduction electrons play a central role in these changes of the electronic properties which show similarity with a Peierls transition. In recent years there has been intensive activity in the area of low-dimensional systems due to their special electronic properties and the possibility of intercalating other atoms into the layers. In particular there is great interest in this family of materials in the field of photoemission and other spectroscopic methods as they have such an interesting electronic structure^{4,5,6} and since simply by cleaving a clean surface may be obtained. The geometric structure is equally of great interest: scanning tunnelling microscopy, other microscopy techniques and also neutron and X-ray scattering methods are used to gain an insight into the properties of these materials. Indeed, the topic is the theme of an interdisciplinary experimental and theoretical DFG "Forschergruppe" at Kiel university investigating the structural and electronic properties of layered compounds using a range of techniques. The grazing incidence X-ray diffraction study (GID) of 2H-NbSe₂ at the charge density wave transition presented in this thesis has been carried out within the framework of this "Forschergruppe".

The physics of phase transitions is an extremely interesting area, especially for layered crystals where one might expect low dimensionality to play a dominant role in the critical behaviour at the phase transition. X-ray elastic diffraction provides

information on the structure of materials. By monitoring the diffraction from a sample while varying temperature it is possible to investigate the temperature dependence of a material structure and relate this to the phase transition physics. Many bulk X-ray and neutron scattering studies of phase transitions have been carried out on layered materials, hence there is a depth of knowledge available in this area (see for example Refs. 1, 3, 7, 8, 78, 95).

The role of a surface in continuous phase transitions has been described in detail by theoreticians such as S. Dietrich and H. Wagner⁹, H. W. Diehl¹⁰, K. Binder¹¹ and others. Recently much theoretical work has been devoted to the behaviour at the surface very close to the transition temperature such as the studies of D. P. Landau and K. Binder¹² and A. Milchev *et al.*¹³. Comparatively little experimental work has been done on the role of the surface. Using GID, i.e. maintaining an incidence angle below that of the angle of total external reflection, it is possible to restrict the penetration depth of the X-ray beam into the sample to $\sim 30 \text{ \AA}$ (e.g. Ref. 14). Depth-sensitive measurements are possible by carefully varying the angle of incidence of the incoming X-ray beam. Zhu *et al.*⁸ carried out such a GID experiment on the CDW transition at the charge density wave material $\text{K}_{0.3}\text{MoO}_3$ (blue bronze) surface. However, they did not observe modified behaviour at the surface and postulated that this was due to the existence of weak coupling perpendicular to the $(20\bar{1})$ surface. In many other systems surface effects have been observed. Burandt *et al.*¹⁵ found a modified surface behaviour at the NH_4Br surface. In 1997 Reichert *et al.* reported surface-induced anisotropy in Cu_3Au ¹⁶ and more recently determined the long-range order for the same system also by GID.¹⁷ In 2003, again using grazing incidence diffraction, they observed that the short range order in Cu_3Au was modified with respect to the bulk behaviour.¹⁸

For a charge density wave system, in order to understand the dynamical behaviour at the surface, it is also important to consider lattice vibrations and the role of phonon-phonon interactions and that of phonon-electron interactions. A novel X-ray scattering method to probe the surface phonons is presented in this thesis.

In particular, this study is focused on the transition metal dichalcogenide 2H-NbSe_2 , a layered structure with a hexagonal symmetry, space group $\text{P6}_3/\text{mmc}$, with lattice constants $a = 3.443 \text{ \AA}$ and $c = 12.547 \text{ \AA}$.¹⁹ Previous studies have shown that NbSe_2 undergoes a second order phase transition, within experimental accuracy, to a charge density wave structure^{1,3}. The presence of a CDW below 33.3 K, with a hexagonal superstructure, was reported by Moncton *et al.* in 1975 using neutron scattering.¹ The crystal lattice modification that occurs is fundamental to the transition, as the facilitating motion of the ions in the form of an accompanying phonon mode reduces the Coulomb energy of the CDW. This modification in association with the CDW is

evidence of strong electron-phonon coupling. Due to a linear coupling between the lattice and the charge density wave, a lattice distortion develops, the amplitude of which is proportional to the order parameter of the transition¹. Moncton *et al.* showed the CDW to be incommensurate down to $T = 0$ K. A superconducting transition occurs at $T = 7.2$ K²⁰.

The properties of the layered crystal niobium diselenide are presented in detail in chapter 2. The theory of phase transitions and their classifications are discussed in chapter 3. Particular attention is devoted to the occurrence of a surface phase transition in this $\frac{1}{2}$ - ∞ system. In this work the method of grazing incidence diffraction is employed to investigate the nature of the CDW phase transition at the surface of the material and to compare this behaviour to that of the bulk. We measure and characterise the CDW satellite peaks at the phase transition in order to carry out a direct comparison between the surface and bulk behaviour. Diffraction techniques are introduced in chapter 4 and the detailed description of the experiments carried out at Kiel and at the HASYLAB and ESRF synchrotron sources is presented in chapter 5. The experimental data are presented in chapter 6 along with the data analysis. The relevance of these results is also discussed. A recently performed novel experiment where inelastic X-ray scattering was carried out at the surface of NbSe₂ is outlined and the preliminary results are presented in chapter 7. In the concluding chapter the impact of the work is considered and future prospects in this area are put forward.

2 Structure and properties of layered crystals

2.1 NbSe₂ – a layered crystal

The TX₂ dichalcogenides have been largely studied for about 40 years. These layered crystals can be synthesised to form highly anisotropic compounds. While inside each layer strong ionic and covalent bonding predominates, weak van der Waals forces act between adjacent layers. The layered transition metal dichalcogenides exhibit fascinating properties due to their van der Waals bonded layered structure: superconducting behaviour, nonlinear and anisotropic electrical properties, gigantic dielectric constants, charge density wave (CDW) instabilities and a wealth of dynamical behaviour. NbSe₂ is a member of this group of materials, with T = Nb and X = Se. The coordination around T is either trigonal prismatic or octahedral.

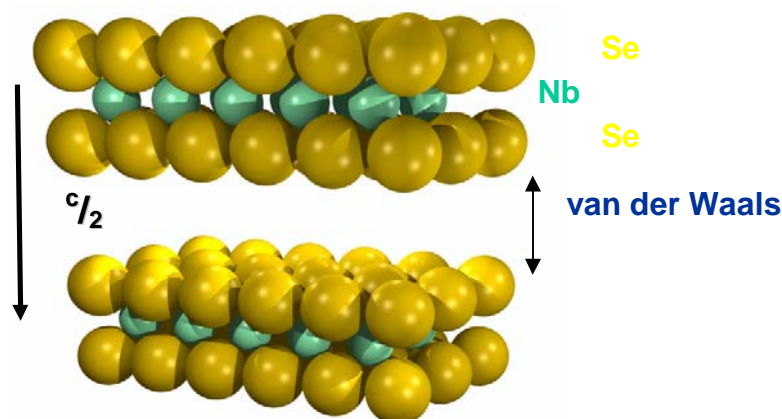


Figure 2-1 NbSe₂ has a layered structure consisting of Se-Nb-Se layers bound only by van der Waals forces.

The layers themselves are highly correlated, i.e. very well ordered, but perpendicular to the layers the structure is less well bound. As a result of this layer-like structure NbSe₂ displays almost two-dimensional behaviour, for example exhibiting a charge density wave transition.^{1,2,3} The structure arises from the stacking of hexagonal

packed planes (not close packed) as shown in Figure 2-1 with van der Waals forces between the layers. The hexagonal structure has lattice constants $a = 3.443 \text{ \AA}$, $c = 12.547 \text{ \AA}$ as measured by Meerschaut *et al.*¹⁹ at room temperature for a powder sample that displayed perfect stoichiometry. The calculated density is $6.467 \text{ g}\cdot\text{cm}^{-3}$. The single crystals investigated in this work are predominantly of the 2H-polytype and have the space group $P6_3/mmc$. Figure 2-2 shows the 2H-stacking. Though 2H is the most common several stacking polytypes exist. There are many discussions of the nature and relevance of polytypes in the literature such as discussed in Refs. 19, 21, 22, 23.

$> 33 \text{ K}$	Normal metal
$< 33 \text{ K}$	Incommensurate CDW
$< 6 \text{ K}$	Superconducting

Table 2-1 The important temperatures for NbSe_2 are shown above.

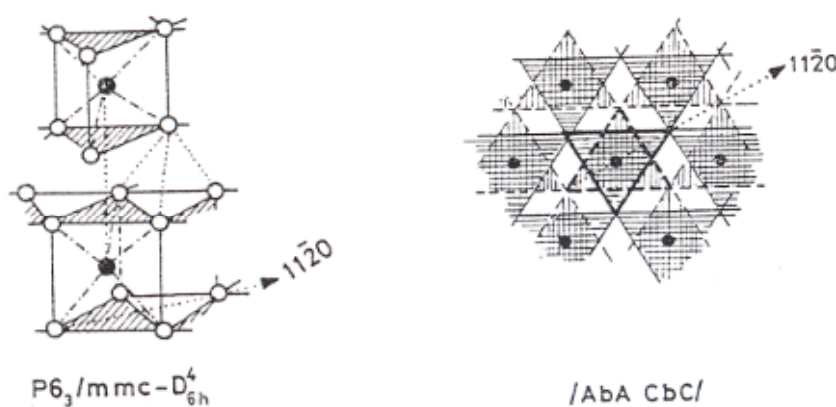


Figure 2-2 The structure of the 2H- NbSe_2 polytype shown on the left hand side in 3 dimensions and on the right hand side in plane view (after Wilson²³).

There are three known phases of NbSe_2 (Table 2-1). At temperatures greater than approximately 33 K it is a metal. Below 33 K an incommensurate CDW phase forms and below 6 K superconducting behaviour is observed in addition to the CDW instability. These phase transitions in NbSe_2 can clearly be seen in the resistivity measurement shown in Figure 2-3 where a dip in the resistivity occurs as the system undergoes the charge density wave transition, followed by a drop to immeasurably low resistivity at the superconducting transition.

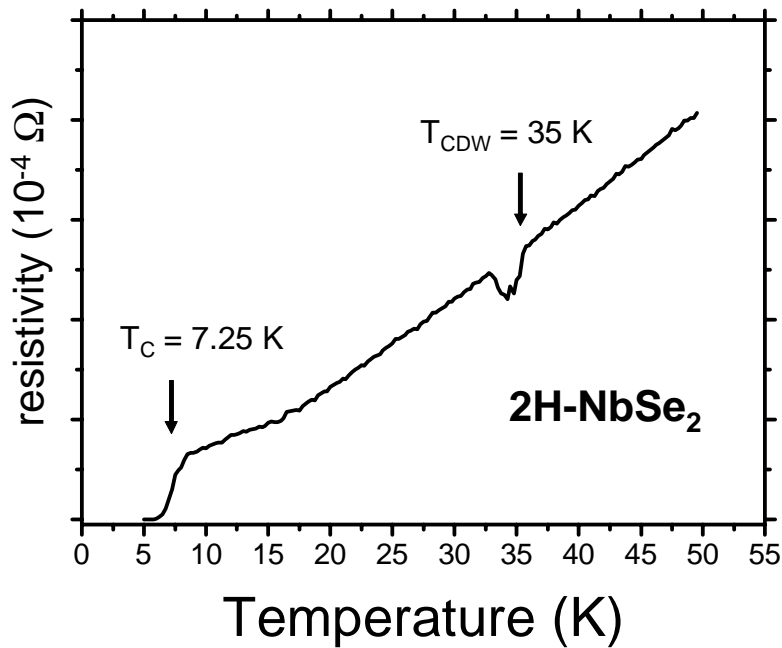


Figure 2-3 Resistivity measurements made by Oulo University show the transition temperatures in 2H-NbSe₂. Measurements courtesy of Ref. 24.

2.2 Charge density waves

In the mid 1970's quasi-one-dimensional metals were discovered which underwent unusual transitions. Materials such as NbSe₃ and “blue bronze” K_{0.3}MoO₃ were found

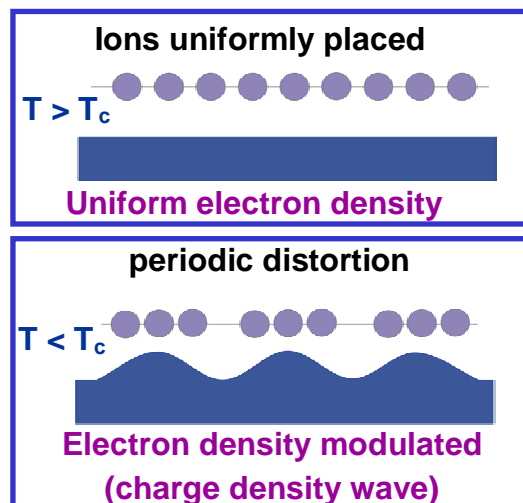


Figure 2-4 At room temperature there is a uniform distribution of the electron density. As the material is cooled the ions develop a static periodic distortion known as a Peierls distortion. In association with this distortion a Fermi gap opens up (after Thorne²⁵).

to undergo a charge density wave transition at low temperatures. Comprehensive reviews are given by Thorne²⁵ and Grunner²⁶ among others.

In a one-dimensional metal with a partly filled band, the lattice will never be stable at sufficiently low temperatures because the presence of the periodic potential would break the Fermi surface distribution, i.e. open a gap, resulting in a Peierls distortion. At room temperature there is a uniform distribution of the ion lattice. As the material is cooled below the critical temperature the ions form a periodic distortion (Figure 2-4).

The Peierls instability²⁷ in a 1D electron system is induced by strong electron-phonon interaction, which can develop due to the characteristic topology of the Fermi surface with a perfect nesting: For a single one-dimensional chain of atoms the Fermi “surface” consists of two points $k = +k_F$ and $k = -k_F$ (Figure 2-5). For a three-dimensional, periodic distribution of non-interacting chains the intersection of the energy band with the Fermi energy lies on two parallel planes which are perpendicular to the chain direction and can be shifted onto each other by the translation $|k| = 2k_F$. The overlap of parts of the Fermi surface as a result of a translation is called nesting.

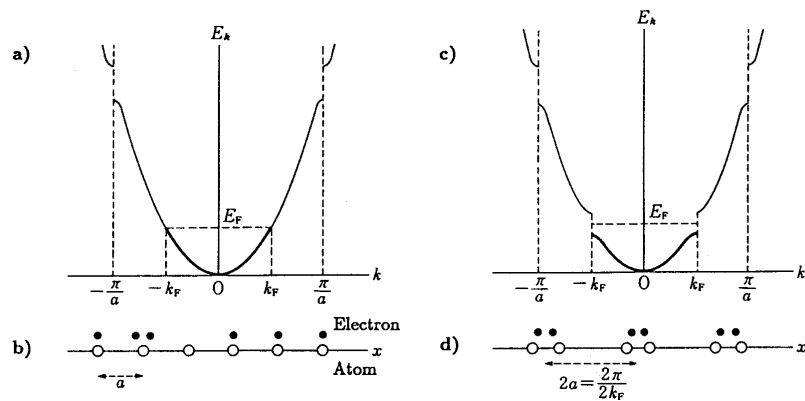


Figure 2-5 The Fermi energy behaviour for a Peierls instability: A one-dimensional electron system can lower its total energy by a lattice distortion. A half-filled band in a one-dimensional metal (a) at room temperature displays a uniform electron density (b). On cooling an energy gap opens at the new zone boundary (c) due to the periodic lattice distortion (i.e. the charge density wave) (d).

The Fermi surface and the nesting for electron systems of various dimensions are illustrated in Figure 2-6: For the one-dimensional case the overlap, i.e. the nesting, with respect to the translation $|k| = 2k_F$ is perfect, while for a 2-D system the overlap reduces to a line of the cylindrical Fermi surface and for a 3-D system to a single point on the Fermi sphere.

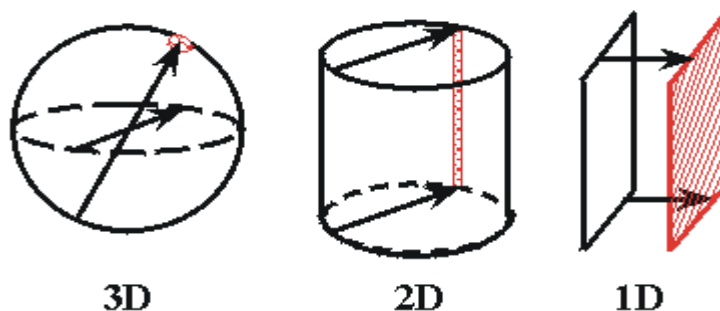


Figure 2-6 Fermi surface and nesting of ideal isotropic electron systems of various dimensions. In three dimensions the overlap is simply a point on the cylindrical Fermi surface, in two dimensions the overlap becomes a line on the cylindrical Fermi surface and only in the one-dimensional case perfect nesting occurs with respect to the translation $|k| = 2k_F$.

2.3 Previous NbSe₂ studies

In NbSe₂ a structural phase transition accompanied by a CDW distortion occurs at approximately 33 K^{1,3}. The crystal lattice modification associated with the charge density wave transition is fundamental to the transition, as the facilitating motion of the ions and an accompanying phonon mode reduce the large Coulomb energy of the CDW. Due to a linear coupling between the lattice and the charge density wave, a lattice distortion develops, which is proportional to the order parameter of the transition.

Though the origin of these instabilities is not fully understood, they are thought to result from Fermi surface nesting. Surface sensitive angle-resolved photoemission experiments suggested that Fermi nesting plays an important role in the charge density wave formation.^{4,5,6} A charge-density wave vector of $q = 0.69 \pm 0.06 \text{ \AA}^{-1}$ has been determined by Straub also using angle-resolved photoemission data on the Fermi surface and conduction band dispersion²⁸. The structure remains incommensurate even through a superconducting transition which occurs at $T \approx 6 \text{ K}$, reported to be a first order vortex transition^{3,5}. The superconductivity in 2H-NbSe₂ has been shown to be Fermi sheet-dependent^{4,5}. In a separate study Mallet has measured the local density of states in the CDW phase and revealed that the electronic structure close to the Fermi level and of the Fermi surface itself is very complex²⁹. Other techniques such as NMR studies³⁰ have shown that the local commensurability of the CDW should correspond to an orthorhombic symmetry.

In 1970 Overhauser³¹ predicted that satellite reflections should be observable with neutron diffraction due to the atomic displacements associated with the CDW instability as observed later by Moncton *et al.*¹. The charge density wave superstructure can also be observed in real space by STM³² as shown in figure Figure 2-7. Other STM studies of charge-density waves are reported by Sacks and Van Bakel^{33,34}.

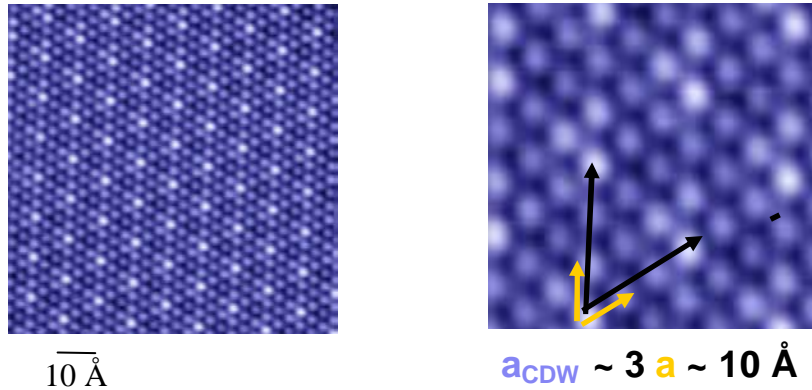


Figure 2-7 STM image of NbSe₂ collected below the charge density wave transition temperature (33 K). In the left hand picture the hexagonal superstructure due to the charge density wave is clearly visible superimposed on the hexagonal structure of the lattice. In the blown up picture on the right the superstructure of the charge density wave at $3a$ is seen, where the yellow arrow represents the regular lattice and the black arrow the superstructure resulting from the charge density wave (after Davis³²).

The CDW phase transition of bulk NbSe₂ has been investigated by both neutron and X-ray diffraction^{1,2,3} by monitoring the temperature dependence of the charge density satellite reflection intensity. This is possible as the charge density wave reflection intensity is proportional to the square of the order parameter. The presence of a CDW below 33.3 K with a hexagonal superstructure was reported by Moncton *et al.* in 1975 using neutron scattering^{1,2}. Moncton, Axe and DiSalvo carried out neutron studies of 2H-NbSe₂ and 2H-TaSe₂. They showed the CDW satellite reflection to be incommensurate on formation in both compounds with a wavevector $q_o = (1 - \delta)a^*/3$ where $a^* = 4\pi/\sqrt{3}a$. For NbSe₂, although the peak moves towards the commensurate position of $2/3$, it does not lock in over the temperature range from 32 to 10 K. In the case of 2H-TaSe₂, a first order lock-in transition was observed at 90 K.

Since the charge density wave formation in layered materials is related to the anisotropy of the layers it is expected that anisotropy in the long-range forces will be observed. This is very nicely illustrated by this example from 2H-TaSe₂ measured by Moncton and co-workers¹ (Figure 2-8). The correlation length perpendicular to the plane is only one third of that in the plane. This demonstrates a degree of two-dimensionality in TaSe₂. This can be related to the associated coupling constants (J_{\perp} , J_{\parallel}) so that $J_{\perp} = \frac{1}{3}J_{\parallel}$. In NbSe₂ one would expect a similar behaviour.

In addition, Moncton *et al.* observed strong Kohn anomalies in the case of both. For the two systems they observed Σ_1 phonon-like displacements and although they did not measure mode softening directly in NbSe₂ – it was measured for TaSe₂ – on this

ground they predicted a second order phase transition for both systems. The superlattice reflection intensity is shown in Figure 2-9 to fall continuously to zero.

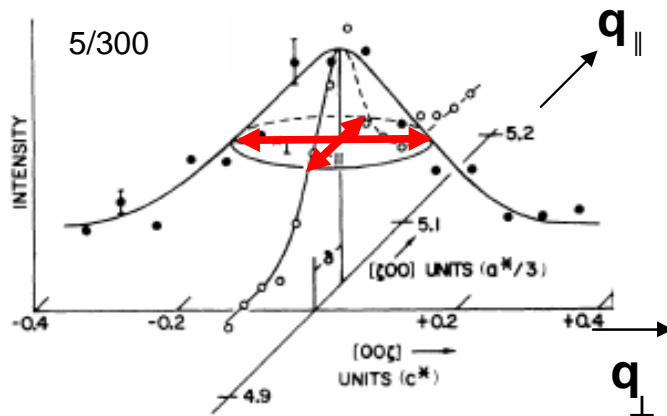


Figure 2-8 The critical scattering at the superlattice reflection in 2H-TaSe₂ is shown in both the q_{\parallel} and the q_{\perp} direction at 123 K. The width of the q_{\parallel} measured reflection is $\frac{1}{3}$ of that of the q_{\perp} measured reflection showing anisotropic correlation lengths (from Moncton²).

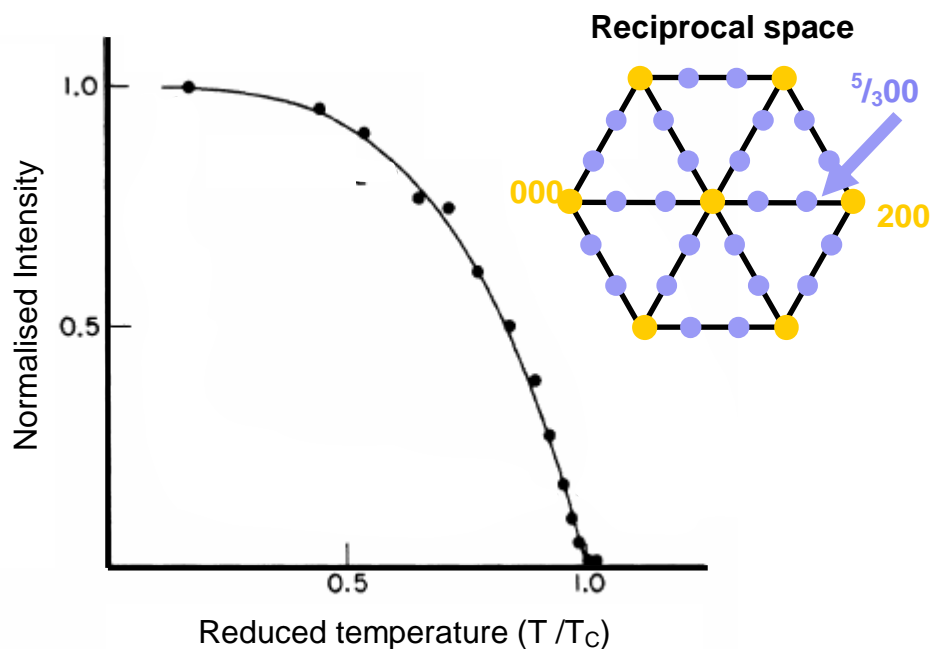


Figure 2-9 The normalised intensity of the charge density ($\frac{5}{3}00$) superlattice reflection versus temperature. The intensity falls smoothly to zero (after Moncton¹). This is consistent with a second order phase transition.

In a later neutron scattering experiment (1992) Ayache and co-workers⁷ investigated the softening of the longitudinal Σ_1 phonon mode at the charge density wave satellite

reflection in 2H-NbSe₂. They observed two modes at room temperature, ω_1 and ω_2 (Figure 2-10). The ω_1 optical mode remained constant as temperature was reduced. The uncertainty in the measurements is clearly seen in the figure where a band at approximately 75 meV was observed. Within the accuracy of the measurements no temperature dependence of the mode was observed. For the ω_2 acoustic mode found to be at about 25 meV at room temperature softening is observed from about 100 K and it appears to be complete at approximately 32 K within the experimental accuracy, indicating that NbSe₂ undergoes a second order transition at 32 K.

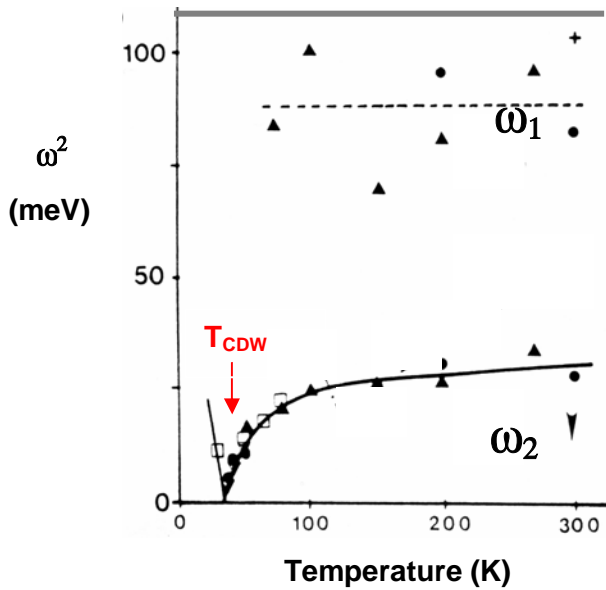


Figure 2-10 The temperature dependence of the longitudinal Σ_1 phonon. Complete mode softening is observed in the ω_2 branch as T_c is approached. This is indicative of a second order transition at $T_c = 32$ K. Figure from Ref. 7.

The incommensurate nature of charge density waves is discussed in the frame of Landau theory by McMillan³⁵ who found the lowest energy state near the lock-in transition to be a distorted plane wave. He also concluded that, at constant lattice parameter, the onset transition for a single charge density wave is continuous.

In summary, the neutron studies of Moncton^{1,2} and Ayache⁷ both predict that the charge density wave transition is a second order phase transition. However, as a small component first order behaviour is difficult to determine experimentally it can not be completely ruled out.

3 Theory of phase transitions

3.1 Introduction to phase transitions

Many of the fundamental concepts from the theory of phase transitions are common place. We are all familiar with the fact that matter occurs in different phases such as solid, liquid and gas. It is possible to change from one form to another by changing thermodynamic variables such as temperature, pressure or volume. For example, if the temperature is raised a block of ice becomes water and when heated further water turns into steam. There are many interesting examples of phase changes to be found all around us; everyday ones such as freezing water and more exotic ones such as NbSe₂ which changes from being conducting to superconducting at temperatures lower than 7 K or liquid helium which, when cooled below 2.2 K, becomes a superfluid.

The coexistence of phases is also no surprise to us; from first order phase transitions we know that at 0°C a beaker can contain water and ice at the same time. The matter in the beaker exists in two different states simultaneously.

We now consider the case where the beaker of water at room temperature is heated to 100° C. At low temperature there are perhaps a few very small bubbles of gas in the water which can be described as density fluctuations. As the water is heated one finds more and more gas bubbles occurring, i.e. greater density fluctuations. Close to the boiling temperature, the transition point, there is a large number of bubbles of different sizes. Above the boiling temperature more and more of the water becomes gas. The occurrence of such fluctuations, density or otherwise, close to the critical point of a second order transition is generally described by the term 'critical fluctuations'. These fluctuations may occur on many different length scales. Consider small bubbles of gas with a radius as low as a few microns to bubbles the size of the beaker close to the boiling point. Critical phenomena may be observed on a large range of length scales, ranging from 10⁻¹⁰ m in effects as described in quantum field theory to macroscopic turbulence occurring on the scale of microns to kilometres. Renormalisation group theory provides an algorithm for relating critical effects over a large range of length scales.

In theory one can at first consider such effects for infinite systems. In reality of course each system has a finite size and has surfaces or interfaces to be taken account of. As

one would expect the surface provides a disruption to the system. For example at a crystal surface some bonds are missing which can modify the local structure and lattice constants at the surface³⁶. It is therefore useful to devolve the theory to consider such effects.

In the study of different states of matter a phase diagram is often used to illustrate the transition of matter from one state to another. For example, a phase diagram for water can be described as a two-dimensional presentation showing the different phases of water with dependence on temperature and pressure, as in the above example. A third variable such as density or volume or more variables may be required to describe a complete system accurately.

In order to achieve a deeper understanding of phase transitions a theory that can qualitatively and quantitatively describe and predict critical behaviour is required. The charge density wave phase transition in NbSe₂ is the central topic of this thesis. In order to understand this effect a brief review and classification of phase transitions is given in this chapter. Both phenomenological and microscopic theories will be discussed. In particular, the effect of truncating the volume by a surface will be considered.

3.2 Thermodynamics of phase transitions

The first law of thermodynamics, conservation of energy, describes the differential dU

$$dU \equiv \delta Q - \delta W \quad (3-1)$$

where U is the internal energy of the system (see e. g. Finn³⁷) and

$$\delta W = PdV$$

is the quantity of work (where δ denotes an inexact differential) done by the system with pressure P and by volume change dV .

For an infinitesimal reversible process we can write for the change in heat

$$\delta Q = TdS \quad (3-2)$$

with temperature T and entropy S .^{38,39}

In order to give a thermodynamic description of phase transitions it is helpful to define thermodynamic relations that are analogous to the above. This was initially carried out for magnetic systems^{41,42}. We will replace the state variables P , V by a field H , and m as the change caused by this field, respectively. Following the notation of Stanley⁴¹ we can substitute

$$\begin{aligned} V &\rightarrow -m \\ P &\rightarrow H \end{aligned} \quad (3-3)$$

The first law of thermodynamics can now be written

$$dU = TdS + Hdm. \quad (3-4)$$

For an isolated system in an external field H at a given temperature T the state function or thermodynamic potential is the Gibbs free energy

$$G = G(T,H) = U - TS - mH. \quad (3-5)$$

In the initial formulation for magnetic systems m represented the magnetisation. More generally, the concept of an order parameter can be thought of as follows. Through the selection of an appropriate measure representing the order of the system, it is possible to describe a phase transition mathematically by quantifying the degree of order during a phase transition. By monitoring the degree of ordering as the temperature approaches the critical point, we can describe the mechanics of the phase transition. For a two-phase thermodynamic system where the high temperature phase has a lower degree of ordering than the low temperature phase, the thermodynamic order parameter m derived from the Maxwell relations and Equation (3-5) can be expressed as

$$m(T) = -\left(\frac{\partial G}{\partial H}\right)_T. \quad (3-6)$$

This is valid for a system that has $m(T)$ maximum at $T = 0$ and $m(T) = 0$ at T above a certain critical temperature. The isothermal susceptibility or response to the external field is defined as

$$\chi(T) \equiv \left(\frac{\partial m}{\partial H}\right)_T = -\left(\frac{\partial^2 G}{\partial H^2}\right)_T. \quad (3-7)$$

In the case where the acting field H is constant the entropy may be expressed as follows

$$S(H) = -\left(\frac{\partial G}{\partial T}\right)_H \quad (3-8)$$

and therefore the specific heat is given by

$$C_H(T) = T \left(\frac{\partial S}{\partial T} \right)_H = -T \left(\frac{\partial^2 G}{\partial T^2} \right)_H. \quad (3-9)$$

3.3 Classes of phase transitions

Historically, phase transitions are often divided into two classes; first order and second order. In the case of first order phase transitions the order parameter (Equation 3-6) displays a discontinuous behaviour at the transition point. This results in a discontinuity in the susceptibility and in the specific heat. There are many examples of first order transitions: a solid melting into a liquid, or some superconducting phase transitions such as the one found in NbSe₂⁵.

Second order phase transitions are continuous in the sense that the state of the body changes continuously. There is no latent heat associated with a second order transition, however the specific heat and susceptibility are discontinuous at a second-order phase transition point. The 2H-NbSe₂ charge density wave transition discussed in this thesis is considered to be a second order transition within the measured experimental accuracy^{1,7}. Other classic continuous phase transitions include the paramagnetic to ferromagnetic phase transition in iron and the transition of liquid He to a superfluid state.

The general aim of any theory is to help understanding of a phenomenon. Following on from the Nernst equations (based on the third law of thermodynamics) Landau provided a macroscopic theory to describe the nature of second order phase transitions. This model was later refined by Ising who introduced a simple lattice model.

3.4 Landau theory

In 1937 Landau provided a good treatment of phase transitions describing the thermodynamic potential near the critical point (this is described in detail in Ref. 40). As Landau theory does not account properly for critical fluctuations it fails in the immediate region of the critical point. Landau uses the assumption that it is possible to expand the thermodynamic potential in a power series about the critical point. The symmetric nature of the function can be seen in Figure 3-1. We know that the expansion about the critical temperature cannot be valid up to arbitrary orders and may have singularities. There are, however, grounds to suppose that its singularity is of higher order than the terms we consider below⁴⁰.

In Landau theory it is assumed that the Gibbs free energy can be expanded in a power series about $T=T_0$ depending on the order parameter m where $m(T_0)=0$:

$$G(T, m) = G_0(T) + \frac{a(T)m^2}{2} + \frac{b(T)m^4}{4} + \frac{c(T)m^6}{6} . \quad (3-10)$$

In the case of a second order phase transition, terms with odd powers of m are usually missing in order to fulfil symmetry requirements of the crystal on a microscopic level^{42,42}. Therefore only the even exponents are kept in the expansion of the free energy⁴¹.

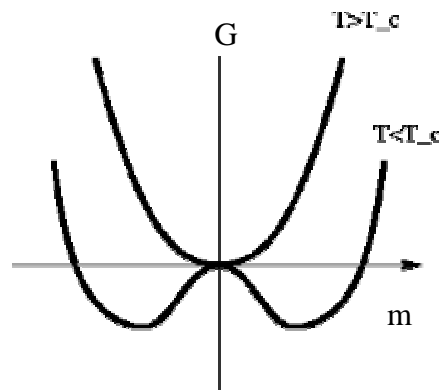


Figure 3-1: Landau theory describes the Gibbs free energy for a second order phase transition. The free energy has one minimum when $T > T_c$ and two minima when $T < T_c$.⁴⁰

If we consider a phase transition at a transition temperature T_c we can write

$$a(T) = a \left(\frac{T - T_c}{T_c} \right) \quad (3-11)$$

where a' is a positive constant below T_c . For a second order transition b is positive and constant and the last term of Equation (3-10) may be neglected .

The variation problem can be solved by minimising the Gibbs free energy with respect to the order parameter m .

$$\frac{\partial G}{\partial m} = 0 = a(T)m + bm^3 \quad (3-12)$$

It is then possible to write Equation (3-12) in the form

$$m \left[a' \left(\frac{T - T_c}{T_c} \right) + bm^2 \right] = 0 \quad (3-13)$$

Since a' and b are positive for $T > T_c$ the only real root is $m = 0$ (Figure 3-1). We define the dimensionless reduced temperature τ

$$\tau = \left(\frac{T - T_c}{T_c} \right). \quad (3-14)$$

For $T < T_c$ the minimum of the Landau free energy in zero applied field is at

$$|m(\tau)| = \left(\frac{a'}{b} \right)^{\frac{1}{2}} (-\tau)^{\beta} \quad (3-15)$$

where $\beta = 1/2$ when $\tau \leq 0$. The order parameter has a power law behaviour and will go continuously to zero in the case of a second order transition as outlined in Equation (3-15). (See Figure 3-2)

The critical behaviour of the order parameter susceptibility χ may be similarly determined for small position independent fields considering Equation (3-7)

$$\chi(\tau) \propto |\tau|^{-\gamma} \quad (3-16)$$

giving $\gamma = 1$. For the specific heat C_H considering Equation 3-9, it can be shown

$$C_H(\tau) \propto |\tau|^{-\alpha} \quad \tau < 0 \quad (3-17)$$

predicting $\alpha = 0$. The correlation length ξ is a measure of the range of the coherent oscillations in the system:

$$\xi(\tau) \sim |\tau|^{-\nu}. \quad (3-18)$$

$\nu = 1/2$ and ξ diverges at $T = T_c$ in a second order transition^{41,42}. The critical diffuse scattering intensity is proportional to the susceptibility. The correlation length ξ may be related to the pair correlation function $g(\vec{r}, \vec{r}')$ through a Fourier transformation.⁴³ For a three-dimensional system described by Landau theory (Ornstein-Zernicke⁴¹) it may be written as follows:

$$g(\vec{r}, \vec{r}', \tau) \propto \frac{1}{|\vec{r} - \vec{r}'|^{1+\eta}} e^{-\kappa|\vec{r} - \vec{r}'|} \quad (3-19)$$

where the exponent η is a correction known as the Fisher exponent. The term κ that appears in the exponential term is the inverse correlation length and it follows the following law:

$$\kappa = \kappa_0^\pm \cdot |\tau|^\nu. \quad (3-20)$$

The correlation length is defined as $\xi = \kappa^{-1}$. As the critical temperature is approached it grows rapidly and is divergent at T_c (Figure 3-2). The critical diffuse scattering intensity is proportional to the susceptibility that can be determined from the Fourier transform of the pair correlation function:

$$I_{diff} \propto \chi(\vec{q}, \tau) \propto \int g(\vec{r}, \vec{r}', \tau) e^{i\vec{q} \cdot (\vec{r} - \vec{r}')} d|\vec{r} - \vec{r}'|. \quad (3-21)$$

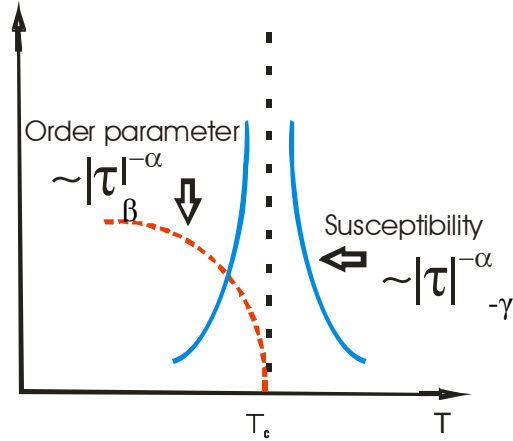


Figure 3-2: Temperature dependent behaviour of susceptibility and order parameter for a continuous transition close to T_c .

Close to T_c the exponential term in Equation 3-19 is equal to one and the pair correlation function follows a power law. It is therefore possible to write down the relationship between the susceptibility and the correlation length as

$$\chi(q, \tau = 0) \propto \frac{\kappa^2}{\kappa^2 + q^{2-\eta}}. \quad (3-22)$$

For three-dimensional systems, the Fisher exponent η is very small ($\eta \approx 0.03$), therefore, a Lorentz profile is observed in many experiments.

The limitation of the Landau theory is due to the fact that it does not consider critical fluctuations. Therefore, the description fails at temperatures in the immediate vicinity of the critical temperature. This failure means that the exponents predicted do not agree well with experimental findings. Nonetheless the theory provides a good framework to understand the phenomena occurring at temperatures close to the phase transition temperature particularly for complicated systems. The predicted values of critical exponents by Landau theory are the same as those of other classical theories such as mean field theory, Van der Waals theory and the Ornstein–Zernike theory.⁴¹ Values for the critical exponents as predicted by Landau theory are given in

Table 3-1.

3.5 Universality

For many second order phase transition systems the critical behaviour may be divided into equivalence classes. Where all members of an equivalence class have the same critical properties we say that universality is displayed. The thesis of quantitative universality states that all systems in the same universality class show the same critical behaviour in the sense that the critical exponents and all other characteristic

universal variables have identical numerical values. This concept is a very useful way of grouping systems with similar attributes.^{41,42,44}

The quantities used to classify a phase transition are (1) the dimensionality d , (2) the order parameter dimensionality n , i.e. the number of components required to describe the order parameter and (3) the range of interaction. Water for example is a 3-D system with a single component order parameter m . An example of a system where n is greater than 1 is the ferromagnetic transition in iron. One must then consider both magnitude and direction of the order parameter. For a spin- $1/2$ system with only two possible spin values the number of components reduces to 1 and can be described by the Ising model. For some alloys n can be as high as 4. There are different models for various values of n : Ising $n = 1$, XY $n = 2$, Heisenberg $n = 3$, Spherical $n = \infty$.

For systems of the same class identical exponents are found. These critical exponents are related by scaling relations

$$\alpha + 2\beta + \gamma = 2, \quad (3-23)$$

$$2 - \alpha = d\nu. \quad (3-24)$$

Many material properties depend upon microscopic details (lattice structure, type and range of interactions). This is also true for non-universal critical parameters such as the critical temperature or pressure. The critical exponents, however, are not material specific, but universal. They have the same numerical values for very different systems. Within a universality class non-universal quantities can be described by use of a scaling factor. Some examples of three-dimensional systems belonging to the same universal class are: the brass order-disorder transition, the liquid-gas transition at the critical point in CO₂ and the binary liquid wetting transition in hexane-nitrobenzene.

3.6 Mean Field theory

The mean field theory deals with problems involving many interacting particles. Interactions between many particles make the calculation of the partition function (nearly) insolvable. In this case fluctuations are neglected. The idea of mean field theory is to substitute the forces acting on a given particle by an effective external field. The exponents are the same as those given by the Landau theory. See

Table 3-1 for a comparison of exponents from the different theories.

model	d	n	α	β	γ	ν	η
Landau Mean field	}		0	0.5	1.0	0.5	0
Ising			2	1	'log'	0.125	1.75
Ising	3	1	0.11	0.325	1.241	0.63	0.031
XY	3	2	-0.007	0.346	1.316	0.669	0.033
Heisenberg	3	3	-0.015	0.365	1.386	0.705	0.033
spherical	3	∞	-1	0.5	2	1	0

Table 3-1 presents a compilation of the values predicted for the exponents α , β , γ , ν , and η for the mean field approximation, the Ising models and other common theories. Values from Refs. 10,11,43 and references therein.

3.7 Ising Model

In addition to phenomenological theories it is also possible to consider microscopic interactions and thereby include the lattice dimensionality in the description.

We write down the model Hamiltonian for the generalised Heisenberg model⁴¹, a classical spin system

$$H^{(n)} = -J \sum_{\langle i,j \rangle} S_i^{(n)} S_j^{(n)}. \quad (3-25)$$

In the case where $S_i^{(n)}$ are n -dimensional unit vectors and $-J$ the energy of a nearest neighbour pair $\langle ij \rangle$ of parallel spins localised on the sites i and j of the lattice. n is the order parameter dimensional unit and for the single component case it is 1, causing Equation (3-23) to simplify to the simple spin-half Ising model.

The Ising model provides a simple though by no means trivial model applicable to systems with two possible states of order (e.g. spin value $J = +1/2$ or $-1/2$) as in a ferromagnetic transition, or the analogous lattice-gas model for fluid systems⁴¹ such as the CO₂ liquid-gas transition. The Ising model can also be applied to superfluid, binary alloy and magnetic transitions. In its simplest form the Ising model assumes a cubic lattice arrangement where the interaction of each atom with the nearest neighbour can be considered (Figure 3-3). Coupling is introduced via nearest

neighbour interactions. Consider a pair of parallel spins with energy $-J$ and a pair of anti-parallel spins with energy J . The Hamiltonian is

$$H = -\sum_{\langle i,j \rangle} J_{ij} S_i S_j \quad (3-26)$$

where J_{ij} is the pair energy of the (ij) nearest neighbours. The Ising model can be generalised to describe the case for interactions further than nearest interactions and also for other lattices.

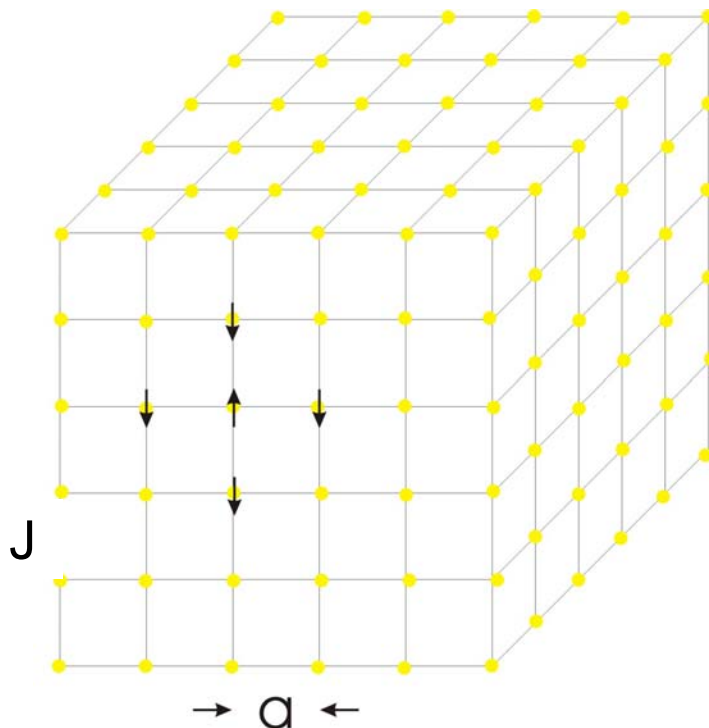


Figure 3-3: The 3-D Ising spin model can be considered as a cubic lattice where each element sits at a lattice point. J is the exchange interaction or nearest neighbour interaction between atoms that are a distance a apart. All the nearest neighbour interactions J are considered to be same. The spin elements and their associated direction are illustrated by the arrows.

The Ising model has no phase transition in one dimension and T_c is the absolute zero. If we now extend the lattice to two dimensions and beyond with $T_c > 0$, exponents may be calculated. Let us consider the case for the 3-D Ising model. Consider the system energy as the sum over all pairs of neighbours. If J_{ij} is positive, then having neighbours in the same state ($S_i = S_j$) decreases the total energy of the system. In particular, if all the coupling constants are positive, the system energy is minimised for the configuration in which all vertices are in the same state (either all +1 or all -1). If $0 < T < T_c$ the interatomic distance a is much smaller than the correlation length, $a < \xi$ where ξ is still much smaller than the system size L . Above T_c disorder takes

over and the order parameter is 0. Close to the transition temperature the correlation length tends towards infinity in an infinitely large system, and is limited only by the size of the system in a contained system.

Critical exponents may be obtained from the Ising model. These values for exponents α , β , γ , ν , and η are presented in

Table 3-1. There are other microscopic theories to describe critical behaviour allowing for situations more complicated than a simple spin $1/2$ case. There are extensions of the Ising model describing systems where the dimensionality of the order parameter n is greater than 1 such as XY, Heisenberg and Spherical models. It can be shown that the assumptions of nearest neighbour interactions and isotropic symmetry do not significantly affect the critical point predictions⁴¹. The reader is referred to the given references for a detailed discussion^{41,42}. For each model it is possible to predict values for the exponents as discussed before. The reported values for the different theories are also presented in

Table 3-1. There is a difference between the Ising model exponent values and the Landau ones – the phenomenological theories are not good at describing critical behaviour very close to the critical point as they neglect critical scattering.

3.8 Critical phenomena at surfaces

Continuing on in the frame of the previous discussion we now consider the effect of a surface or interface on a system in the case where no surface field is applied. This has been discussed by Binder¹¹, Diehl^{10,44}, Dietrich and Wagner⁹ and others. By relating the phenomenological Landau theory to microscopic mean field theories one can classify the behaviour close to a free surface. The Hamiltonian for the semi-infinite three-dimensional Ising model with modified surface coupling is

$$H = -J \sum_{\langle i,j \rangle_{bulk}} S_i S_j - J_s \sum_{\langle i,j \rangle_{surf}} S_i S_j. \quad (3-27)$$

To understand surface behaviour in a material one must consider the lack of atomic neighbours at the surface and the effect on local interactions with certain bonds missing. The order parameter has a position dependence on the scale of the correlation length. This means that in the region close to the surface we can consider the case where the degree of order is different than one would await for an infinite crystal.

The order parameter m requires a correction in the region close to the surface in the $1/2-\infty$ case. In the situation close to T_c where the correlation length ζ is close to the sample size Z every 'spin' knows it is in a finite system and therefore experiences finite size effects ($Z = Na$ where N is the number of layers and a is the distance

between atoms). It is the case $Z \gg \zeta$ as is normally found in an experiment we now discuss further.

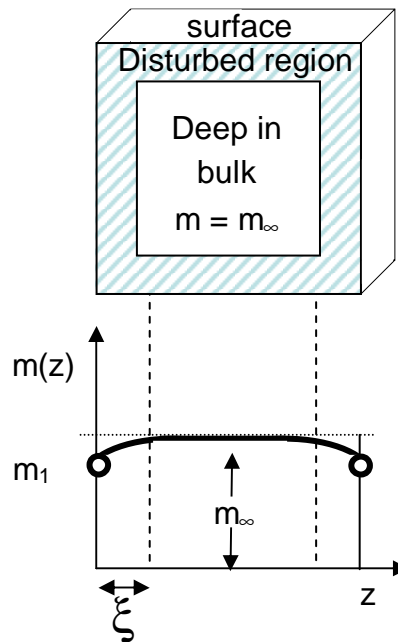


Figure 3-4 The effect of the presence of a surface on the order parameter m in a system with a short range correlation length. (After Diehl⁴⁴)

Considering Figure 3-4 one can see that the order parameter $m(z)$ in the middle of our cube becomes $m(\infty) = m_\infty$, while at the surface there is

$$m_1 = m(0) \Rightarrow m_1 \propto |\tau|^{\beta_1} \quad (3-28)$$

where β_1 is an exponent describing the surface order parameter. The order parameter at the surface m_1 and the other surface parameters show anomalous behaviour close to T_c which can be described by a power law with separate critical exponents. The order parameter density $m(z)$ at the surface $z = 0$ follows a different power law than $m(\infty)$. Let us consider the temperature dependence for $0 < z < \infty$. It is clear that $m(z)$ always displays anomalous behaviour as $T \rightarrow T_c$. To observe the temperature dependence of m_1 the distance z must be much smaller than ζ . It is important to note that the value of $m(z)$ is different for $z \ll \zeta$ than for $z \gg \zeta$.

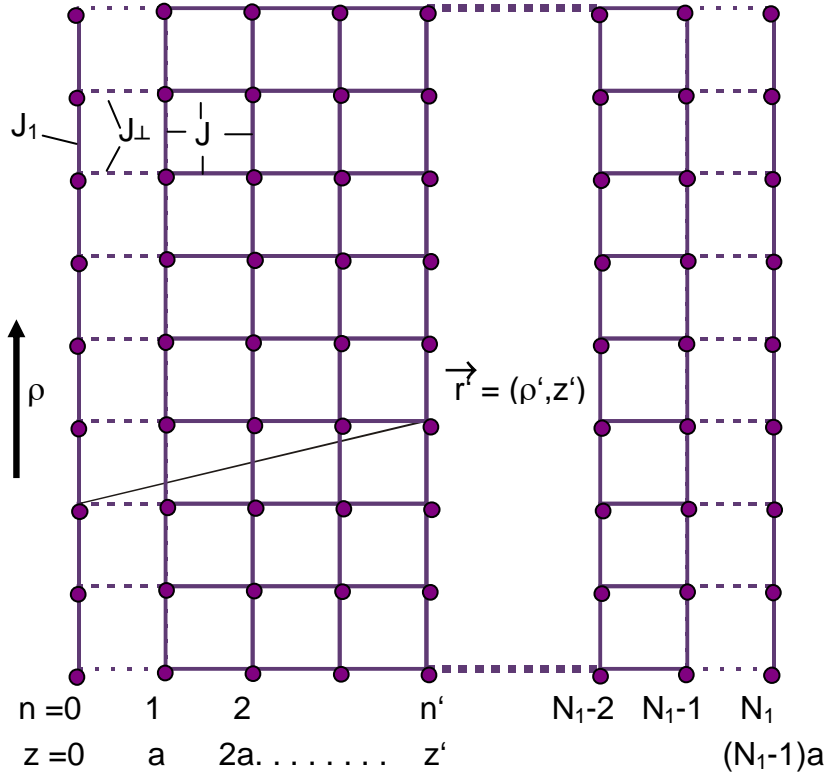


Figure 3-5 This figure shows the modification to the Ising model due to the presence of a surface or interface. The cross section of a d -dimensional Ising film of N_1 layers is shown schematically. Each vertical line represents a $(d-1)$ -dimensional layer, with coordinate ρ . Each layer has an index n from 0 to N_1 or z from 0 to $N_1 a$. An arbitrary point is denoted by the vector $\vec{r} = (\rho', z')$. For $N_1 \rightarrow \infty$ the system is a half-infinite system with a free surface at $z = 0$. In the bulk the nearest neighbour interactions are all the same (J). However in the surface plane the interactions between the spins are J_1 , and to the adjacent plane is J_\perp (after Ref. 11).

For the case for $m(z)$ where $a \ll z \ll \xi$ a power dependence is displayed

$$m(z) \approx z^{\frac{(\beta_1 - \beta)}{\nu}} \quad (3-29)$$

where β_1 the exponent describing the surface order parameter and β is the exponent describing the bulk order parameter. In the case of the bulk there is a single universal classification for a wide range of systems however at the surface more classes are required than in the bulk.

In order to take a closer look at the surface we use the 3-D Ising description of a simple cubic half-infinite ($1/2-\infty$) system as shown schematically in Figure 3-5. In such a system all nearest neighbour interactions can be described by the coupling constant J . Here as in section 3.7 we consider J as the coupling constant in the bulk and we introduce J_1 as a modified coupling constant at the surface. In the case of the 3-D Ising bulk each atom had 6 nearest neighbours so

$$\Delta E_b = 6J. \quad (3-30)$$

On the surface there are only 5 nearest neighbours, in addition we have now a modified coupling constant J_1 at the surface and $J_{\perp} = J$:

$$\Delta E_s = 4J_1 + J , \quad (3-31)$$

therefore we can state the following relations:

$$J_1 \leq J \Rightarrow \Delta E_s < \Delta E_b , \quad (3-32)$$

$$J_1 \gg J \Rightarrow \Delta E_s > \Delta E_b . \quad (3-33)$$

If the second case were to occur then more surface energy would be required and then there is a transition temperature T_{cs} that is greater than T_c . Exploring the ratio of the two coupling constants $x = J_1/J$, which is called enhancement, it is possible to develop a picture of the temperature dependence of the surface transition temperature with respect to bulk one as shown graphically in Figure 3-6. In order to describe such a half infinite system there are four classes of transitions: **ordinary**, **surface**, **extraordinary** and **special**.

The critical behaviour at surfaces is principally determined by the interaction of two characteristic lengths, the bulk correlation length ζ_b and the extrapolation length λ . The extrapolation length - a linear projection of the order parameter - characterizes the order parameter profile due to the fact that $m(z)$ varies linearly with z near T_c as shown graphically in Figure 3-7. If one extrapolates the $m(z)$ variation it vanishes at $z = \lambda$ (thus the term extrapolation length). When one considers that the extrapolation must not be constrained to $0 < \lambda < \infty$ there is the possibility of different classes of transitions occurring in the half- infinite description.

In the case where $0 < 1/\lambda < \infty$ an '**ordinary transition**' occurs and the bulk and the surface order simultaneously at $T_c = T_{cb} = T_{cs}$. This occurs when the enhancement J_1/J is < 1.5 . The transition is bulk driven and the degree of order is less at the surface than in the bulk. The order parameter falls off exponentially as the surface is approached over the range ζ_b .

The '**surface transition**' describes the unusual case where the surface orders first while the bulk remains disordered, $T_{cs} > T_{cb}$. Here critical behaviour is observed in the surface layer but it is not extending infinitely into the bulk. In the region $T_c < T < T_{cs}$ the bulk correlation length is finite and the order parameter falls off exponentially as one penetrates into the bulk. The extrapolation length is negative. In this region

$$m_1 \sim |\tau|^{1/8} . \quad (3-34)$$

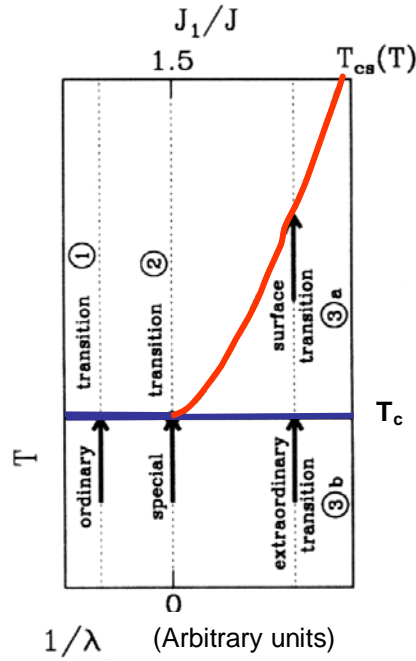


Figure 3-6 The figure shows the phase transitions that can occur at the surface of a semi-infinite system. In the case of nearest neighbour interactions the inverse extrapolation length λ^{-1} is proportional to the enhancement J_1/J of exchange interactions in the surface layer.¹¹

On lowering the temperature further an ‘**extraordinary transition**’ occurs. Here the bulk orders in the presence of an already ordered surface ($T_{cb} = T_c$). The critical behaviour or cross-over of the order parameter in this region⁴⁵ is then

$$m_1 - m_1^{reg} \approx |\tau|^{\beta_1} \quad (3-35)$$

where

$$m_1^{reg} = m_{1c} + a\tau + b^\pm \tau^{(2-\alpha)}. \quad (3-36)$$

m_1^{reg} is a background term due to the fact that surface ordering is already present, m_{1c} is the value of m_1 at T_{cb} and a and b are constants. From this expression the following scaling law can be derived:

$$\beta_1 = 2 - \alpha. \quad (3-37)$$

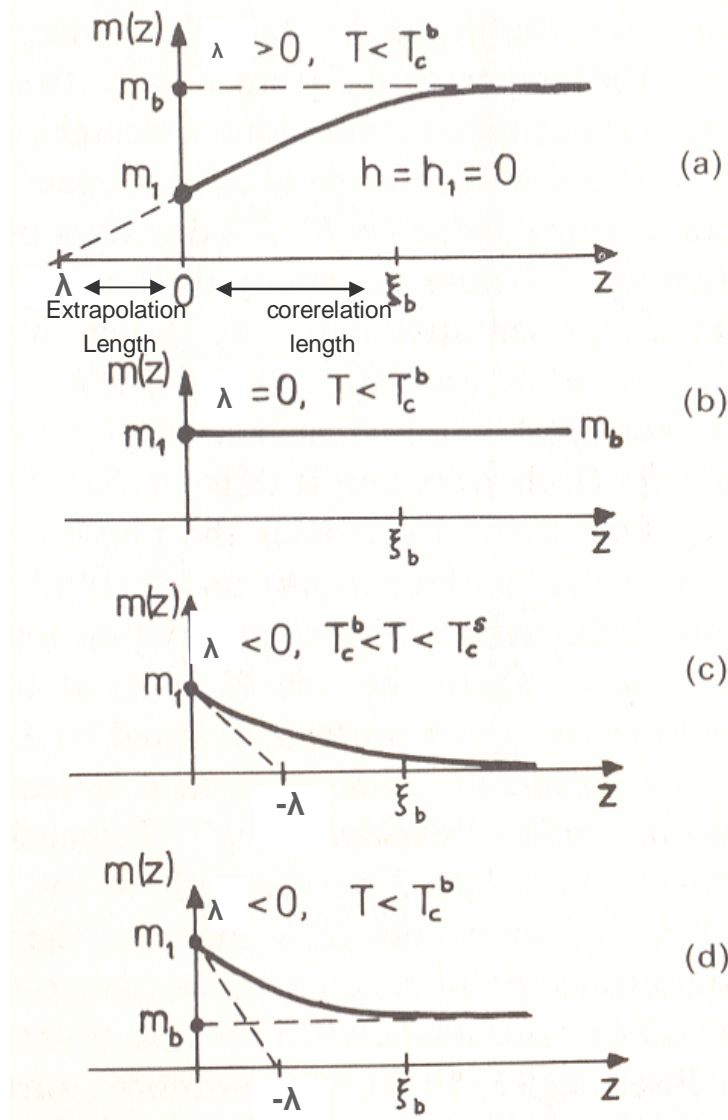


Figure 3-7 Landau or mean field approximation give rise to the order parameter profiles shown for the ordinary (a), special (b), surface (c) and extraordinary (d) transitions. The inverse extrapolation length discussed in the text is shown with a dashed line after Refs. 10,11.

A ‘special transition’ or ‘surface bulk’ transition occurs in the case where the extrapolation length is infinite. In this case the bulk and surface order simultaneously. The critical exponents are surface driven. In this case the surface and bulk exponents are equal.

The ordinary, surface, extraordinary and special transitions are continuous. The order parameter profiles as obtained by Lubensky and Rubin⁴⁶ are shown in Figure 3-7.

It is generally considered that as one goes from a bulk transition to a surface transition that one degree of dimensional freedom is lost. For example in the case of a three-dimensional bulk transition the associated surface transition is considered to be two-dimensional.

For three-dimensional systems as we cross $T = T_c$ the bulk order parameter m_∞ can be determined independently of J_I/J . In the volume there is universality of the 3-D Ising model due to the short range interaction which results in characteristic critical behaviour. The surface order parameter m_1 , however, displays a behaviour that is strongly dependent on the value of J_I/J . So while a single universal class exists to describe volume transitions, on the surface there are different classes. The critical behaviour of the specific heat C_I , the order parameter m_I , the order parameter susceptibility χ_1 at the surface can be described by the critical exponents α_1 , β_1 , γ_1 respectively similar to those in the bulk:

$$C_1 \propto |\tau|^{-\alpha_1}, m_1 \propto (-\tau)^{\beta_1}, \chi_1 \propto |\tau|^{-\gamma_1} \quad (3-38)$$

where the reduced temperature τ as defined in Equation (3-14).

Many authors have calculated values for the surface exponents. Table 3-2 presents a summary of these findings.

Universality class		β_1
Ordinary	Mean Field	1
Special	Mean Field	0.5
Extraordinary	Mean Field	1
Surface	Mean Field	0.5
Ordinary	Ising - 3D	0.8
Special	Ising - 3D	0.25
Extraordinary	Ising - 3D	0.175
Surface -	Ising - 3D	0.125

Table 3-2 A summary of the predicted values for the surface exponent β_1 is presented here according to Refs. 15,11,10,45,43,47.

Relate theory to experiment

Due to a linear coupling between the lattice and the charge density wave, the change of lattice distortion, which develops in NbSe₂, can be measured via the intensity of the superlattice reflection. This is then proportional to the square of the order parameter m .¹ Therefore we can study the nature of the phase transition by following the temperature-dependent behaviour of the CDW satellite scattering intensity, which can be expressed as

$$I = I_o \tau^{2\beta}, \quad (3-39)$$

where we need to take 2β as we measure intensity and not amplitude. This can be expressed as

$$\log \frac{I}{I_0} = 2\beta \log |\tau| \quad (3-40)$$

which can be determined experimentally. Other variables such as the diffuse intensity, the full width half maximum of the diffuse component and their dependence on reduced temperature can also be related to the exponents described in this chapter. In addition the susceptibility can be described by measuring the diffuse scattering intensity as seen in Equation 3-21, where we saw that $I_{diff} \propto \chi(\vec{q}, \tau)$.

4 Theory of X-ray diffraction

4.1 X-ray diffraction

When X-rays impinge on a periodic array of atoms they are scattered by the electrons and strong reflections may be observed in certain discrete directions. This behaviour is the result of constructive interference of the radiation scattered by the scattering centres and is described by the Bragg law. In the following discussion the Bragg law is discussed and methods for using it to determine the crystal structure and orientation are presented. By measuring the angles of the reflections one can determine the lengths describing the periodic arrangement of the scatterers if the wavelength of the radiation is known. Similarly a crystal of known structure can be used as a spectrum analyser or as a monochromator.

The determination of unknown crystal structures by indexing intense reflections is just one application of X-ray diffraction. Diffraction can also be used to determine stress/strain in materials, to monitor defects, to determine material composition and to study phase transitions. These are just a few examples. Structure determination is carried out not only for pure crystalline materials such as diamond⁴⁸ for example, but also for non-crystalline materials such as polymers and composite materials such as wood and fibres. Many chemists and biologists use X-ray diffraction as a tool in their work. John Walker shared the 1997 Nobel Prize for his structure determination work on the F₁-ATPase structure, a protein which plays a key role in cellular energy production⁴⁹. Recently Takada *et al.*⁵⁰ determined the structure of a new cobalt oxide low-temperature superconductor ($T_c = 5$ K) using X-ray diffraction. In some cases the crystal structure undergoes a phase transition when the temperature is changed or pressure is applied. In this case the structure change can be monitored by X-ray diffraction as a function of the applied field. In this way the order parameter for the phase transition may be determined as discussed in chapter 3. As seen in this thesis, the intensity of reflections associated with the superstructure due to the charge density wave modulation^{1,3,51} may be measured in order to determine the order parameter and thermodynamic potentials. Similarly surface reconstructions resulting in superstructures^{52,53} can also be observed by X-ray diffraction.

4.2 Bragg diffraction

In 1915 Sir William Henry Bragg and his son Sir William Bragg jointly received the Nobel prize in physics for developing Bragg's law and for their work in the field of X-ray diffraction as a tool for crystal analysis. The Bragg law describes the way in which X-rays are scattered from a periodic array of scatterers as shown in Figure 2-1. For monochromatic X-rays the reflected X-rays from successive planes will constructively interfere if the total difference of the optical path length is an integer number of wavelengths. For an incident beam and diffracted beam of angle θ with respect to planes of spacing d

$$2d \sin \theta = n\lambda \quad (4-1)$$

where n is a positive integer and λ the wavelength of the radiation.

An X-ray photon falling on an atom may be absorbed or scattered. We consider the scattering process in terms of classical theory, i.e. pose the question what is observed when X-rays scattered by an atom are viewed at a detector a large distance R_0 from the sample. In the dipole approximation, the amplitude of a wave A_e that comes from a single scattering electron at \vec{r}_e as a function of the amplitude of the incoming wave A_0 may be described using the Thompson formula ⁵⁷

$$A_e \exp(-i\vec{k}_f \cdot \vec{r}_e) = A_0 \frac{e^2}{mc^2} \frac{1}{R_0} \exp(-i\vec{k}_i \cdot \vec{r}_e) \quad (4-2)$$

where e is the charge of the electron, m is electron mass, c is the speed of light. \vec{k}_i is the incoming wavevector, \vec{k}_f the outgoing wavevector and the vector \vec{r}_e is the distance to the electron from the crystal origin 0 , as shown in Figure 4-1 and defined below. We assume an elastic scattering process. The kinematical approximation is valid as, even with the large number of electrons in the crystal, the total scattering cross section is small since the constant e^2/mc^2 is very small. This allows us to take the scattered amplitude as the sum of the independent contributions from each individual electron.

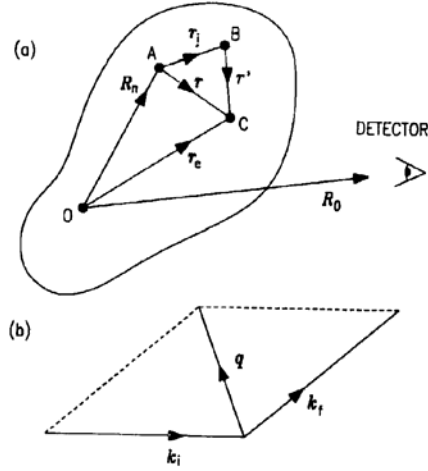


Figure 4-1 The real space vectors discussed in the text are defined in (a). The point 0 is defined as the origin of the crystal, A is the origin of the n^{th} cell, B is the j^{th} atom of the n^{th} cell and C is an electron belonging to the j^{th} atom of the n^{th} cell. In (b) the reciprocal space vectors are defined. \vec{k}_i is the incident and \vec{k}_f the exit wave vector (see Equation 4-4).

4.3 Scattering from atoms and three-dimensional crystals

The momentum transfer \vec{q} is the difference between the incoming wave vector \vec{k}_i in the direction of the beam and the outgoing wave vector \vec{k}_f . This is shown schematically in Figure 4-1b and can be written

$$\vec{q} = \vec{k}_f - \vec{k}_i. \quad (4-3)$$

Since we assume that the scattering is elastic

$$|\vec{k}_i| = |\vec{k}_f| = |\vec{k}| = \frac{2\pi}{\lambda}, \quad (4-4)$$

where λ is the wavelength of the incoming X-rays, we can rewrite the Bragg law described in Equation (4-1)

$$|\vec{q}| = 2|\vec{k}| \sin\left(\frac{2\theta}{2}\right) \quad (4-5)$$

showing that it is possible to relate the momentum transfer \vec{q} to the scattering angle 2θ in an experiment. Equation 4-2 can be expressed as

$$A_e = A_0 \frac{e^2}{mc^2} \frac{1}{R_0} \exp(i\vec{q} \cdot \vec{r}_e). \quad (4-6)$$

This equation allows us to calculate the scattering intensities of individual atoms.

Now we consider the scattering amplitude of the radiation at the detector due to scattering by a single atom⁶⁷. It is obtained by performing a volume integral of equation 4.5 over the electron density $\rho(\vec{r}')$ of the atom of volume d^3r' given by

$$A_{atom} = A_0 \frac{e^2}{mc^2} \frac{1}{R_0} \int_{-\infty}^{+\infty} \rho(\vec{r}') \exp(i\vec{q} \cdot (\vec{R}_n + \vec{r}_j + \vec{r}')) d^3r' \quad (4-7)$$

$$= A_0 \frac{e^2}{mc^2} \frac{1}{R_0} f(\vec{q}) \exp(i\vec{q} \cdot (\vec{R}_n + \vec{r}_j)), \quad (4-8)$$

where the atomic form factor

$$f(\vec{q}) = \int \rho(\vec{r}') \exp(i\vec{q} \cdot \vec{r}') d^3r' \quad (4-9)$$

is the Fourier transform of the electron density for a single atom. Since in almost all cases atoms or ions are considered to be spherical, the atomic form factor then is independent of direction, and so $f(q)$ is written purely as a function of magnitude of the momentum transfer.

We have described the scattering first for an electron and then for a single atom. Now we consider the case of a unit cell of a crystal consisting of a periodic array of atoms. Separate form factors $f_i(q)$ are assigned to each atomic site as the material may consist of different chemical elements. For a unit cell containing of N_c atoms

$$\begin{aligned} A_{unit\ cell} &= A_0 \frac{e^2}{mc^2} \frac{1}{R_0} \sum_{j=1}^{N_c} f_i(q) \exp(i\vec{q} \cdot (\vec{R}_n + \vec{r}_j)) \\ &= A_0 \frac{e^2}{mc^2} \frac{1}{R_0} F(\vec{q}) \exp(i\vec{q} \cdot (\vec{R}_n)) \end{aligned} \quad (4-10)$$

where $F(\vec{q})$, the structure factor, is the sum over all the atoms in one unit cell

$$F(\vec{q}) = \sum_{j=1}^{N_c} f_j(q) \exp(i\vec{q} \cdot \vec{r}_j). \quad (4-11)$$

The structure factor is \vec{q} -dependent as one must consider the relative positions of the atoms in the unit cell. It can alternatively be expressed as

$$F(\vec{q}) = \int_{cell} \rho(\vec{r}) \exp(i\vec{q} \cdot \vec{r}) d^3r \quad (4-12)$$

where \vec{r} is defined as in Figure 4-1 and $\rho(\vec{r})$ is the sum of the contributions from all the atoms in the unit cell.

Finally, to consider the entire crystal we sum up the contributions from each unit cell. To calculate the scattering intensity for a block shaped crystal with the three crystal axes defined by unit cell vectors \vec{a}_1 , \vec{a}_2 , \vec{a}_3 , we sum over all unit cells so

$$A_N = A_0 \frac{e^2}{mc^2} \frac{1}{R_0} F(\vec{q}) \sum_{n_1=0}^{N_1-1} \sum_{n_2=0}^{N_2-1} \sum_{n_3=0}^{N_3-1} \exp(i\vec{q} \cdot (n_1\vec{a}_1 + n_2\vec{a}_2 + n_3\vec{a}_3)) \quad (4-13)$$

where N_j , $j=1$ to 3 , is the number of unit cells along the axis \vec{a}_j . If we now consider N_1 as the total number of atoms along \vec{a}_1 , N_2 the total number of atoms along \vec{a}_2 etc., a geometric series can be summed up easily

$$S_N(\vec{q} \cdot \vec{a}) = \sum_{n=0}^{N-1} \exp(i\vec{q} \cdot n\vec{a}_j) = \frac{1 - \exp(i\vec{q} \cdot \vec{a}N)}{1 - \exp(i\vec{q} \cdot \vec{a})}. \quad (4-14)$$

This complex quantity represents a simplified version of the scattering amplitude for a one-dimensional crystal containing N atoms. In a diffraction experiment the intensity $I(\vec{q})$ is measured:

$$I(\vec{q}) \sim |S_N(\vec{q} \cdot \vec{a})|^2 = \frac{\sin^2\left(\frac{i\vec{q} \cdot \vec{a}N}{2}\right)}{\sin^2\left(\frac{i\vec{q} \cdot \vec{a}}{2}\right)}, \quad (4-15)$$

also known as the N -slit equation from optics. We can now express Equation 4-13 in the following form

$$A_N = A_0 \frac{e^2}{mc^2} \frac{1}{R_0} F(\vec{q}) S_{N_1}(\vec{q} \cdot \vec{a}_1) S_{N_2}(\vec{q} \cdot \vec{a}_2) S_{N_3}(\vec{q} \cdot \vec{a}_3). \quad (4-16)$$

The Equation (4-16) has maxima at the point \vec{G}_{hkl} , where \vec{G}_{hkl} can satisfy the three Laue equations

$$\begin{aligned}\vec{a}_1 \cdot \vec{G}_{hkl} &= 2\pi h \\ \vec{a}_2 \cdot \vec{G}_{hkl} &= 2\pi k \\ \vec{a}_3 \cdot \vec{G}_{hkl} &= 2\pi l\end{aligned}\quad (4-17)$$

Bragg reflections are observed at the intensity maxima where h, k, l are the integers known as the Miller indices. It is now possible to define a reciprocal lattice where the reciprocal lattice vector \vec{G}_{hkl} can be defined as a linear combination of the reciprocal lattice vectors \vec{b}_j . In order to relate these with the lattice in real space we can introduce the concept of lattice planes h, k, l .

$$\vec{G}_{hkl} = h\vec{b}_1 + k\vec{b}_2 + l\vec{b}_3, \quad (4-18)$$

where

$$\begin{aligned}\vec{b}_1 &= 2\pi \frac{\vec{a}_2 \times \vec{a}_3}{\vec{a}_1 \cdot (\vec{a}_2 \times \vec{a}_3)} \\ \vec{b}_2 &= 2\pi \frac{\vec{a}_3 \times \vec{a}_1}{\vec{a}_1 \cdot (\vec{a}_2 \times \vec{a}_3)} \\ \vec{b}_3 &= 2\pi \frac{\vec{a}_1 \times \vec{a}_2}{\vec{a}_1 \cdot (\vec{a}_2 \times \vec{a}_3)}\end{aligned}\quad (4-19)$$

The vectors $\vec{b}_1, \vec{b}_2, \vec{b}_3$ are the basis of the reciprocal lattice and \vec{b}_1 is orthogonal to the lattice vectors \vec{a}_2 and \vec{a}_3 , \vec{b}_2 to \vec{a}_1 and \vec{a}_3 , and \vec{b}_3 to \vec{a}_1 and \vec{a}_2 that span the unit cell. Now we can state that the intensity measured is of the form

$$I_{hkl} = \left| A_0 \frac{e^2}{mc^2} \frac{1}{R_0} F(h\vec{b}_1 + k\vec{b}_2 + l\vec{b}_3) N_1 N_2 N_3 \right|^2 \quad (4-20)$$

Considering equation 4.4 we can now also state

$$q_{hkl} = G_{hkl} = 2k \sin \frac{\phi_{hkl}}{2} \quad (4-21)$$

Using this formula we can relate the angle of diffraction or scattering angle ϕ_{hkl} to the scattering vector modulus q_{hkl} . From Equation 4-15 the half width of the Bragg reflections can be determined along all three crystal axes. This gives us information

about the number of coherently scattering unit cells N_j and thereby the size of crystallites in the crystal $\xi_{crystal} = N_j a_j$. A good approximation for the FWHM^{54,55} is

$$\sigma_{fwhm,j} \approx \frac{2\pi}{N_j a_j} = \frac{2\pi}{\xi_{crystal}} \quad (4-22)$$

often expressed in the following form

$$\frac{1}{2} \sigma_{fwhm} \sim 1/\xi_{crystal} \quad (4-23)$$

This approximation holds well when the illuminated area is large compared to the crystal domain size.

From the Bragg law description given in Equation 4-5 we can relate the spacing between scattering planes d_{hkl} to the modulus of the reciprocal lattice vector \vec{G}_{hkl} . NbSe₂ has a hexagonal symmetry which means that $a_1 = a_2 \neq a_3$ and the angles between the basis vectors are $\alpha = \beta = 90^\circ$, $\gamma = 120^\circ$. In this case the lattice spacing is

$$d_{hkl} = \frac{1}{\sqrt{\frac{4}{3} \left(\frac{h^2 + hk + k^2}{a^2} \right) + \frac{l^2}{c^2}}}. \quad (4-24)$$

4.4 Surface X-ray diffraction

The effect of introducing a surface to our system can be developed from Equation 4-17. Consider first the topmost layer. If we take \vec{a}_3 to be along the surface normal, we set $N_3 = 1$ for this single layer, and the observed diffraction is then independent of $\vec{a}_3 \cdot \vec{G}_{hkl}$, the component of momentum transfer perpendicular to the surface. In 3-D reciprocal space for a purely two-dimensional layer we would have rods of intensity sharp in the two directions parallel to the surface and a diffuse streak in the perpendicular direction with the bulk. For the half-infinite case we now consider both the surface layer and the bulk contribution. In this case we observe Bragg reflections superimposed on the 2-D Bragg rods^{56,57}.

If we define the wavevector

$$\vec{q}_3 = \vec{G}_3 + \Delta\vec{q} \quad \text{where } \Delta\vec{q} \parallel \vec{b}_3 \quad \text{and} \quad \Delta\vec{q} \neq 0, \quad (4-25)$$

these intensity streaks occur perpendicular to the surface and are known as crystal truncation rods (CTR's) since they result from the crystal being truncated^{58,60}. This intensity profile can be derived by considering the N -slit function described in Equation (4-15). For large values of N the numerator is a rapidly varying positive function and so $\sin^2(N\vec{q} \cdot \vec{a}_3/2)$ can be approximated by its average value of $1/2$ giving

$$|S(\vec{q}_3 \cdot \vec{a}_3)|^2 = \frac{1}{2 \sin^2(\frac{1}{2} \vec{q}_3 \cdot \vec{a}_3)}. \quad (4-26)$$

This equation, though it is not valid very close to Bragg reflections, illustrates a non-zero intensity along the surface normal. The intensity distribution along a crystal truncation rod can thus be expressed as

$$I_{ctr} = \left| A_0 \frac{e^2}{mc^2} \frac{1}{R_0} F(\vec{q}_3) N_1 N_2 \right|^2 \frac{1}{2 \sin^2(\frac{1}{2} \vec{q}_3 \cdot \vec{a}_3)}. \quad (4-27)$$

In the case of small $\Delta\vec{q}$ and from the third Laue condition it can therefore be shown that

$$I_{ctr}(\Delta\vec{q}) \sim \left| F(\vec{G}_{hkl} + \Delta\vec{q}) \right|^2 \frac{1}{2a_3^2} \cdot \frac{1}{\Delta q^2}, \quad (4-28)$$

showing that the intensity of a Bragg reflection at the surface has a $1/|\Delta\vec{q}|^2$ dependence. The intensity of the truncation rod is modified due to the presence of layers on the surface or surface roughness (see below).⁵⁹

There is a second approach in which the CTR is represented as a product of the step function with an infinite lattice. The electron density of a sample with a perfectly flat surface in the (x, y) plane at $z = 0$ can be written as

$$\hat{\rho}(\vec{r}) = \rho(\vec{r})\Theta(z), \quad (4-29)$$

where the function $\Theta(z)$ is the Heavyside step function and $\rho(\vec{r})$ is the electron density for an infinitely extended crystal. It is known from the kinematic approximation that the Fourier transform of the electron density is the scattering amplitude. Therefore,

$$\hat{A}(\vec{q}) = \mathfrak{F}(\hat{\rho}(\vec{r})) = A(\vec{q}) * \frac{1}{|\vec{q} \cdot \vec{a}_3|}, \quad (4-30)$$

where * denotes a convolution and $A(q)$ is the scattering amplitude as described in Equation 4-16. For the intensity of a Bragg reflection in the z direction a $1/|\vec{q}_z|^2$ behaviour as derived as above in Equation 4-28.

In order to describe the effect of a rough surface we expand on this approach: the effect of roughening can be considered as an effective broadening of the step function. A simple model proposed by Robinson⁶⁰ assumes an exponential distribution of heights where β is a parameter $0 < \beta < 1$ where $\beta = 0$ is perfectly flat and $\beta = 1$ is infinitely rough. Layer 0 is considered to be fully occupied; layer 1 has a fraction β filled, layer 2 has a fraction β^2 filled and so on. The intensity behaviour of Equation (4-25) then becomes

$$I_{rough} = I_o \frac{(1-\beta)^2}{1+\beta^2-2\beta\cos(\vec{q}_3 \cdot \vec{a}_3)} \frac{1}{\sin^2(\frac{1}{2}\vec{q}_3 \cdot \vec{a}_3)}. \quad (4-31)$$

In order to relate β to other roughness models the surface roughness can be expressed as a root-mean-square deviation of the surface contour from a flat surface, σ_{rms} as derived in⁶¹:

$$\sigma = \sqrt{2} \frac{\sqrt{\beta}}{1-\beta}. \quad (4-32)$$

4.5 Reflectivity

Reflectivity is discussed elsewhere in great detail. Dynamical considerations are very important in this case, a good overview of the theory is presented in Tolan⁶² and Foster⁶³ and in Ref. 64. Here we confine ourselves to a brief summary of the key findings. As stated in the International Tables for Crystallography⁶⁵, the refractive index $n(\vec{r})$ for X-rays may be expressed as

$$n(\vec{r}) = 1 - \delta(\vec{r}) + i\beta(\vec{r}) \quad (4-33)$$

where $\delta(\vec{r})$ and $\beta(\vec{r})$ are the dispersion and absorption terms, respectively:

$$\delta(\vec{r}) = \lambda^2 \frac{r_e \rho(\vec{r})}{2\pi} \sum_{j=1}^N \frac{f_j^0 + f_j'(E)}{Z} \quad (4-34)$$

and

$$\beta(\bar{r}) = \lambda^2 \frac{r_e \rho(\bar{r})}{2\pi} \sum_{j=1}^N \frac{f_j''(E)}{Z} = \frac{\lambda}{4\pi} \mu(\bar{r}). \quad (4-35)$$

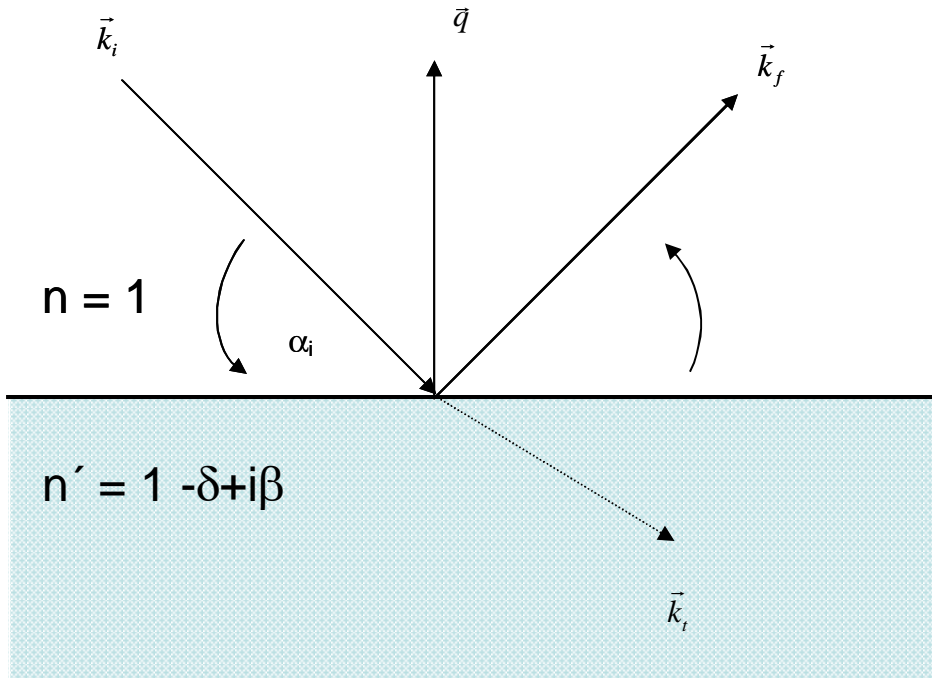


Figure 4-2 Reflection scattering geometry. A plane electromagnetic wave with wave vector \vec{k}_i impinges on a surface at glancing angle α_i . The wave breaks up into a reflected wave \vec{k}_f and a transmitted wave \vec{k}_t .

$\mu(\bar{r})$ in Equation 4-40 is the linear absorption coefficient, f_j is the atomic form factor as described in Equation 4.8 and $f_j'(E)$ and $if_j''(E)$ represent dispersion and absorption corrections in the form $f_j = f_j^0 + f_j'(E) + if_j''(E)$. The values of f_j^0 are q -dependent but this may be neglected in the region of grazing angles of incidence and exit making it possible to simplify the equation for the refractive index in the case of a homogenous medium far away from absorption edges and $f_j^0 \approx Z$:

$$n = 1 - \lambda^2 \frac{r_e \rho(\bar{r})}{2\pi} + \frac{\lambda}{4\pi} \mu(\bar{r}). \quad (4-36)$$

The fact that the index of refraction $n < 1$ for X-rays (Equation 4-33) means that total external reflection occurs when the angle of incidence of an incoming X-ray beam is below the critical angle for total external reflection. It is given by

$$\alpha_c = \lambda \left(\frac{r_e \rho_e}{\pi} \right)^{\frac{1}{2}}. \quad (4-37)$$

Here ρ_e is the mean electron density, $r_e = e^2/mc^2$, and wavelength λ as defined above. The specularly scattered intensity (see Figure 4-3 for experimental geometry) can be analysed using the Parratt algorithm⁶⁶ which is based on a recursive application of the Fresnel law at the interfaces. One can calculate the profile of the electron density in the z -direction and therefore the density profile of layers perpendicular to the sample normal.

4.6 Grazing incidence diffraction

If grazing angles of incidence and exit are chosen, as shown schematically in Figure 4-3, it is possible to keep the momentum transfer almost parallel to the surface and thus we can investigate the in-plane structure. If these angles are kept below or in the region of the angle of total external reflection we can also limit the penetration depth of the X-rays in the sample and obtain structural information on the first few atomic layers. Since for X-rays the refractive index $n < 1$, Bragg scattering occurs under total external diffraction conditions if the angle of incidence of the incoming X-ray beam is held beneath the critical angle α_c (Equation 4-37) as discussed by Dosch¹⁴, Dietrich⁶⁷ and many others^{36, 56,57,68,70}. This technique is particularly useful for probing surface critical and wetting phenomena.

The transmission coefficient of the dielectric boundary for a transparent medium has been calculated by Born and Wolf⁶⁹

$$T = \left| \frac{2 \sin \alpha_i}{\sin \alpha_i + \sqrt{n^2 - \cos^2 \alpha_i - 2\delta}} \right|^2, \quad (4-38)$$

where n is the refractive index and α_i is the angle of incidence. For large angles of incidence $\alpha_i \gg \alpha_c$ the transmission coefficient tends to 1. When $\alpha_i < \alpha_c$ the transmitted wave does not propagate but the field strength at the surface is still described as above and the diffracted intensity from the atoms in the surface layer is proportional to T . The signal is, therefore, enhanced by a factor of 4 when the incidence ray impinges at exactly the critical angle α_c . The diffracted beam experiences refraction in exactly the same way, so that in the absence of absorption a second factor of 4 may be obtained when the angle of exit from the surface α_f is equal to α_i . This can be seen in Figure 4-4.

The observed scattering originates from a scattering depth

$$\Lambda = \frac{\lambda}{2\pi(l_i + l_f)} \quad (4-39)$$

with

$$l_{i,f} = 2^{-\frac{1}{2}} \left\{ (2\delta - \sin^2 \alpha_{i,f}) + \left[(\sin^2 \alpha_{i,f} - 2\delta)^2 + 2\beta^2 \right]^{\frac{1}{2}} \right\}. \quad (4-40)$$

If absorption is ignored Snells law predicts that Λ can also be expressed in terms of k where $\vec{k}_{i,z} = \vec{k} n \sin(\alpha_i)$ and n is the refractive index as above⁷⁰

$$\Lambda = \frac{1}{2k\sqrt{\alpha_c^2 - \alpha_i^2}} \quad (4-41)$$

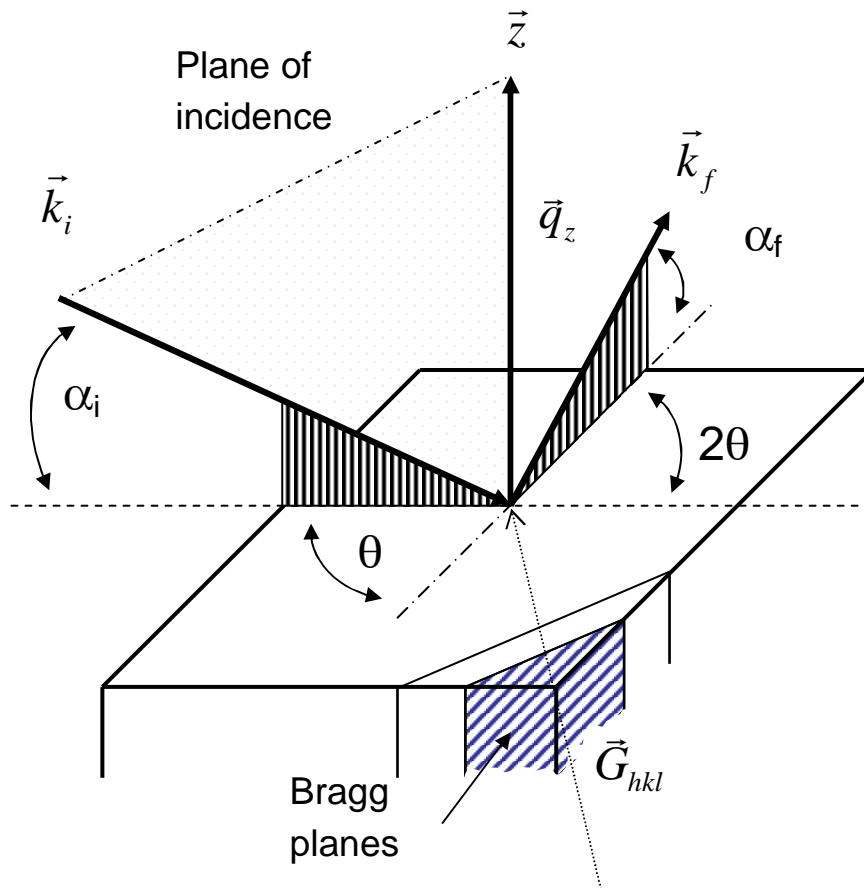


Figure 4-3 The grazing incidence geometry of the X-ray beam impinging on the surface at an angle α_i . After diffraction through an angle of 2θ the X-rays exit the surface at an angle α_f . The momentum transfer \vec{q} is composed of an in-plane component \vec{q}_{\parallel} and a \vec{q}_z component normal to the surface and provides information on the in-plane structure of a sample.

This means that for $\alpha_i \ll \alpha_c$ Λ is equal to $(2k\alpha_c)^{-1}$ which is only material-dependent and not wavelength-dependent (see Equation 4-37). For NbSe₂ $(2k\alpha_c)^{-1}$ is 24 Å, while for gold it is 12 Å. The behaviour of Λ with changing α_i is shown in Figure 2-1.

The intensity for any kinematic scattering intensity (I_{GID}) observed close to the total external reflection condition is

$$I_{GID}(\vec{Q}') \propto |T_i|^2 F(\vec{Q}') |T_f|^2, \quad (4-42)$$

the product of the squares of the incident and transmitted beam transmission functions and the surface diffraction intensity. The dependence of $|T_i|^2$ on α_i/α_c is seen in Figure 4-4, the enhancement in the region of α_c is evident. In practice it is preferable to measure away from the critical angle so that the intensity is not so sensitive to slight changes of angle in the incoming beam or sample vibration. Generally for surface X-ray diffraction the advantage of measuring close to or below the critical angle is lower background simply because less of the bulk is penetrated. In grazing incidence measurements the incidence angle is often deliberately varied in order to achieve a depth profile of the sample.

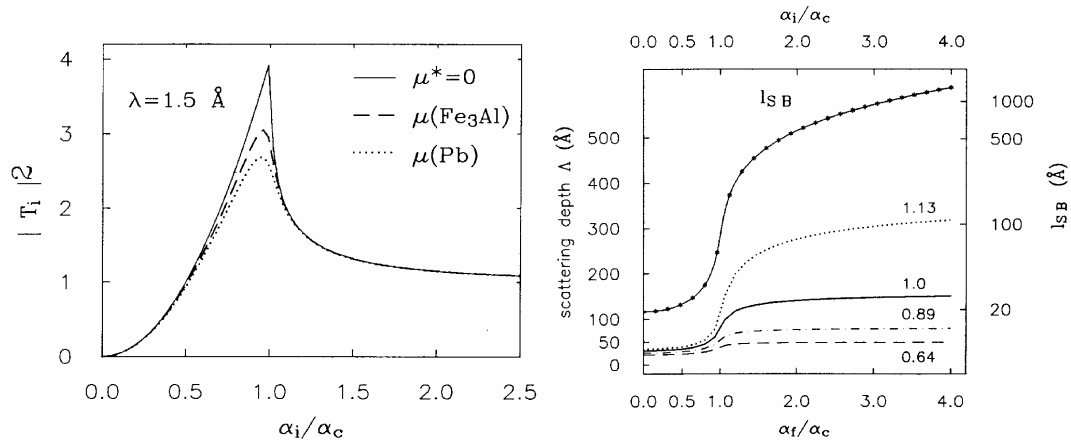


Figure 4-4 (a) Fresnel transmission $|T_i|^2$ as a function of α_i/α_c for a transparent medium and for Fe₃Al and Pb¹⁴. (b) On the left side the scattering depth Λ is shown as a function of α_i/α_c for various values $\alpha_i/\alpha_c = 0.64, 0.89, 1.0$ and 1.13 . The solid curve marked with asterisks shows the penetration depth of the specular beam as a function of α_i/α_c on a logarithmic scale (after 14).

5 Experimental set-up

5.1 Introduction

The essential experimental components for the study of the charge density wave phase transition in a single crystal of 2H-NbSe₂ are presented in this chapter. The sample preparation is outlined, the sample environment and the instruments used for the X-ray diffraction measurements are described. The experiments discussed in this thesis were carried out in Kiel on the two rotating anode sources as described in the thesis of Seeck⁵⁵ and in particular at a number of different beamlines at the HASYLAB and ESRF synchrotron radiation sources. The principal technique employed was grazing incidence diffraction as discussed in the previous chapter. Standard X-ray diffraction, X-ray reflectivity and surface X-ray diffraction were also carried out at the XMaS beamline at ESRF.

5.2 Sample preparation

The single crystal 2H-NbSe₂ sample, prepared by Bell Labs, had dimensions of 8 x 4 x 3 mm³. The samples were prepared by iodine vapour transport using a narrow ampoule with a long two stage annealing process⁷¹. This process results in high-quality, thick crystals with a low mosaic width, FWHM (0.0025 ± 0.0003) Å⁻¹ for the 200 reflection, which is ideal for grazing incidence diffraction.

For these experiments the samples were cleaved prior to measurements using librarian Scotch tape. Initially the more conservative approach of using a cleaving bar glued to the sample surface was employed but the results were unsatisfactory. It was difficult to achieve the removal of a complete layer and often the sample cleaved in the middle or even close to the base. A single cleave rarely produced an acceptable surface. The success was much greater using book Scotch tape. The stiff, foil like nature and gentle adhesion properties of the tape proved to be ideal for removing the top layers of the layered sample in an effective manner. There are often many cleaves required, on average about fifteen attempts, to achieve an intact surface layer. Using this technique a clean, optically flat, shiny surface was obtained.

For most experiments the samples were cleaved at the beamline, then immediately mounted on the cryostat and cooled in the cryostat for the measurements. A pressure of 10^{-7} mbar was maintained in the cryostat throughout the measurements.

5.3 Cryogenic temperatures

The CDW phase transition in NbSe₂ occurs at about 33 K. In order to investigate the behaviour at the phase transition, a temperature range of 15 to 60 K was required. Therefore, a closed cycle He cryostat was used for the measurements. The low-temperature operation of a closed cycle cryostat is achieved by using high-pressure helium gas to produce cooling down to 10 K. A helium compressor provides high pressure gas to the cryo-cooler through a flexible gas line. The expansion of the gas at different stages gives rise to the refrigeration. Low-pressure gas is then returned through another gas line where it is recycled through the compressor. This can be continuously repeated, leading to a closed loop, and maintained as needed to achieve the required temperature.

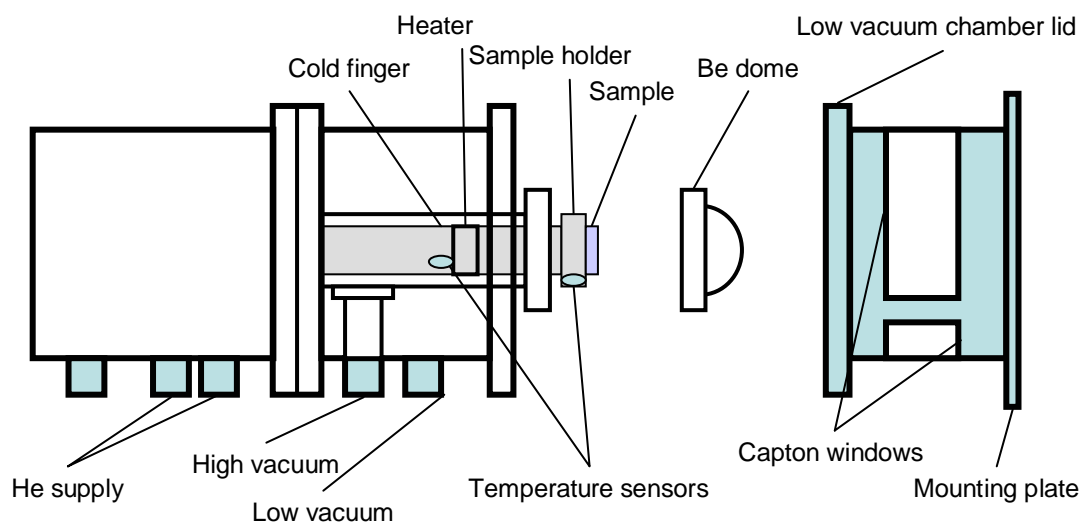


Figure 5-1 A schematic diagram of the Kiel Leybold RGD 1245 cryostat used on the BW2 beamline at HASYLAB.

A number of different cryostats were used depending on which beamline was used. At HASYLAB, a Leybold RGD 1245 coldhead and a RW5 compressor were used in conjunction with a pair of class A Pt100 temperature sensors as outlined schematically in Figure 2-1. One was placed at the sample holder and the second close to the heater on the cold finger. Temperature regulation was carried out by a Lakeshore 330 temperature controller, using the Pt100 temperature sensor at the

sample holder as reference (sensitive over the range 20 to 300 K). The sample was mounted on a copper block fastened on top of the cryostat cold finger. In order to improve thermal contact, an indium foil was placed between the copper holder and the copper coldhead. The sample mount and the cold finger were covered by a beryllium dome allowing UHV pressures of 10^{-7} mbar to be reached while simultaneously allowing X-ray transmission to the sample. A secondary vacuum was provided by a copper can with capton windows (also X-ray transmissive). The whole housing weighing about 30 kg in total was attached to the diffractometer via a mounting plate consisting of four 20 mm support poles and a base plate. The sample environment had to be supported with a counter weight throughout the experiment in order to maintain stability in the sample position and to allow the diffractometer to move with sufficient accuracy.

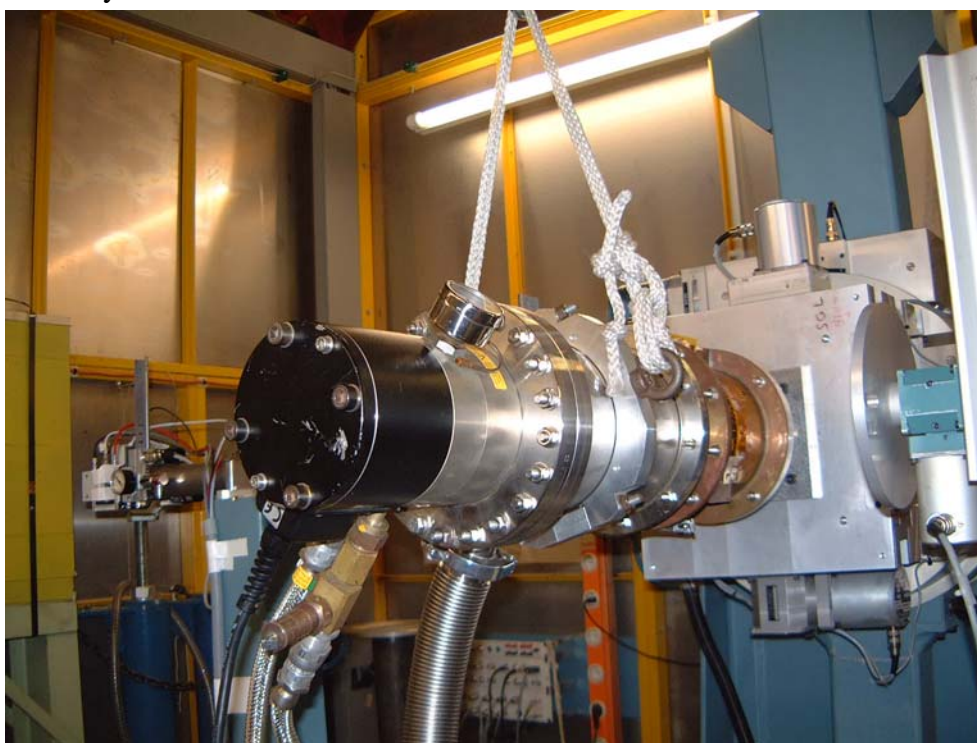


Figure 5-2 Close up of the Leybold RGD 1245 Cryostat at BW2, HASYLAB.

For all ESRF experiments an ARS DE202G closed cycle cryostat was used for refrigeration and calibrated silicon diodes for temperature readout in the range 1 to 350 K. The temperature controller used on both beamlines was the Lakeshore model 340 (temperature stability ± 0.01 K). This cryostat was much smaller and lighter (approximately 10 kg) and so could be mounted directly on the diffractometer without the need for a counter weight.

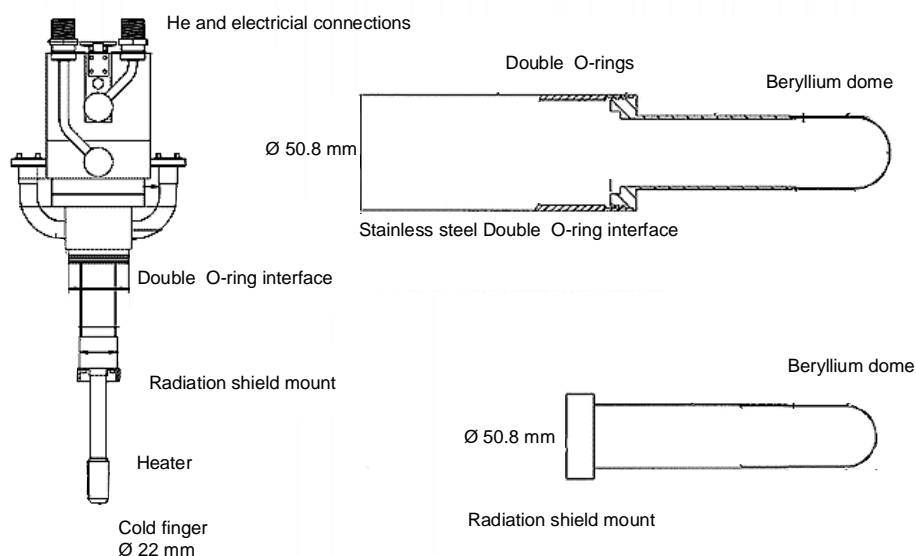


Figure 5-3 Schematic diagram of the ARS DE202G closed cycle cryostat.

5.4 Laboratory X-ray sources

In the course of this work X-ray radiation was used. The characterisation measurements on the early samples were carried on the rotating anodes at Kiel. In the case of a rotating anode X-ray tube electrons are emitted providing a broad continuous background spectrum of radiation known as bremsstrahlung caused by the sudden deceleration of the electrons as they impact the anode. This radiation extends spectrally out to long wavelengths with decreasing intensity and down to a minimum wavelength corresponding to the wavelength of a photon that carries away all the kinetic energy of an electron incident on the anode. Superimposed on the bremsstrahlung continuum is an almost monochromatic set of X-ray lines that reflect the atomic structure of the atoms of the anode. This characteristic radiation is produced when a high-energy electron impacts the anode and knocks out an inner shell electron from an anode atom. An X-ray photon is emitted when the vacancy thus created is filled by means of a downward transition made by an electron in one of the higher energy shells. Due to spin-orbit interaction a splitting can occur. A copper anode was used in Kiel and there the important emission lines are K_{α} ($\lambda = 1.541 \text{ \AA}$, used for the experiments) and K_{β} ($\lambda = 1.392 \text{ \AA}$).

5.5 Synchrotron radiation

In the case of a synchrotron highly intense collimated X-rays are produced over a wide spectral range from far extreme infra-red to hard X-rays. The beginning is

similar to a lab source. Electrons are produced from a thermionic emitter. They are then accelerated up to an energy of approximately 1 MeV as they are fed into a booster ring. In the booster ring the acceleration continues until all the electrons have an energy of several hundred MeV. Then they are injected into a larger ring called a storage ring. Here they are accelerated up to 6 GeV. At this stage the electrons are travelling at relativistic speeds and so they give off synchrotron radiation in the tangential direction. This X-ray radiation is extremely collimated and has a high intensity, i. e. high brilliance. The intensity of the radiation can be increased by using an insertion device such as a wiggler or an undulator. The X-ray beam is then transported to an end station via a series of optical elements. As the beam is polychromatic, often a monochromator is used to select a single wavelength for the experiment. There are many reviews of synchrotron radiation techniques. A general introduction to synchrotron radiation is given by Margaritondo⁷² and Duke⁷³.

5.6 XMaS

The XMaS beamline is a bending magnet beamline and provides X-rays in the energy range 3 to 15 keV. The optical layout is shown schematically in Figure 5-4.⁷⁴ The first optical component is a double-crystal silicon (111) monochromator. The first crystal is water cooled and absorbs most of the incident synchrotron radiation power. It is followed by an uncooled toroidal mirror that focuses the beam to a small spot onto the sample surface. The mirror surface has been coated with a thin layer of Rhodium to enhance reflectivity. The beam is focused at the sample position; the diffractometer is located 50 m from the source.

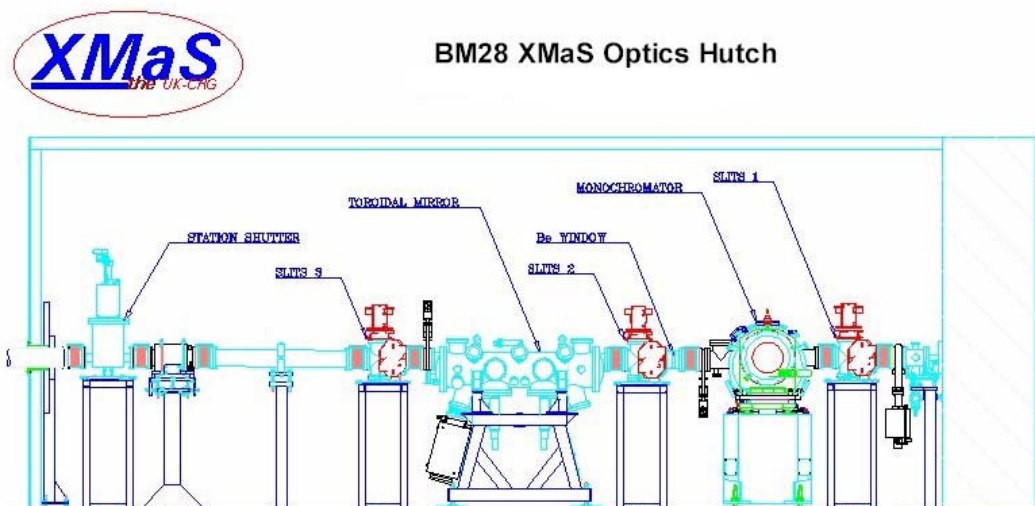


Figure 5-4 A schematic figure of the XMaS beamline, ESRF, showing the principle optical components.

The 11 axis diffractometer at BM28 provides the option of using a horizontal or vertical four circle scattering geometry. The vertical geometry was used for these reflectivity and diffraction measurements. The experiment was carried out at 10 keV in order to maximize intensity. The cyber star scintillation single element detector was used for data collection. The sample was cleaved as described in section 5.2 and directly mounted on the cryostat.

Extended reflectivities were collected at 10 and 40 K in order to characterise the surface roughness and to see if there was a surface layer present. 00 l truncation rod scans were performed to approximately 006 at 10 K and 40 K in order to investigate the temperature dependence in the out of plane direction.

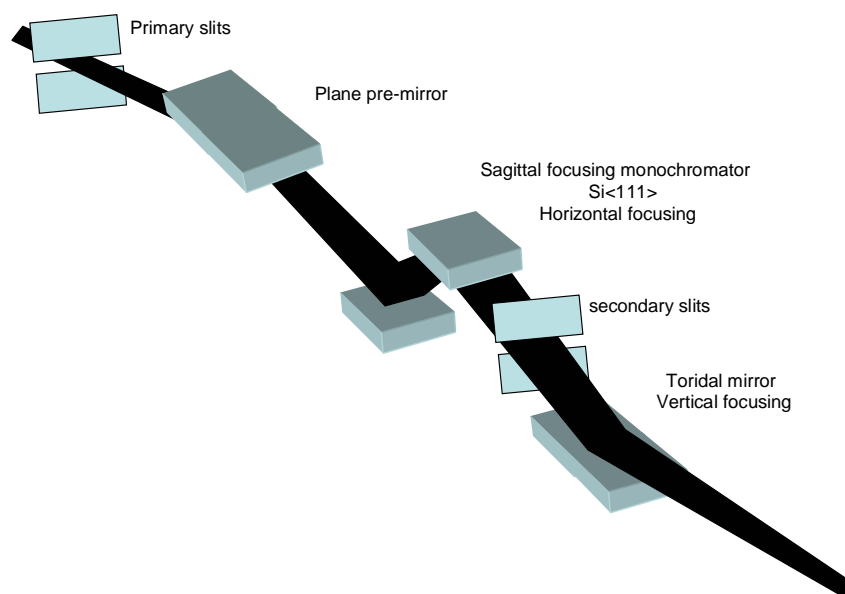


Figure 5-5 Schematic layout of the wiggler beamline optics at BW2, HASYLAB.

5.7 BW2

The first GID experiments were performed at the BW2 beamline⁷⁵, HASYLAB, DESY. The BW2 beamline is designed to provide a high intensity monochromatic beam in the energy range 2.5 to 25 keV. The principal optical elements consist of a plane pre-mirror and a (+/-) double crystal fixed-exit Si (111) monochromator⁷⁶. A sagittally bent second monochromator crystal and a tangentially bent mirror in the monochromatic beam provide focusing (Figure 5-5). A photon flux of $4 \times 10^{12} \text{ s}^{-1}$ total is available at the sample (9 keV, 70 mA ring current).

We used the Risø four-circle diffractometer for these grazing incidence diffraction (GID) measurements. The experiment was carried out at an energy of 9.5 keV in order to maximise intensity. The sample was cleaved in air and then mounted under a Be

dome, on the cold finger of a closed-cycle Helium cryostat (minimum temperature 25 K, see 5.3). The cryostat was mounted directly on the BW2 diffractometer (Figure 5-6). The incident beam was defined by slits of dimensions $0.5 \times 1 \text{ mm}^2$ (horizontal x vertical) giving an illuminated sample area of about 2 mm^2 . For the scattered beam 1 mm horizontal slits with a position sensitive detector collecting over a vertical range of 20 mm were used. This resulted in a q -space resolution of 0.005 \AA^{-1} in the vertical diffraction plane (Figure 5-7).

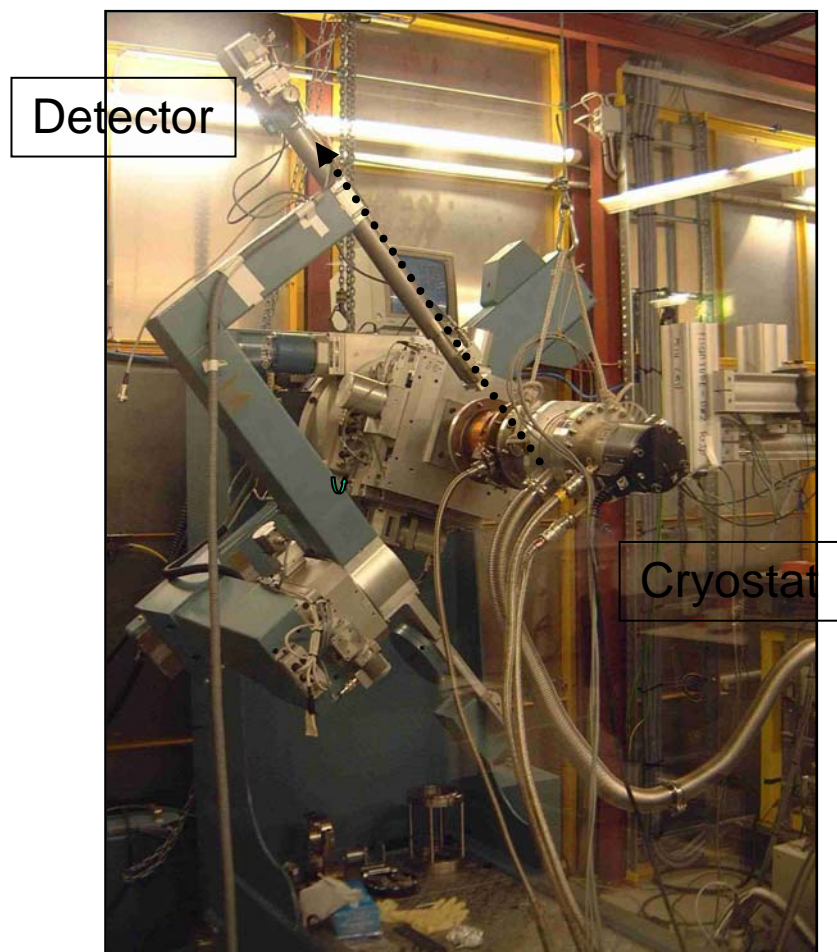


Figure 5-6 Kiel cryostat mounted on the 6 circle diffractometer at BW2 in HASYLAB. The X-ray beam entering from the right, is diffracted by the sample in the vertical plane into the detector. The capton window on the outer vacuum chamber of the cryostat can be seen. The detector is housed at the end of an evacuated tube in order to minimise air scattering while optimising resolution. The cryostat is fastened to the diffractometer via a mounting plate and is supported via a counter weight. The supports are seen above the cryostat.

Even though we were illuminating a sizeable area of the sample, the characteristic transmission curve from a single terrace could be observed at the position sensitive detector throughout this experiment. The depth resolution was therefore not limited by the sample but the cost was a loss of total intensity. The position sensitive detector signal integrated over α_f was taken as the peak intensity for our study.

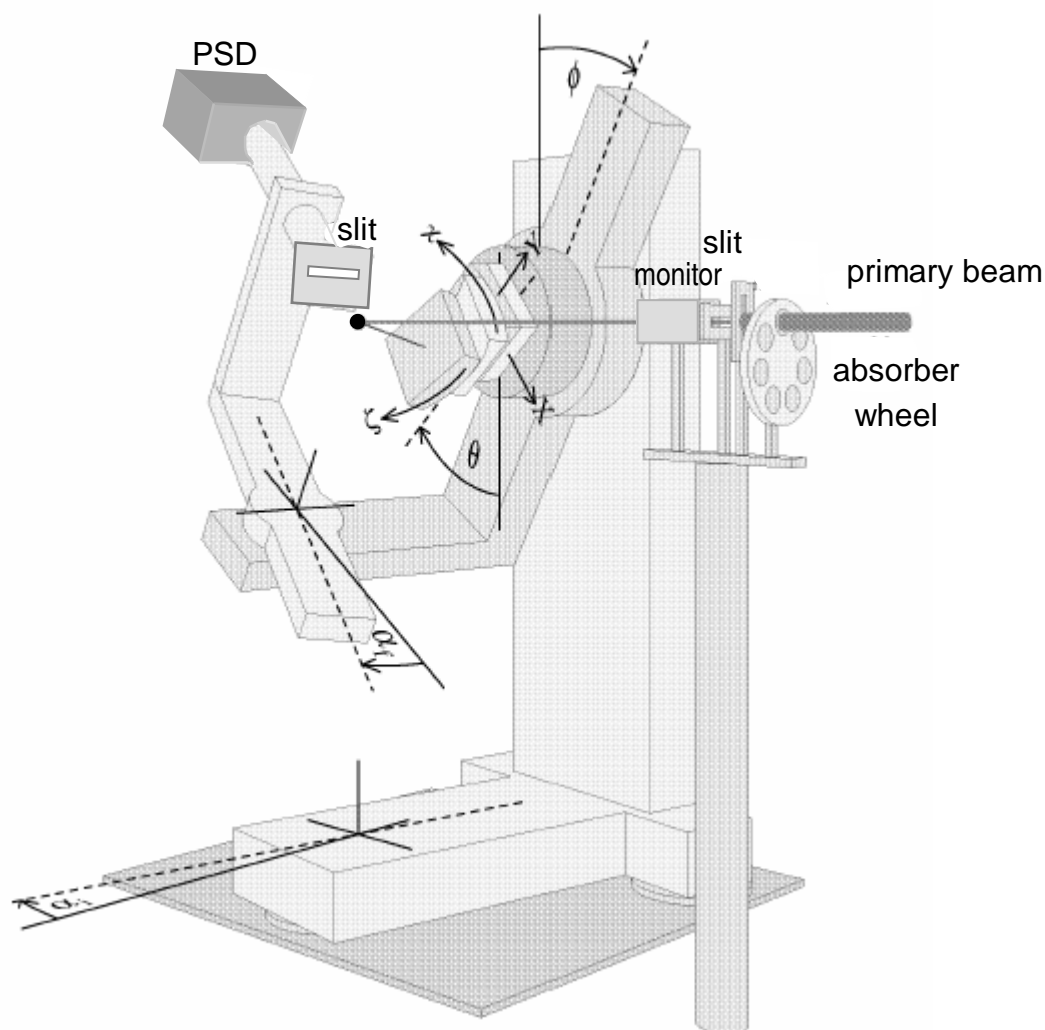


Figure 5-7 The grazing incidence geometry at BW2. Note that the angle of incidence α_i can be set by rotating the whole diffractometer independently of sample alignment.

The out of plane sample surface quality was first confirmed with a reflectivity scan by placing 1 mm horizontal slits in front of the detector and varying the angle of incidence and the detector in a theta / two theta scan. Following this, in the temperature range 25 to 45 K GID Bragg scans were then performed at the CDW satellite reflection $q(\frac{5}{3} 0 0) = 3.513 \text{ \AA}^{-1}$ and at a reference reflection $q(2 0 0) = 4.215 \text{ \AA}^{-1}$ (see Figure 5-8). The detector signal was integrated over α_f . The experiments were performed at 8 keV initially and later at 9.5 keV in order to maximise flux at BW2. At 9.5 keV the critical angle of total external reflection for NbSe_2 is 0.225° . Below this, we are in a surface sensitive geometry and at angles greater than the critical angle have a bulk sensitive geometry^{67,56,57,70}. The CDW satellite reflection and a reference reflection were measured at a low incidence angle ($\alpha_i = 0.17^\circ$, penetration depth $\sim 24 \text{ \AA}$) and then at an increased incidence angle ($\alpha_i = 0.4^\circ$, penetration depth $\sim 1,500 \text{ \AA}$),

to increase bulk sensitivity. Temperature steps of 0.1 K were required in the region of the phase transition. Due to the low intensity of the satellite reflection, the signal-to-noise ratio was just 3.5 to 1 even at 25 K, therefore counting times were very long especially close to the transition temperature where a single Bragg scan at the $^{5/3}00$ position required 2 hours. Over the temperature range we monitored the order parameter (a function of satellite peak intensity) and the satellite diffuse scattering intensity.

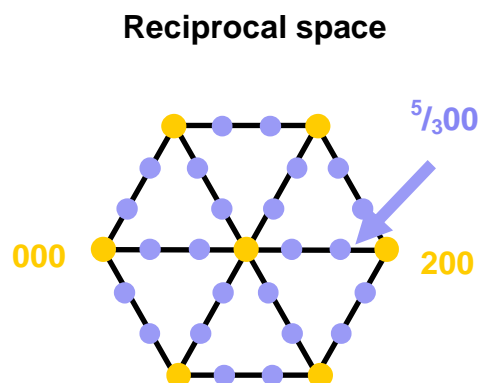


Figure 5-8 A reciprocal space picture for the hexagonal structure of NbSe₂ is shown above. The yellow dots represent the Bragg reflections resulting from the NbSe₂ structure and the blue dots are due to the charge density wave superlattice Bragg reflection. Data were collected at the 200 Bragg reflection and at the nearby $^{5/3}00$ superlattice reflection.

5.8 ID1

The ID1 beamline at ESRF provides X-rays in the energy range 2.1 keV to 35 keV provided by the combination of a 42 mm undulator with 38 periods and a 70mm wiggler⁷⁷. The calculated flux available at the sample is 4.4×10^{13} photons /s at 8 keV. For this experiment, in order to maximize intensity and minimize penetration depth, an energy of 10.37 keV was chosen.

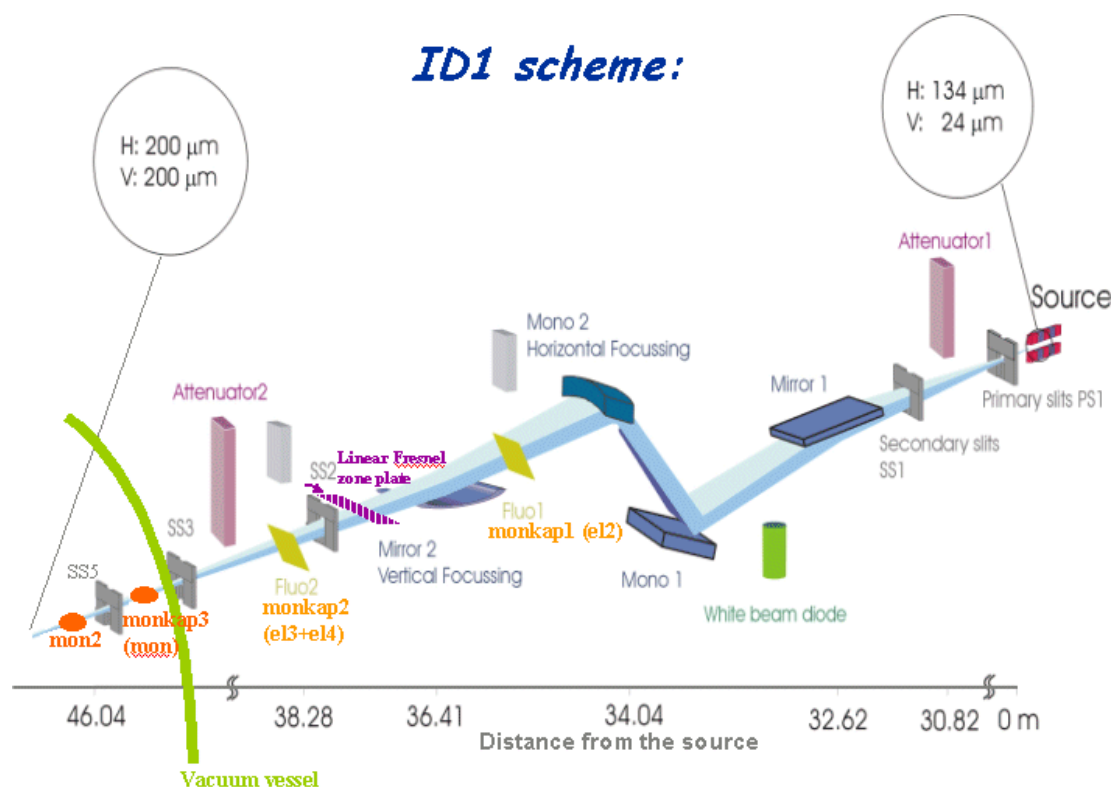


Figure 5-9 Schematic layout of the ID1 beamline optics layout (courtesy of T. Metzger).

The ID1 optics (Figure 5-9) consist of a double-crystal monochromator located in between two mirrors providing a fixed-exit monochromatic beam. The X-ray fan is vertically reflected by a liquid nitrogen cooled Si-premirror which provides a beam almost parallel to match the vertical divergence to the acceptance angle of the first flat Si monochromator (also liquid nitrogen cooled). The full horizontal divergence of the source is accepted by the second Si crystal which provides sagittal focusing. A fixed beam-stop located after the monochromator vessel intercepts the white beam and the bremsstrahlung radiation. Finally meridional focusing is achieved via a second Si-mirror which also provides harmonic rejection.

The four-circle diffractometer at ID1 was used for these grazing incidence experiments in order to achieve the high flux and low divergence we required.

The cryostat was mounted on a Huber tower on the beamline diffractometer. The configuration is shown in Figure 5-10. The single crystal 2H-NbSe₂ sample was mounted, under a Be dome, on the cold finger of a closed cycle ARS DE202G He cryostat (minimum temperature 18.5 K). Data were collected at 9.5 keV in order to maintain a low penetration depth and thus surface sensitivity for our experiment.

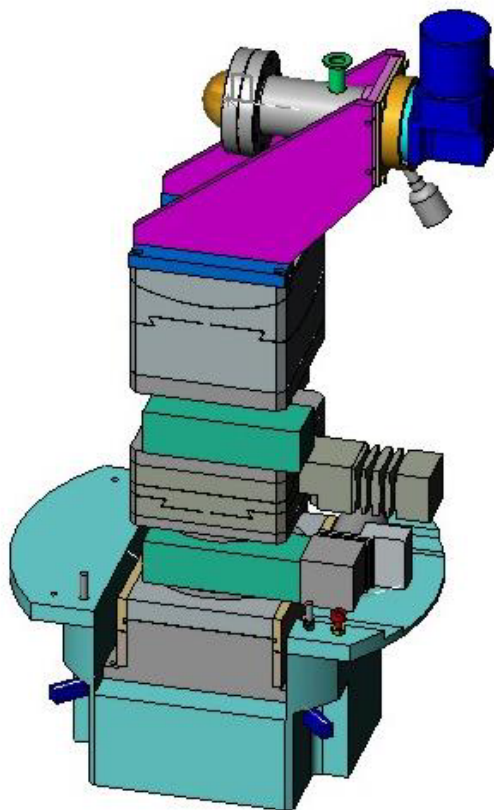


Figure 5-10 Schematic diagram of the ID1 Huber tower with the cryostat mounted.

Grazing incidence diffraction was carried out at the 200 Bragg peak and the $^{5/3}00$ satellite (appearing below 33 K) over the temperature range 18.5 to 60 K to study temperature-dependent behaviour in the region of the phase transition. Over the temperature range we monitored the order parameter of the charge density wave satellite reflection (a function of peak intensity), and the degree of diffuse scattering. Temperature steps of varying sizes were chosen. They were as small as 0.1 K in the region of the transition. Bragg scans were made along the q_z direction on both the Bragg and the satellite peak at angles below the critical angle to achieve surface sensitivity and then above to obtain bulk reference measurements over the entire temperature range.

6 Experiments and analysis

6.1 Introduction

The principal techniques of X-ray diffraction employed in the realm of this thesis were presented in the previous chapter. In this chapter the experiments and results of grazing incidence X-ray diffraction (GID) investigations on NbSe₂ are presented. In these experiments we employ GID techniques in order to compare charge density ordering at the surface and in the bulk over the temperature range of 18.5 K to 60 K. The intensity of a superlattice reflection is proportional to the square of the order parameter $I \sim |F|^2 \sim |m^2|$. Therefore, from an investigation of the temperature dependence of the charge density wave satellite reflection one can also determine the order parameter for both the surface and the bulk.

In section 6.2 a summary of samples measured is presented and the difficulties in growing a layered crystal suitable for grazing incidence diffraction is discussed. Then in section 6.3 the characterisation of the sample grown by Oglesby *et al.*⁷¹ is presented. In sections 6.4 a first experiment carried at BW2 is reported. In 6.5 an *in situ* UHV experiment is discussed. Results from grazing incidence measurements on beamline BW2 at HASYLAB are shown in 6.6 and compared with the data collected at the ESRF on beamline ID1 (6.7). All results are discussed in section 6.8 and summarized in 6.9.

The data collected during these experiments are shown. The analysis procedure is outlined, the results are presented and an interpretation is offered.

6.2 Samples

The ideal sample for X-ray diffraction measurements with NbSe₂ is a perfect single crystal of a single polytype with an optically flat surface. In reality there are only a few materials, such as silicon, which display properties close to ideal. Sample quality becomes an even greater issue once one begins to investigate systems other than metals or classical semiconductors. For layered crystals growing single crystals is a major challenge. The growth of high quality single crystals of transition metal dichalcogenide layered crystals has been a limiting factor in this area of research since

the 1970's^{1,2}. Even today NbSe₃, also a layered crystal, can only be grown as tiny whiskers 20 x 40 x 600 μm³ as described in Ref. 78.

As previously discussed in chapter 5, the mosaicity of samples must be low if a good depth resolution is to be achieved in GID. The full width half maximum (FWHM) of a sample obtained from a rocking scan is a good measure of the mosaicity of a crystal; a high quality crystal will have low FWHM tending towards a delta function for a perfect crystal. Layered crystals are rarely high quality single crystals and have a broad mosaic width which can be of the order of degrees. In the first year of this project many samples were tested and found to have a mosaicity outside the acceptable range. One would require a FWHM of the rocking curve of less than 0.05° in order to preserve depth sensitivity. In a sample with a broad rocking curve the depth resolution is washed out as the critical angle of total external reflection for NbSe₂ is just 0.29° (at 10 keV).

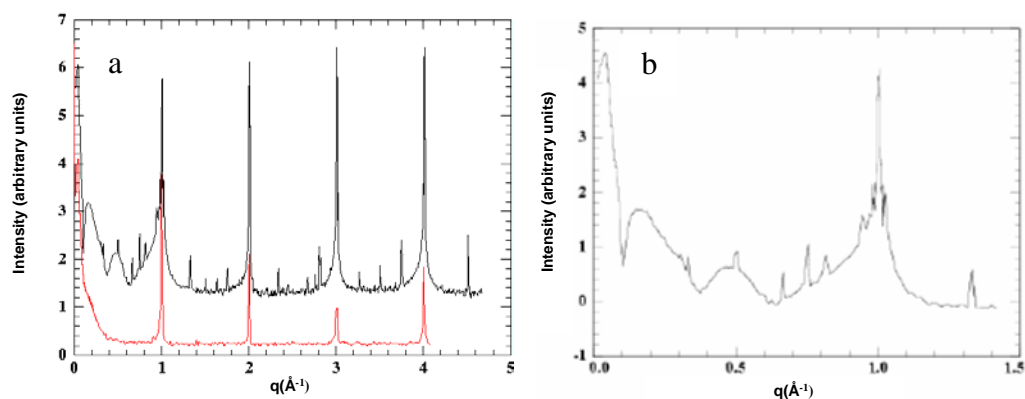


Figure 6-1 NbSe₂ samples grown in university of Bayreuth (red) and in Kiel (black) were measured on the laboratory X-ray source in Kiel. Extended reflectivities were measured for both samples (a). The reflectivity in the region up to $q = 1.5 \text{ \AA}^{-1}$ including the 002 reflection is shown for the upper sample (b). The oscillations at are due to a layer of about 34 Å. A more detailed discussion is carried out in the text below.

In Figure 6-1 diffraction diagrams of samples grown at University of Bayreuth in the group of Prof. Van Smaalen and of samples grown at the University Kiel by the group of Prof. Skibowski measured in the course of this thesis are shown. Samples from University of Konstanz in Prof. Meerchaut's group were also measured. The typical structure for 2H-NbSe₂ can be observed with Bragg reflections occurring at $q \approx 1, 2, 3, 4 \text{ \AA}^{-1}$. In Figure 6-1b a close-up of the reflectivity in the region up to $q = 1.5 \text{ \AA}^{-1}$ is shown.

Rocking curves were also measured for many samples to investigate the crystal quality. Figure 6-2 shows data measured on the laboratory X-ray sources in W. Press's working group in Kiel. These rocking curves from NbSe₂ illustrate the difficulty in growing samples of sufficient quality for X-ray diffraction studies. The

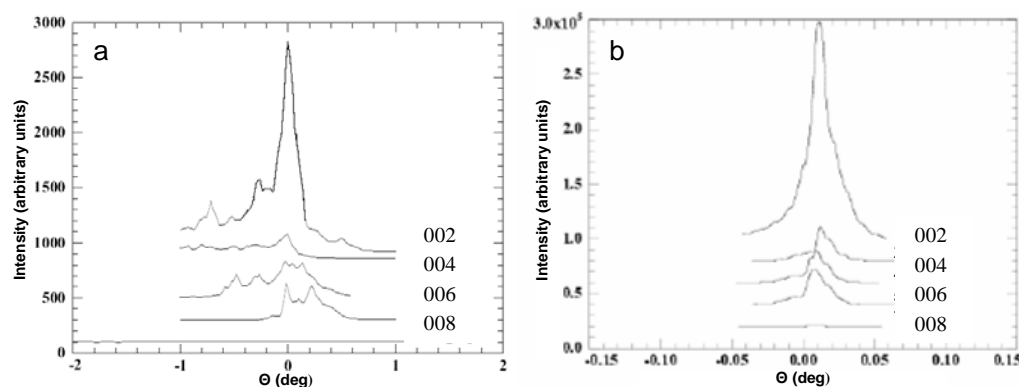


Figure 6-2 Typical rocking curves measured for initial NbSe₂ samples on the Kiel X-ray diffractometer. The width of the rocking curve can be related to the mosaic spread for the sample. The presence of multiple peaks in the rocking scan shows that the crystal is faceted (a, Bayreuth sample). In (b) sample skib2 (Kiel) with a lower mosaic spread is shown, the FWHM is 0.025°. However, as one sees the intensity falls off rapidly for the higher order reflections.

samples measured had full widths over the range 0.05° to as big as 0.5°. Initially the size of these samples was also far from ideal, ranging from thin whisker of samples to a volume of 1 x 1 x 1 mm³ or samples with a larger surface area, such as 10 x 10 mm² but a thickness of less than 100 μm.

All samples, though grown in different laboratories, were produced using Iodine transport methods as described in 5.2. A significant improvement in sample quality is observed in the rocking curve shown in Figure 6-4. This was measured on a sample grown by C. Oglesby⁷¹ which has an excellent quality. The growth method differed from the others in that the annealing time was extremely long, 6 weeks in total.

Variation of the stacking structure of successive NbSe₂ layers along the hexagonal *c* axis can lead to a large variety of crystal structures or polytypes. Therefore, one must also consider the polytype components of a crystal. For X-ray diffraction studies one would ideally have a single polytype present, i.e. just the 2H form in this case. For the 2H-polytype one expects to observe Bragg peaks only 00*l* with *l* = 2, 4, 6, 8. The presence of additional peaks at non-integer values of *q_z* indicates that the crystal is not purely single crystalline but contains some domains of other forms. For grazing incidence measurements there is the additional requirement that the surface is flat, optically displaying no protrusions or bending, and with a low atomic roughness.

6.3 Sample characterisation

The 2H-NbSe₂ sample grown by Oglesby⁷¹ is discussed here. It was found to be an ideal crystal for this study, 2 mm thick, 4 mm wide and 8 mm long. This sample was significantly bigger than all previous ones. The sample was initially almost perfectly flat though later after cleaving many times a slight bend observed at over the last

millimetre at one end of the crystal. The side faces of the crystal were also crystal facets. Indeed, in a previous experiment on the same sample, Du *et al.* measured diffraction not only from the top but also from the side of the sample³. The experiments presented in this chapter were carried out on this high-quality sample.

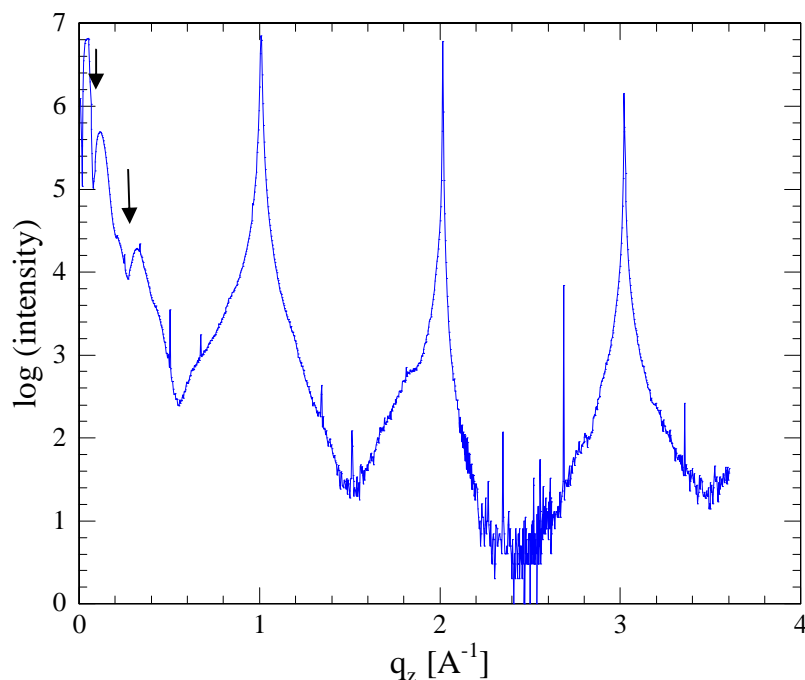


Figure 6-3 The extended reflectivity or 00 l truncation rod scan from $l = 0$ to approximately 7. Data were collected on the XMaS beamline at the ESRF.

A reflectivity of the Oglesby sample as measured on the XMaS beamline at the ESRF, at 10 keV is shown in Figure 6-3. A standard θ - 2θ reflection geometry was used as outlined in chapter 5. The high surface quality of this sample is clear from the almost seven orders of magnitude of intensity observed in the reflectivity. The high degree of crystallinity can be quantitatively measured in the rocking curves which for this sample have a FWHM of only 0.005° or $2.5 \cdot 10^{-4} \text{\AA}^{-1}$ (Figure 6-4) and is an order of magnitude improvement on our previous best value of 0.05° for a sample with a good reflectivity. This is remarkable for a layered crystal. If one compares the extended Bragg scan of sample Skib1 (Figure 6-1) with that of the Oglesby sample shown in Figure 6-5 one can see that the relative intensity of the 2H-peak to other reflections is greatly increased. This is indicative of a sample with a high contribution from a single polytype. There are many discussions of the nature and relevance of polytypes in the literature such as Refs. 19,21.

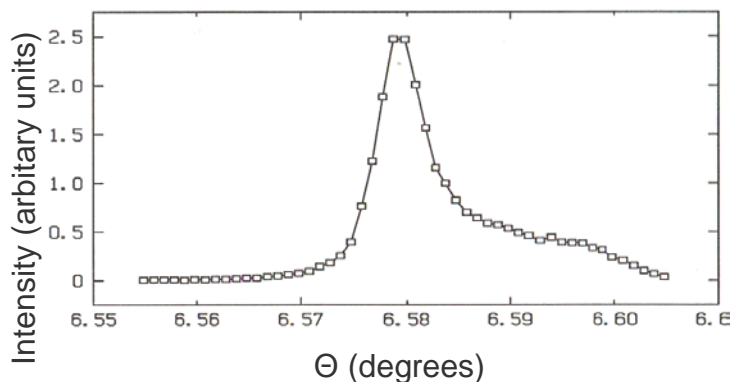


Figure 6-4 Rocking curve of NbSe₂ measured on ID1. The FWHM is 0.005°.

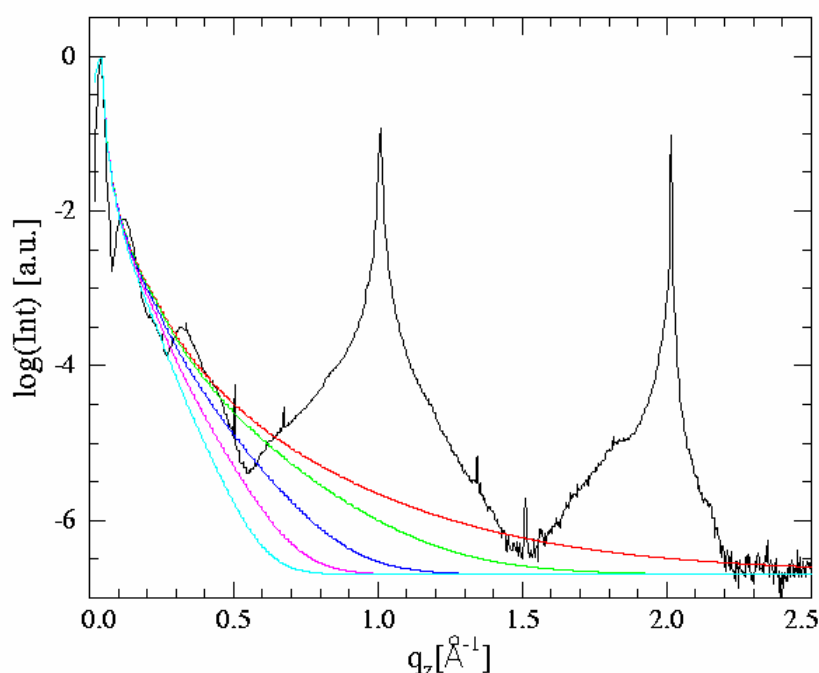


Figure 6-5 Reflectivity of the Oglesby sample measured on the XMaS beamline at the ESRF. The roughness estimated from the data is less than 3 Å. The coloured lines indicate the calculated reflectivities: red 0 Å, green 1 Å, blue 2 Å, purple 3 Å, cyan 4 Å.

Bragg peaks present at $q \approx 1, 2, \text{ and } 3 \text{ \AA}^{-1}$ are due to the NbSe₂ 002, 004 and 006 reflections. The occurrence of the 00 l reflections at integer positions in q is purely coincidental and is due to the fact that the c -axis of 2H-NbSe₂ is approximately 4π ($c = 12.547 \text{ \AA}$)¹⁹. The presence of intensity spikes at 0.5 and at 0.7 \AA^{-1} and later in the 00 l scan are due to a small contribution of some other polytypes in the mainly 2H-sample. The relative intensity of the ‘other’ polytypes is quite small. The presence of an additional oscillation with dips at $q = 0.07967 \text{ \AA}^{-1}$ and $q = 0.2742 \text{ \AA}^{-1}$ gives a period $\Delta q = 0.1946 \text{ \AA}^{-1}$ and shows that there is a layer of about 32 Å present probably at the surface of the crystal. This is likely to be surface layer relaxation over the top layers of NbSe₂. The roughness of the sample has been estimated to be less than 3 Å (Figure 6-6). In order to investigate a temperature dependence on the surface

relaxation, data were collected at 12 K and 40 K. No temperature dependence was observed in the truncation rod scans. Therefore, we can say that the surface relaxation is not temperature dependent. In summary, the Oglesby sample is a high quality 2H-NbSe₂ sample with a low roughness and it has a surface layer of about 32 Å thickness.

6.4 Data from BW2

The initial GID measurement at BW2 on the Oglesby grown NbSe₂ sample was carried out as described in chapter 5. The sample was acetone degreased but not cleaved for this experiment. It was mounted on the Kiel cryostat on the 6 circle diffractometer at BW2. The beam size was set to 0.5 x 1 mm² (horizontal x vertical) and the post sample slits 1 mm vertical. As a position sensitive detector was used the signal was integrated over α_f . Even in this exploratory experiment the sample showed some very interesting results. For this experiment an energy of 8 keV was chosen to maximise surface sensitivity. The $^{5/3}00$ satellite reflection intensity was measured. As the amplitude is proportional to the CDW lattice distortion it can be considered to be an indicator of the order parameter for the sample. The raw data collected at two separate incidence angles is shown in Figure 2-1. The charge density wave satellite reflection and a reference reflection (200) were measured at a surface sensitive incidence angle and then at a bulk sensitive incidence angle at each temperature step. The critical angle of total external reflection for NbSe₂ is 0.34° at 8 keV. The surface sensitive data were collected first at an incidence angle below the critical angle of total external reflection ($\alpha_i = 0.2^\circ$) resulting in a penetration depth of about 23 Å. The incidence angle was then increased beyond the critical angle of total external reflection to increase bulk sensitivity ($\alpha_i = 0.45^\circ$, penetration depth ~ 1,000 Å). A difference in the line shape of the $^{5/3}00$ satellite reflection on the surface and in the bulk was observed. Strong temperature dependence was also seen. There was enough information in the data to decide that the sample was worth further investigation.

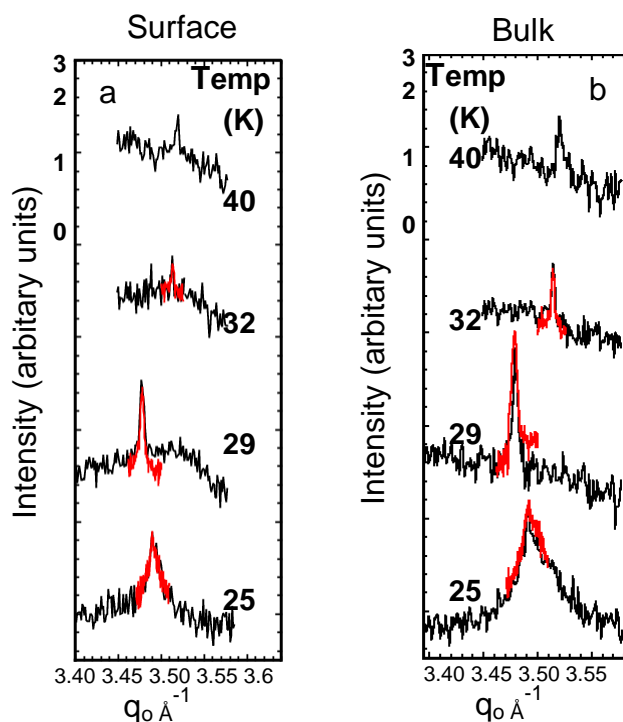


Figure 6-7 Preliminary measurements on NbSe₂ on BW2. A difference in the line shape is observed between the two geometries. The surface sensitive measurements taken at $\alpha_i = 0.2^\circ$ are shown in (a) and the bulk sensitive data ($\alpha_i = 0.45^\circ$) in (b). At low temperature the bulk peaks is broader than the surface peaks. Note at 32 K and higher temperatures a stray bulk reflection was measured instead of the $5/300$ satellite reflection.

This data series shown above, in Figure 6-7, exhibits a different behaviour in the case of the bulk and the surface. The line shape for the bulk is broader than that for the surface. This figure also illustrates one common danger in measuring temperature dependant effects. As the intensity of the satellite reflection dies off with temperature the sample was unfortunately aligned onto a nearby bulk reflection. This problem was avoided in later experiments by only aligning the satellite peak while there was a reasonable amount of intensity and by avoiding movement in θ of larger than $\Delta\theta = 0.01^\circ$ during alignment. This method is effective as the peak width is broad in comparison with position movements. This experiment raised many interesting questions such as why does the surface appear to be more ordered than the bulk. It was clear there was a need for an additional experiment.

6.5 Ultra high vacuum preparation

Although no sign of an oxide is observed in the region of the Bragg peaks and other experiments have shown the surface of NbSe₂ to be unaffected by air in STM measurements⁷⁹ we wanted to confirm this experimentally on our sample. In order to

be certain that there was no surface contamination, an in-vacuum experiment was attempted using the transportable baby chamber of R. Johnson⁸⁰. The samples were cleaved in-vacuum in the Flipper chamber and then transferred under high vacuum to the baby chamber where the sample was mounted on the end of the cold finger of a liquid helium Displex cryostat. The baby chamber was then transported to BW2 under vacuum using a portable power supply and mounted on the diffractometer. On the in-vacuum cleaved sample it was possible to observe the satellite peak but due to the degree of debris on the sample surface it was impossible to maintain a depth sensitivity and we did not obtain a surface sensitivity in these measurements. Using in-vacuum cleaving techniques we were not successful in getting a cleave of sufficient quality for grazing incidence diffraction. We could not achieve a removal of an entire surface layer resulting in the flat surface required in the time scale of a beamtime. This result is not surprising when one considers that in order to obtain a “good” cleave in air the sample is often cleaved as many as twenty times before an optically flat surface is achieved. It would be very interesting to repeat this experiment if there was an alternative cleaving method or if one had a large number of samples. In this case one would require an in-vacuum camera in order to inspect the sample before transferring to the diffractometer.

In the following experiments the sample was cleaved in air, then directly mounted on the cryostat and pumped down to a pressure of 10^{-7} mbar.

6.6 Data from BW2: Further GID measurements

Having seen that the surface/bulk behaviour was different for NbSe₂ in section 6.4 a more thorough experiment was planned. As the signal measured previously was so low the two experiments discussed here were carried out at 9.5 keV to maximise the intensity available at the BW2 wiggler beamline. The sample was cleaved in air using the Scotch tape method outlined in chapter 5 and then mounted, under a Be dome, on the cold finger of the Kiel closed-cycle Helium cryostat (minimum temperature 25 K). The cryostat was mounted on the BW2 diffractometer. The incident beam was defined by slits of 0.5 x 1 mm² (horizontal x vertical) and for the scattered beam 1 mm vertical slits with a position sensitive detector collecting over a horizontal range of 50 mm integrating over α_f (the exit angle from the sample). The integrated signal of the position sensitive detector signal was taken as the peak intensity. Even though we were illuminating a sizeable area of the sample (about 0.5 mm²), the characteristic transmission curve from a single terrace was observed at the position sensitive detector throughout this experiment. The illuminated sample area was 2 mm².

The sample surface quality was first confirmed with a ‘reflectivity’ scan taken in the GID geometry with detector slits 1 x 1 mm² shown in Figure 6-8 (our set-up was optimised for GID and not for reflectivity). In the temperature range from 25 to 45 K

GID Bragg scans and rocking curve scans were then performed at the CDW satellite reflection $q(5/300) = 3.513 \text{ \AA}^{-1}$ and at a reference reflection $q(200) = 4.215 \text{ \AA}^{-1}$.

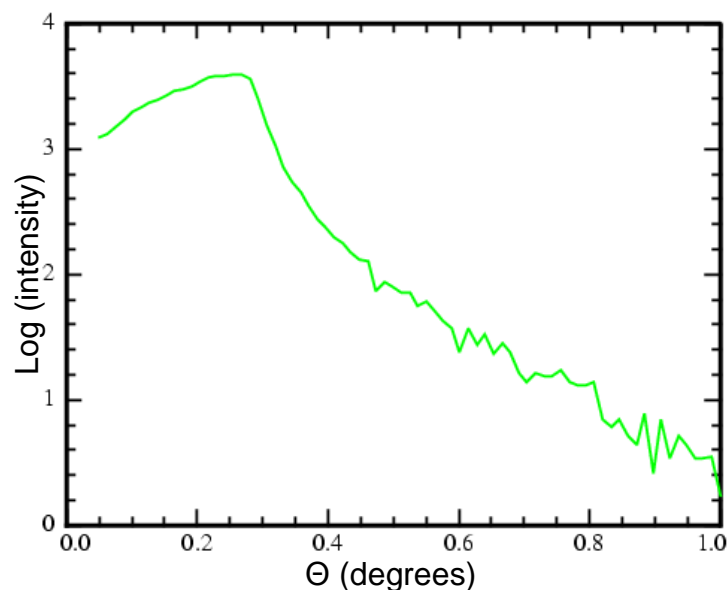


Figure 6-8 This ‘reflectivity’ of cleaved NbSe₂ sample was collected on BW2, HASYLAB with the sample aligned in the grazing incidence geometry. Though this set-up is not optimised for reflectivity the critical angle of total external reflection α_c can be determined ($\alpha_c = 0.29^\circ$).

The CDW and a reference reflection were measured at a surface sensitive incidence angle, the first series with $\alpha_i = 0.14^\circ$ (penetration depth $\sim 24 \text{ \AA}$), and then at an increased incidence angle $\alpha_i = 0.4^\circ$ (penetration depth $\sim 1,500 \text{ \AA}$), to increase bulk sensitivity. The second series was taken with $\alpha_i = 0.17^\circ$ (penetration depth $\sim 26 \text{ \AA}$) to gain intensity in the surface component. Temperature steps 1 K or 2 K were made below the phase transition. Steps of 0.1 K were required in the region of the transition and larger step sizes of 5 K or 10 K were taken above the critical temperature. Due to the low intensity of the satellite reflection, the signal-to-noise ratio was just 3.5 to 1 even at 25 K. Therefore counting times were very long especially close to the transition temperature where a single $5/300$ Bragg scan required 2.5 hours. Over the temperature range we monitored the order parameter (proportional to the square root of the satellite peak intensity) and the satellite diffuse scattering intensity. The temperature dependent evolution of the satellite peak at the surface and in the bulk for two separate temperature scans with different angles of incidence is shown in Figure 6-9 and Figure 6-10.

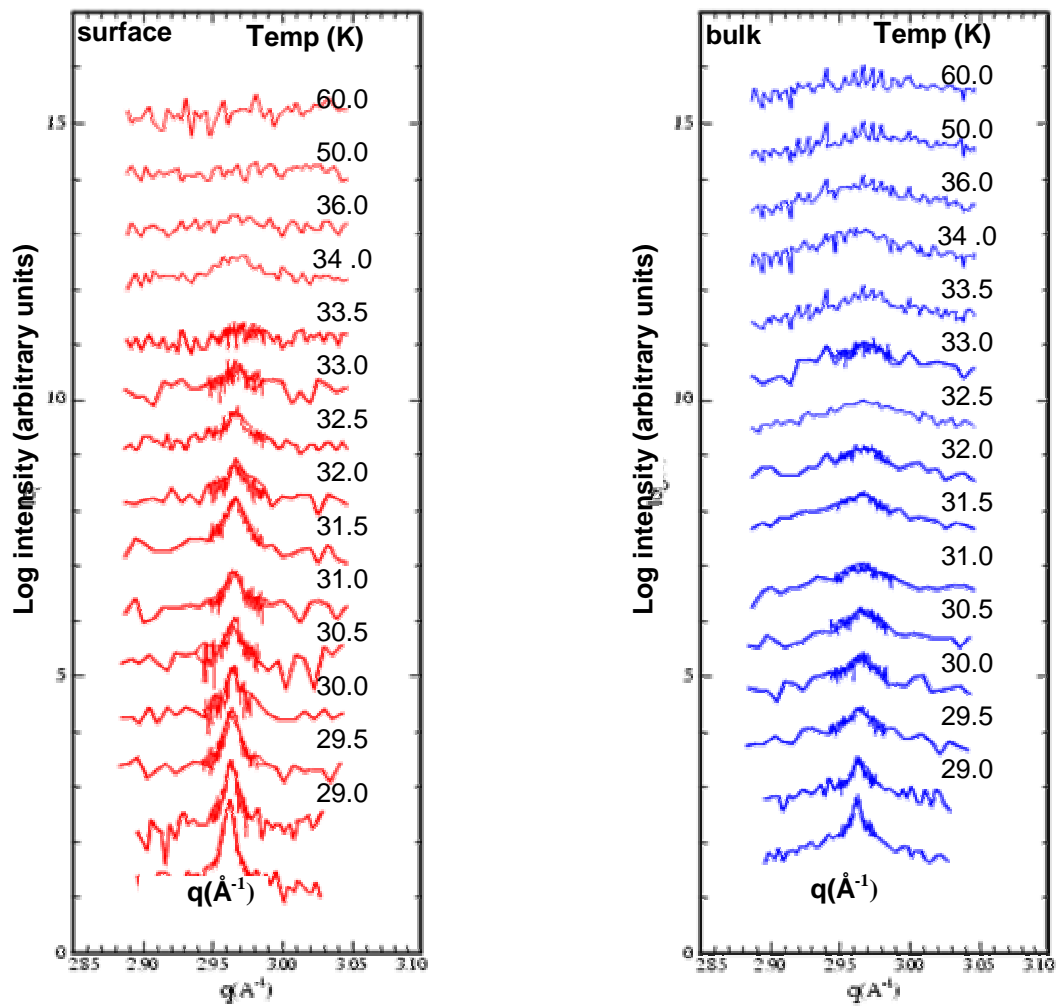


Figure 6-9 The two plots show the temperature dependent behaviour of the $5/300$ satellite peak Bragg scans in the surface sensitive geometry $\alpha_i = 0.14^\circ$ (left) and in the bulk sensitive geometry $\alpha_i = 0.4^\circ$ (right) for temperature series 1. The bulk CDW component vanishes at 33.4 K. The Bragg surface component is still observed at higher temperature. The data were collected at BW2, HASYLAB.

The difference in the peak shapes is striking. We observe a significant change in peak shape between the surface and the bulk data. There is very little diffuse scattering under the satellite Bragg component in the surface data and a broad diffuse background is observed in the bulk. This can be clearly seen in Figure 6-10. The diffuse scattering in the bulk remains visible up to 60 K (

Figure 6-9). In the surface the diffuse component is very low. This contrast between the surface and bulk data is very surprising and is evidence of a greater degree of order on the surface than in the bulk. In Figure 6-11, the bulk and surface scan at 28 K

are shown: there is a stronger, more intense diffuse component present in the bulk than in the surface scan.

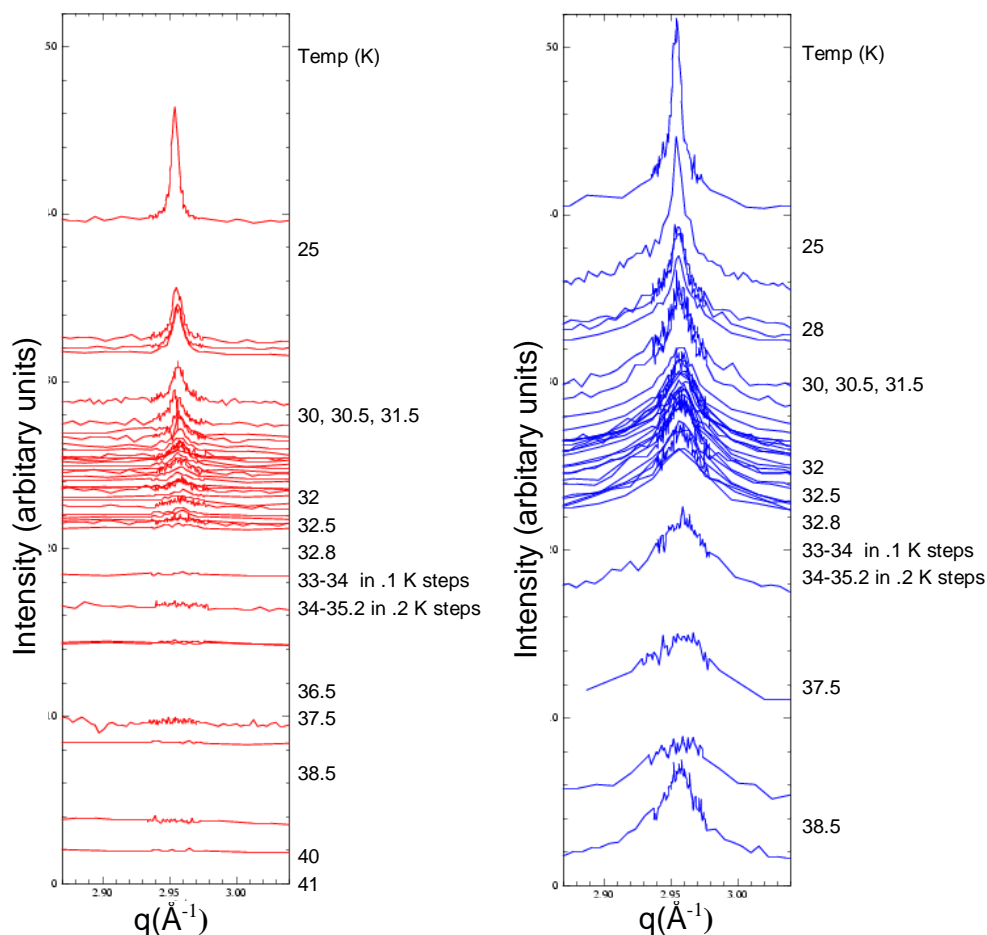


Figure 6-10: Bragg scans measured at BW2 are shown for incidence angles 0.17° and 0.4° at the $5/300$ satellite reflection for the temperature range 25 K to 45 K for temperature series 2. The contrast between the peak line shapes is stark with a broad diffuse component present in bulk even at temperatures above T_c . In the bulk the phase transition occurs at $T_{cb} = 33.5$ K and at the surface at $T_{cs} = 34.9$ K. The temperature difference between the bulk transition and that at the surface is $\Delta T = (1.4 \pm 0.4)$ K.

There could be a number of reasons for this. One could be that in the bulk sensitive geometry thermal diffuse scattering is observed. It could also be that the surface has inherently better short range order and so the component is not broad as in the case of the bulk. We can also consider it as evidence that the transition is more continuous at the surface than in the bulk as the diffuse intensity is more pronounced in the region very close to T_{cb} .

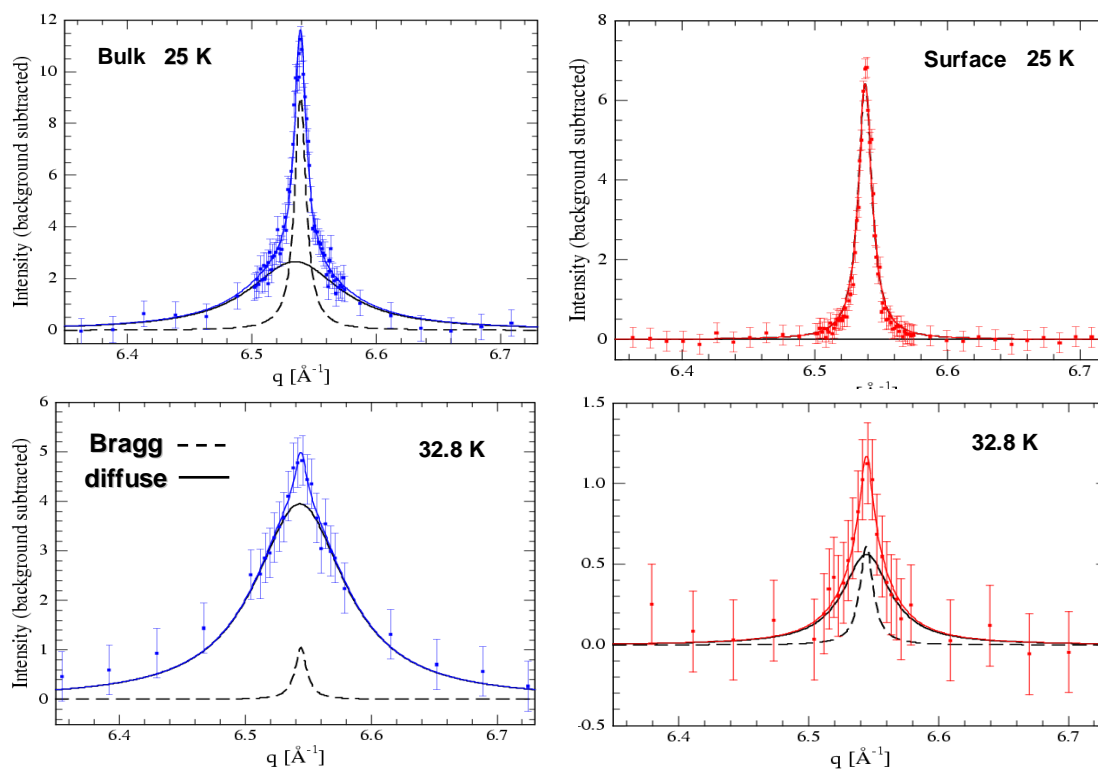


Figure 6-11 Bragg scans through the $5/300$ satellite at 25 K and 32.8 K show a far greater diffuse component in the bulk (left) than in the surface (right) for temperature series 1. The figure shows the Bragg and diffuse component for bulk and surface. Data measured at BW2, HASYLAB.

The data were analysed using a least-squared fit algorithm. At each temperature the Bragg and diffuse component of the satellite peaks were fitted (see Figure 6-11) and also the 200 reference Bragg reflection. The 200 intensities were used to normalise the satellite intensities and the 200 position was used as a reference position for the satellite position. All the peaks were fitted with a Lorentzian line shape. For the satellite peak the integrated intensities and positions of both Bragg and diffuse components were varied, as was the FWHM of the diffuse component. The FWHM of the Bragg component was fixed to a constant throughout the fitting in order to reduce the number of free parameters. This value chosen was the mean value of the FWHM over the temperature series which was the same within the calculated error [surface FWHM = $(0.1 \pm .03)^\circ$, bulk FWHM = $(0.09 \pm 0.03)^\circ$].

The temperature dependence of the intensities of the Bragg component for temperature series 1 is shown below in Figure 6-12. The bulk intensity disappears before the surface intensity. From a linear extrapolation of the data points close to T_c the transmission temperature was estimated for both the surface and the bulk giving $T_{cb} = (33.4 \pm 0.5)$ K, $T_{cs} = (35 \pm 0.5)$ K. This is a very interesting result as $\Delta T = (1.6 \pm 0.5)$ K with the surface critical temperature above that of the bulk.

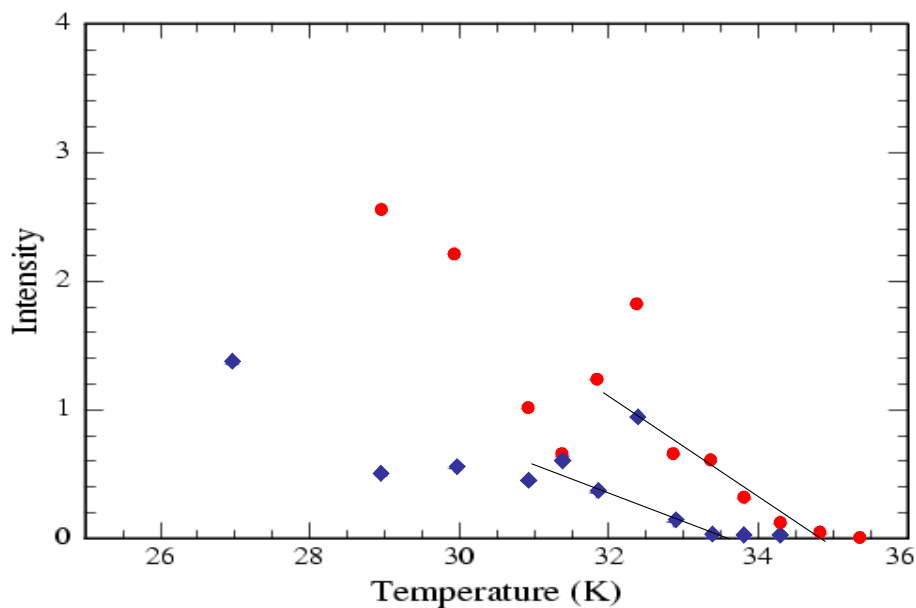


Figure 6-12 By plotting the intensity of the $^{5/3}00$ satellite peak for temperature series 1 (as determined when the data is fitted with two Lorentzian components) against temperature, the phase transition critical temperature for the bulk and surface geometry, respectively may be estimated to be: $T_{cb} = (33.4 \pm 0.5)$ K, $T_{cs} = (35 \pm 0.5)$ K, $\Delta T = (1.6 \pm 0.5)$ K. Data collected at BW2, HASYLAB. The intensity error bars are approximately ± 0.5 intensity units for all data points collected (blue diamonds bulk, red dots surface).

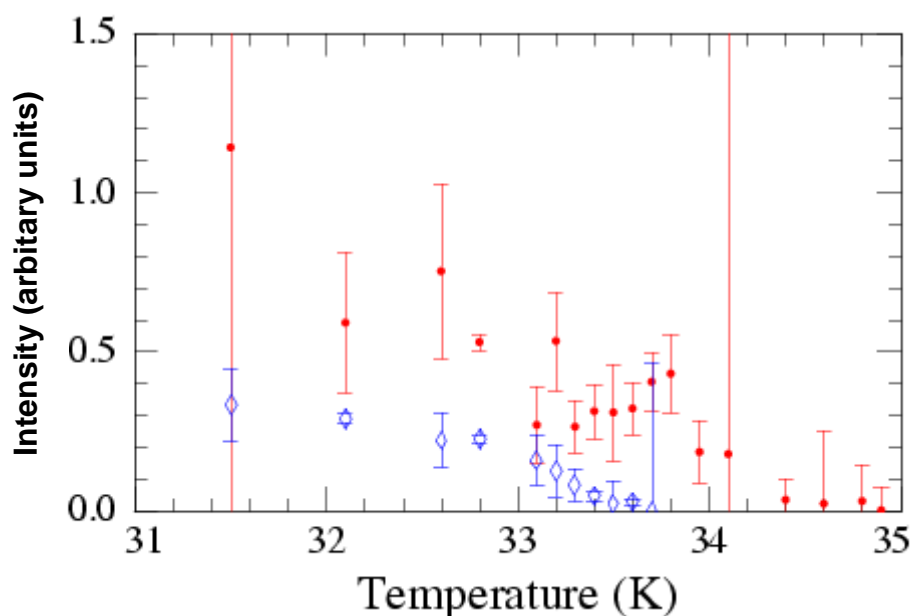


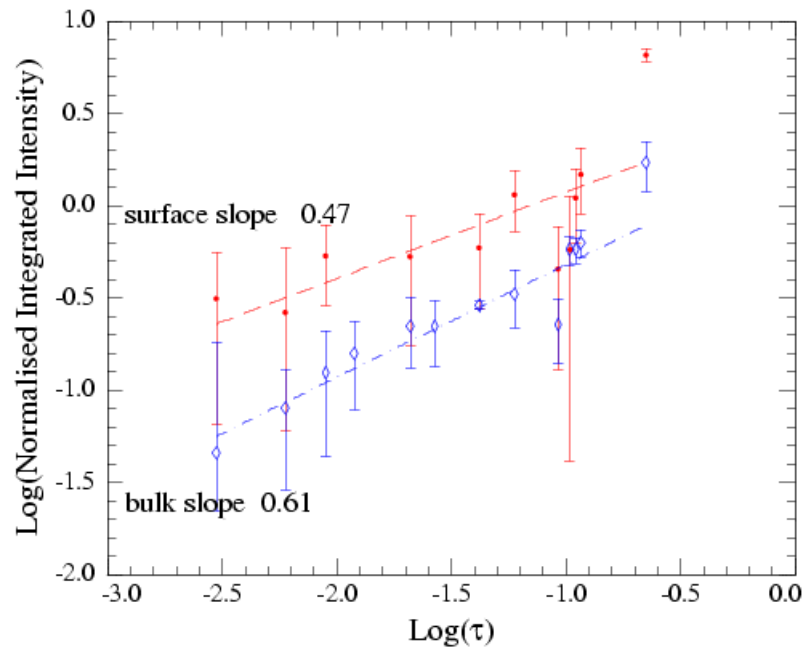
Figure 6-13 Temperature dependence of the integrated intensity of the $^{5/3}00$ satellite reflection measured on BW2 (for temperature series 2), normalised to the integrated intensity of the 200 Bragg reflection. The bulk and surface transition temperatures, respectively, are $T_{cb} = 33.5$ K and $T_{cs} = 34.9$ K (blue diamonds bulk, red dots surface).

Figure 6-13 shows the temperature dependence of the $^{5/3}00$ satellite reflection normalised intensity for the surface and bulk (temperature series 2). For both cases the

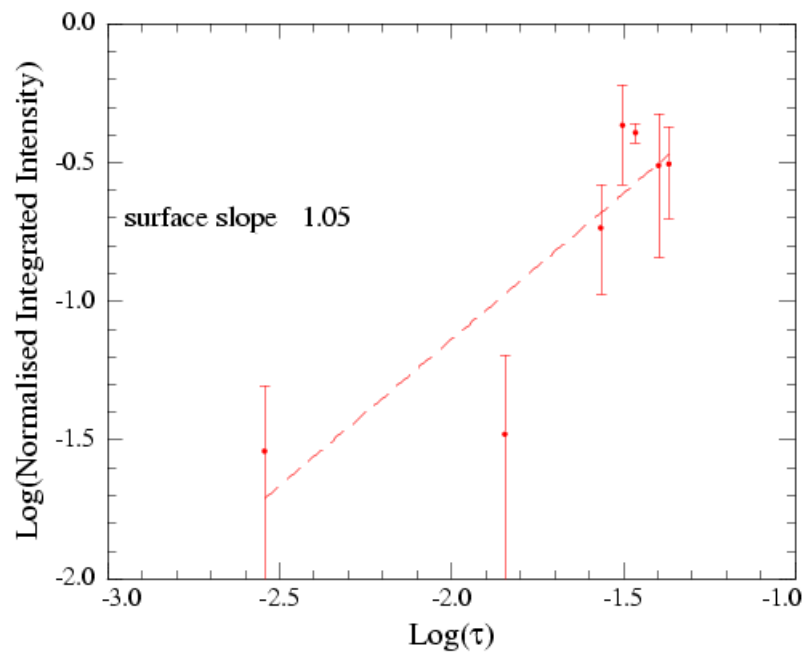
intensities, which are proportional to the square of the amplitude of the modulation, appear to go continuously to zero as expected at a second order phase transition and previously observed by others^{1,7}. Though these experiments found no evidence of a discontinuity it can not be completely ruled out due to limited resolution and intensity. An increased surface transition temperature with respect to the bulk is clearly observed. The transition temperature for the surface and for the bulk was obtained by plotting the integrated intensities on a linear intensity scale. The bulk transition temperature T_{cb} was found to be (33.5 ± 0.2) K and the surface transition temperature $T_{cs} = (34.9 \pm 0.4)$ K. This is an extremely interesting result. $T_{cs} = T_{cb} + (1.4 \pm 0.6)$ K is a strong indication that this is not an ordinary transition as is generally expected for second order transitions (discussed in chapter 3 section 2). One must consider the possibility that we have observed a ‘surface transition’ i.e. a higher transition temperature at the surface than in the bulk in NbSe₂, described by a 2D behaviour at the surface. This situation is predicted by phase transition theory for surfaces^{9,10,11} as discussed in chapter 3 but to the best of our knowledge has not been confirmed experimentally for a second order system. There is some evidence of a slope change for the surface in the vicinity of T_{cb} but the magnitude is comparable to our errors. This could be due to a cross-over effect close to the critical temperature as predicted in the theory^{44,9,46} and observed experimentally¹⁵. The cross-over effect occurs because of the change in the surface coupling constant as discussed in chapter 3 (Equation 3-34). It is not possible to confirm the effect with these data due to the fact that a small slope change is expected and the experimental error is large close to T_c .

By plotting the intensity against the reduced temperature τ on a double logarithmic scale, where τ_b is the bulk reduced temperature calculated using the bulk transition temperature, the exponents for the bulk transition and the extraordinary transition (at the surface) are obtained (Figure 6-14 a). We see that both the surface and bulk data follow a power law. From these slopes we can obtain the values for the order parameter exponents $\beta_{l,e}$ and β_b for the surface and bulk, respectively. In the case of the bulk we obtain an exponent β_b of 0.31 ± 0.1 . The value we obtain for the surface is $\beta_{l,e} = 0.24 \pm 0.2$.

The exponent for the ‘surface transition’ can also be determined by plotting the data from the temperature range $T_{cb} < T < T_{cs}$. In this case τ_s is the surface reduced temperature determined from the surface transition temperature (Figure 6-14 b). An exponent $\beta_{l,s}$ of 0.5 ± 0.3 is obtained for the ‘surface transition’. Due to the large errors these exponents will not be interpreted further at this point.



(a)



(b)

Figure 6-14 Double logarithmic presentation of the integrated Bragg intensity of the $5/300$ satellite reflections collected in temperature series 2, shown in Figure 6-10, with respect to the reduced temperature. The straight lines indicate the power law dependence for the bulk (open diamonds) and surface (closed circles). β_b is 0.31 ± 0.1 and $\beta_{I,e}$ is 0.24 ± 0.2 . (b) The surface intensity is plotted as a function of the surface reduced temperature τ_s giving a $\beta_{I,s}$ of 0.5 ± 0.3 (blue diamonds bulk, red dots surface).

Figure 6-15 shows the temperature dependence of the $^{5/3}00$ satellite diffuse component intensity. It is noteworthy that here we are at the experimental limit and though there appears to be an increase in intensity in the region of the transition the errors are large enough to detract from further analysis. There is very little diffuse scattering under the satellite Bragg component in the surface data and a broad diffuse background is observed in the bulk. From Equation 4-23 the correlation length of the charge density wave is proportional to the inverse of the half width half maximum ($0.5 \sigma_{fwhm}$) of the satellite reflection Bragg peak. From our data sets the correlation length ζ of the charge density wave long-range and short-range component well below T_c at 28 K was calculated for both the bulk and the surface condition. The calculations are shown in table in Table 6-1. The correlation length of the charge density wave oscillations is much shorter than that of the crystal structure as the FWHM of the charge density wave component is $\sim 800 \text{ \AA}$. The average value for the correlation length as calculated from the $^{5/3}00$ diffuse scattering component in the surface is twice that in the bulk. This is a very interesting result and is not usual, therefore we consider it to be related to the temperature shift of the critical point at the surface. This could be an indication that the surface is far more ordered than the bulk. Another possible explanation is that the transition is more continuous at the surface than in the bulk. In the case of an ideal second order phase transition⁸¹ the diffuse component is only observed in the temperature range very close to the T_c .

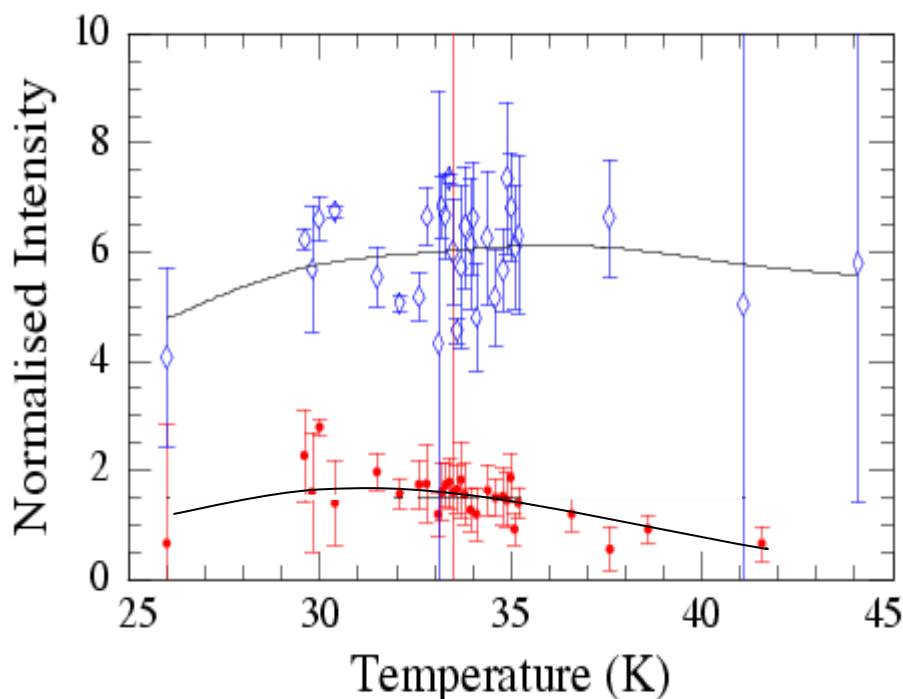


Figure 6-15 Intensity of the diffuse scattering from the $^{5/3}00$ satellite reflection (closed circles – surface, open diamonds - bulk) normalised to the 200 reflection integrated intensity. The lines are a guide to the eye (blue diamonds bulk, red dots surface).

Correlation length		ξ (Å)
5/300 Bragg peak	Moncton @ 10 K	114
5/300 Bragg component @ 28 K	Surface	785 ± 200
	Bulk	825 ± 200
5/300 diffuse component	Surface	285 ± 85
	Bulk	104 ± 30

Table 6-1 The correlation length ξ of the charge density wave oscillation may be calculated from $5/300$ satellite reflection, values found in our experiments are compared to the value from Moncton².

We have observed the same unusual temperature behaviour in both these experiments indicating that the surface charge density wave transition occurs at a higher temperature on the surface than in the bulk. There are large errors in the region close to the transition temperature, which make an accurate description of the diffuse scattering behaviour difficult. Therefore, it was necessary to carry out a further experiment at a third generation synchrotron where a high brilliance is available, i.e. increased flux and lower divergence. This brilliance allows scanning over a wider temperature range and in particular with smaller temperature steps in the region of the transition where the intensity is lowest. However, we can say that the central finding of the BW2 measurement is that for 2H-NbSe₂ there is a temperature difference between the CDW transition temperature in the sample bulk and at the surface. T_{cs} is greater than T_{cb} where $\Delta T = (1.4 \pm 0.6)$ K.

6.7 ID1

A final decisive experiment was carried out on ID1 at the ESRF. An energy of 10.37 keV was chosen in order to profit from the fact that the beamline optics were optimised for use at this energy. The sample was cleaved in air and then mounted, under a Be dome, on the cold finger of the Leybold cryostat (minimum temperature

18.5 K). The cryostat was mounted on the ID1 diffractometer. The incident beam was defined by slits of $0.2 \times 0.2 \text{ mm}^2$ (horizontal \times vertical) and for the scattered beam 0.5 mm horizontal slits with a position sensitive detector collecting over a vertical range of 20 mm . The resulting illuminated spot size was approximately 1.5 mm^2 for the range of incidence angles used in this experiment. The small beam size was chosen to ensure that the characteristic transmission curve from a single terrace was observed at the position sensitive detector throughout this experiment. In addition the focusing monochromator was set to its minimum bend in order to minimise divergence. The position sensitive detector signal integrated over α_f was taken as the intensity.

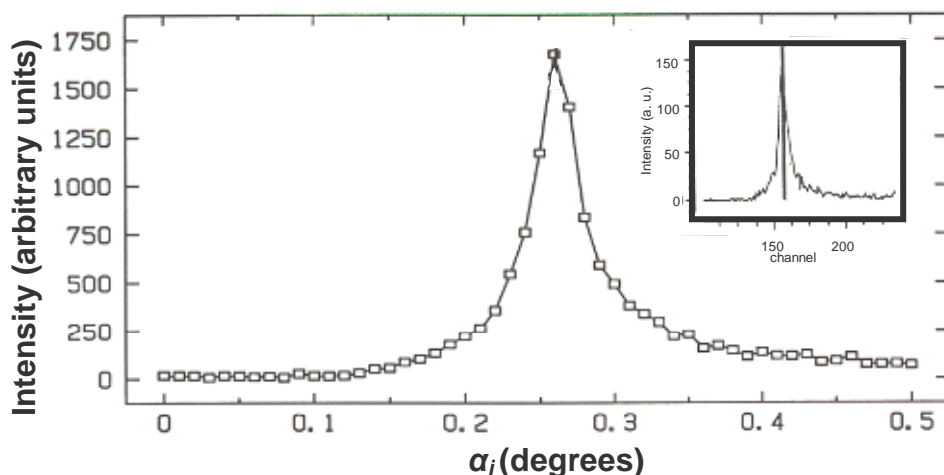


Figure 6-16 Transmission function of NbSe₂ measured on ID1 as a function of α_i . The FWHM is $0.034^\circ \pm 0.001^\circ$. The multi-channel analyser signal (α_f -resolved scattered intensity) taken at α_c is shown as an inset. It displays the typical profile for scattering from a single terrace.

By varying the incidence angle an approximation to the transmission function was measured (Figure 6-16). The critical angle of total external reflection is observed to be at 0.26° which agrees with the calculated value as determined by other authors, see for example Ref. 36. The full width half maximum of the curve is 0.034° . Surface and bulk sensitive measuring geometries were chosen symmetrically about the critical angle. For the surface sensitive measurements an incidence angle of 0.16° was chosen resulting in a penetration depth of approximately 27 \AA . This is a little larger than twice the c lattice constant ($c = 12.547 \text{ \AA}$)¹⁹. The bulk measurements were taken with an incidence angle of 0.36° resulting in a penetration depth of about 1400 \AA .

The temperature dependence of the $5/300$ satellite and the 200 intensity, as reference, were measured in both surface and bulk sensitive geometry. The sample was first cooled to 18 K where the $5/300$ intensity was 300 counts per second at the angle of total external reflection. The 200 intensity was 127,000 counts per second. The raw data are presented in Figure 6-17. Again a different line shape is observed for surface and bulk geometries. A broader and more intense diffuse component is clearly seen in the bulk data while for the surface it is difficult to distinguish the diffuse scattering

from the background at a first glance. Consequently, interpretation of the short range order at the surface is more difficult than that of the bulk. If the beam size at the sample position was increased above $0.2 \times 0.2 \text{ mm}^2$ contributions from other terraces were observed on the PSD. This meant that in order to maintain sensitivity to a single terrace one had to compromise greatly in the charge density wave satellite reflection intensity.

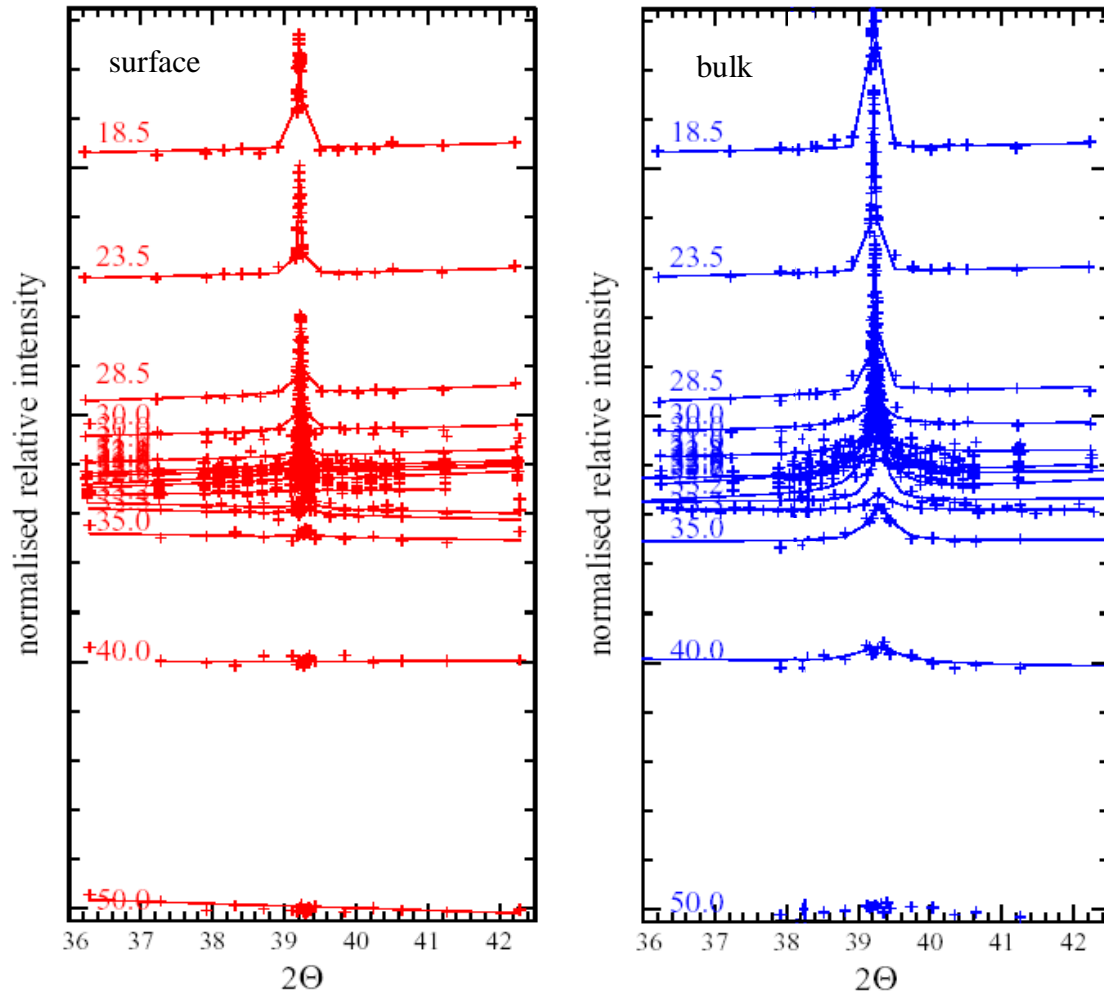


Figure 6-17 The $^{5/3}00$ satellite reflection Bragg scans as collected on ID1 (ESRF) display a noticeable temperature dependence. The data were collected at an incidence angle of 0.36° (bulk geometry) and 0.16° (surface geometry). The experimental data are shown as data points and the result obtained from the fitting procedure as continuous lines (blue bulk, red surface).

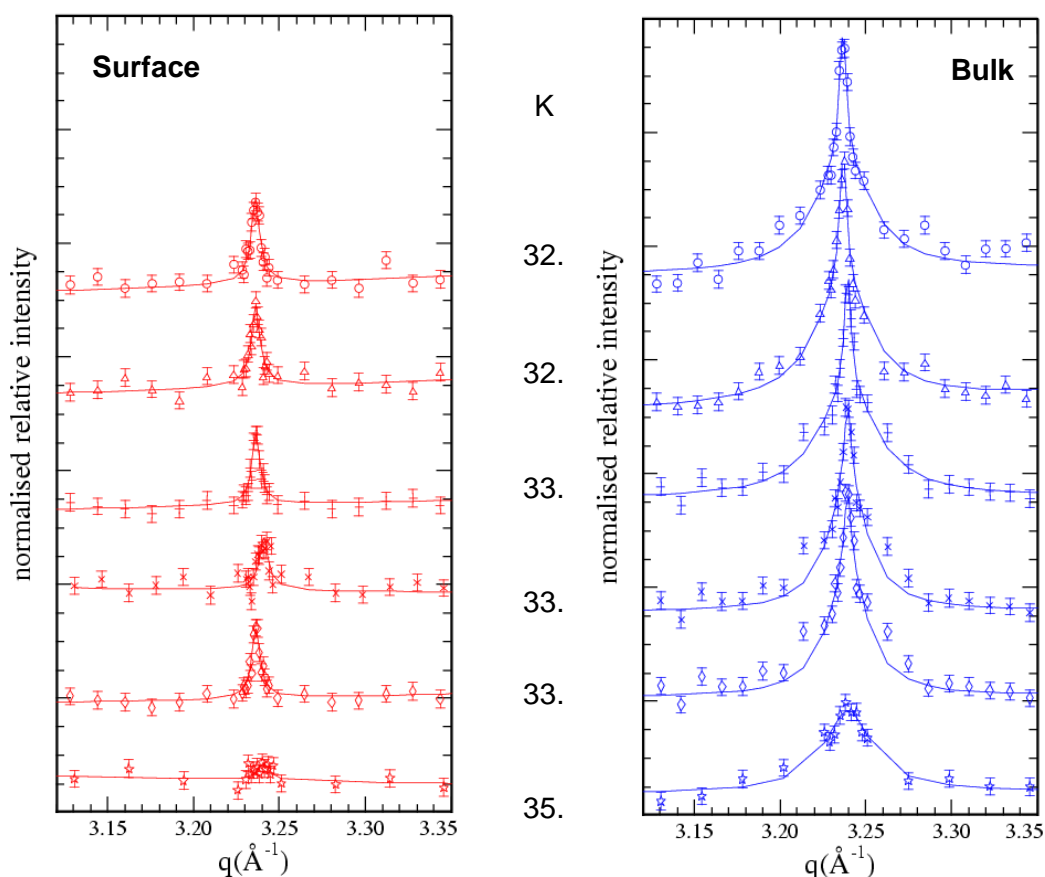


Figure 6-18 The $^{5/300}$ satellite Bragg scans in the range closer to T_c . The data were collected at an incidence angle of 0.36° (bulk geometry) and 0.16° (surface geometry). The experimental data are shown as symbols and the result obtained from the fitting procedure as continuous lines. Data collected at ID1, ESRF (red surface, blue bulk).

Fit

In order to analyse the data they were fitted using the same least squares fitting routine as described in section 6.6. The results obtained when each data set was fitted at each temperature independently are presented in Figure 6-17 and Figure 6-18. This method has the advantage that no prior knowledge of the system is required.

Initially data collected at each temperature were analysed independently. The $^{5/300}$ satellite reflection was fitted with two components, a Bragg component and a diffuse component. The 200 reference Bragg reflection was fitted with a single component using the same procedure. The intensities and positions obtained were used to normalise the satellite reflection data in order to reduce the effect of intensity or positions changes in the primary beam. As before a Lorentzian line shape was found to be appropriate for all peaks fitted. The following fitting procedure was used: For the satellite peak the integrated intensities were varied. The position of both Bragg-

like and diffuse components were set to the same value and then varied together. The FWHM of the diffuse component was varied in addition. The mean value of the FWHM of the Bragg component in the temperature range excluding the 18.5 K data were fixed to a constant throughout the fitting in order to reduce the number of free parameters (surface and bulk FWHM = $0.05^\circ \pm 0.01^\circ$). Fixing the width of the Bragg-like component is appropriate as no large changes in the FWHM close to T_c are expected. This reduced the number of parameters in the fit and helps to ensure that intensity variations close to T_c are assigned to the correct component. For a continuous phase transition where the diffuse component is gaining intensity while simultaneously the Bragg component is losing intensity such an assignment is nontrivial. Further away from T_c the diffuse component is broad and therefore even to the naked eye it is clear which intensity belongs to which component. However as T_c is approached the FWHM of the diffuse component is minimised making it more difficult to separate the diffuse component from the Bragg component.

Determining the critical temperature

The uncertainty in the T_c determination comes principally from the low intensity in the satellite Bragg reflection. There may be an offset in the temperature due to the fact that the diode though close to the sample is not situated on the sample surface (impossible in this geometry). In order to reduce possible errors in the temperature data were collected first in the surface geometry and then in the bulk geometry at each temperature step. This complicates the alignment but reduces possible temperature errors immensely. After each temperature increase the system was allowed to reach thermal equilibrium. For temperature steps of greater than 1 K an hour was required. For steps less than 0.5 K, half an hour was allowed. The thermal stabilisation of the sample was monitored via the satellite peak intensity which varies with temperature. Final alignment at each temperature was carried out only after thermal equilibrium was reached. The main source of error in temperature therefore comes from drift and oscillation due to the temperature control device. The oscillation was ± 0.01 K with the Lakeshore temperature controller. There was a drift of just 0.03 K observed over the three hours required to make a set of scans at a single temperature. This drift was accurately determined as the temperature was recorded at the same time each data point was taken. Therefore, the temperature error possible between an equivalent surface and bulk measurement for this measurement is 0.04 K. One other effect that could cause a small temperature gradient between the sample surface and bulk is warming due to the X-ray beam impinging on the sample. This of course would reduce the temperature gap between the surface and bulk. In any case low temperature studies show that surface warming effects due to thermal contribution of a third

generation synchrotron source X-ray beam are only significant at temperatures less than 1 K⁸².

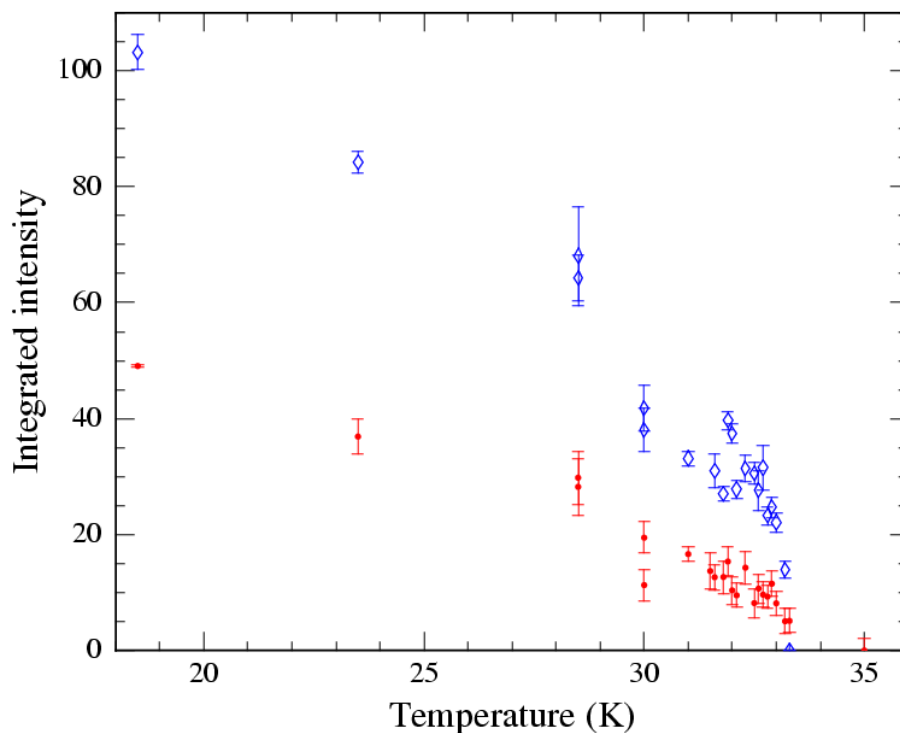


Figure 6-19 Temperature dependence of the integrated intensity of the $5/300$ satellite reflection measured on ID1, normalised to the integrated intensity of the 200 Bragg reflection. Both the surface and bulk intensity go continuously to zero with increasing temperature (blue diamonds bulk, red dots surface).

The temperature dependence of the $5/300$ satellite reflection integrated intensity ($I_{int} \sim I_{peak}$ since the FWHM is fixed), normalised to background, is shown in Figure 6-19. The result is similar to that obtained on the beamline BW2 even with better intensity and lower background. In agreement with previous measurements and with the work of other groups, the transition appears to be continuous^{1,7} for both the bulk and surface geometry. It is, however, impossible to rule out a small first order component: it would be very difficult to see a discontinuity close to T_c experimentally due to the low intensity in the satellite reflection. When heating the bulk satellite intensity goes to zero at $T_{cb} = (33.3 \pm 0.1)$ K, while at the surface the Bragg component of the satellite is present until $T_{cs} = (34.9 \pm 0.3)$ K. Unfortunately, due to a power cut at the synchrotron, a day of beamtime was lost at the end of the run and it was not possible to continue collecting data in small temperature increments in the temperature range 33.4 K to 34.9 K. In order to determine T_{cs} , the T -axis intercept of the slope taken from data points greater than 31 K is used. The power cut occurred after the 30 K series was completed. To conclude the measurement the sample was cooled again to 28 K, reference measurements were taken at 28 K and 30 K and then the series was continued. Therefore, the error in determining the T_{cs} temperature is

larger than that of the T_{cb} determination. We observe the surface $T_c = (34.9 \pm 0.3)$ K and hence $\Delta T = (1.6 \pm 0.4)$ K above T_{cb} .

The magnitude of the 1.6 K temperature increase for the surface transition above the bulk transition is certainly significant for this experiment. Other authors have carried out surface sensitive grazing incidence diffraction investigations on a variety of crystalline systems. However, in systems with second order transitions no temperature difference between the surface and the bulk has been observed in a single experiment in the absence of an external field (see discussion, 6.8).

Assuming a continuous transition one would expect the data to follow a power law when intensity is plotted against the reduced temperature on a double logarithmic scale (Figure 6.10). We can obtain the values for the order parameter exponents $2\beta_{l,e}$ and $2\beta_b$ for the surface and bulk, respectively, from these slopes. We obtain $\beta_b = 0.18 \pm 0.02$ and $\beta_{l,e} = 0.20 \pm 0.04$. The bulk exponent lies between the 2-D (0.125) and the 3-D (0.325) Ising values predicted by calculations suggesting that NbSe₂ exhibits quasi 2-D behaviour^{10,11}.

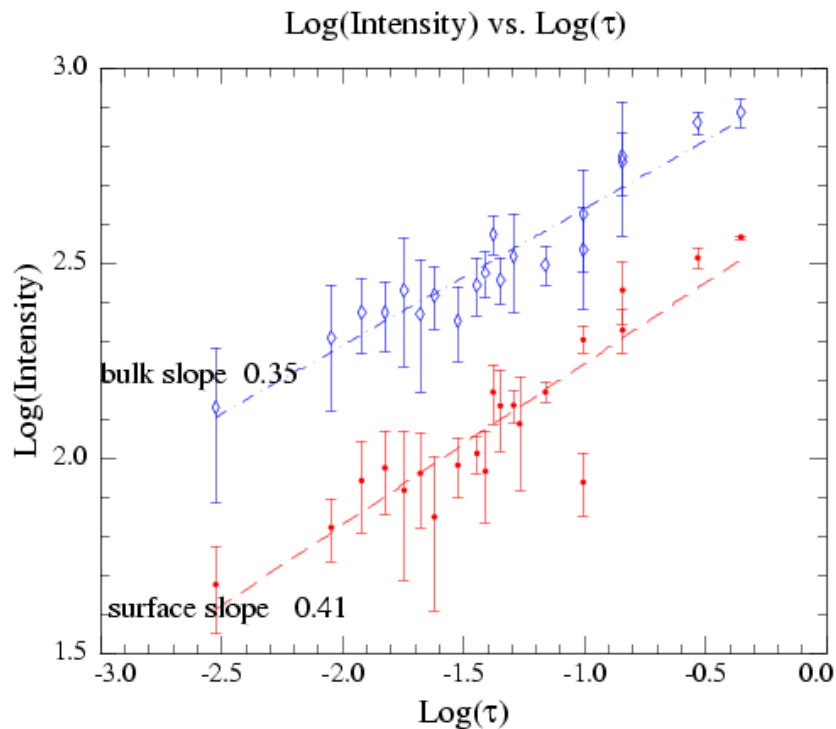


Figure 6-20 Double logarithmic presentation of the integrated Bragg intensity of the $5/300$ satellite reflections, shown in Figure 6-19, plotted versus reduced temperature $\tau = (T - T_{cb})/T_{cb}$. The straight lines indicate the power law dependence for the bulk (open diamonds) and surface (closed circles). The bulk exponent is $\beta_b = 0.18 \pm 0.02$ and for the surface $\beta_{l,e} = 0.20 \pm 0.04$ (blue diamonds bulk, red dots surface).

The consideration hereafter follows that described by Diehl¹⁰ and Landau and Binder¹². The surface exponent β_l describes the ‘extraordinary transition’ in the

temperature range $T < T_{cb}$. As the sample is heated, the degree of ordering m_1^{reg} at the surface does not go to zero at T_{cb} but instead a certain degree of surface order m_{1c} is present at T_{cb} and a degree of order until T_{cs} . Therefore in order to describe the β_1 exponent in the range $T < T_{cb}$ the power law description must be modified. We can determine it using Equation 3-34 as described in Refs. 12,13,44. Following this procedure we observe a linear dependence of $\Delta m = m_1^{reg} - m_{1c}$ on $\tau^{(1-\alpha)}$:

$$\frac{m_1^{reg} - m_{1c}}{\tau} = +a + b^{\pm} \tau^{(1-\alpha)} \quad (3-30)$$

where $\beta_1 = 2 - \alpha$. This is shown in Figure 6-21 below where the constant b , the slope of the linear fit, and the intercept a can be used to determine the exponent β_1 that describes the ‘extraordinary transition’. We observe a linear behaviour of Δm and this is evidence that the system undergoes an extraordinary transition following on from a ‘surface transition’. Since we are so close to the ‘special transition’ condition further analysis does not provide additional information.

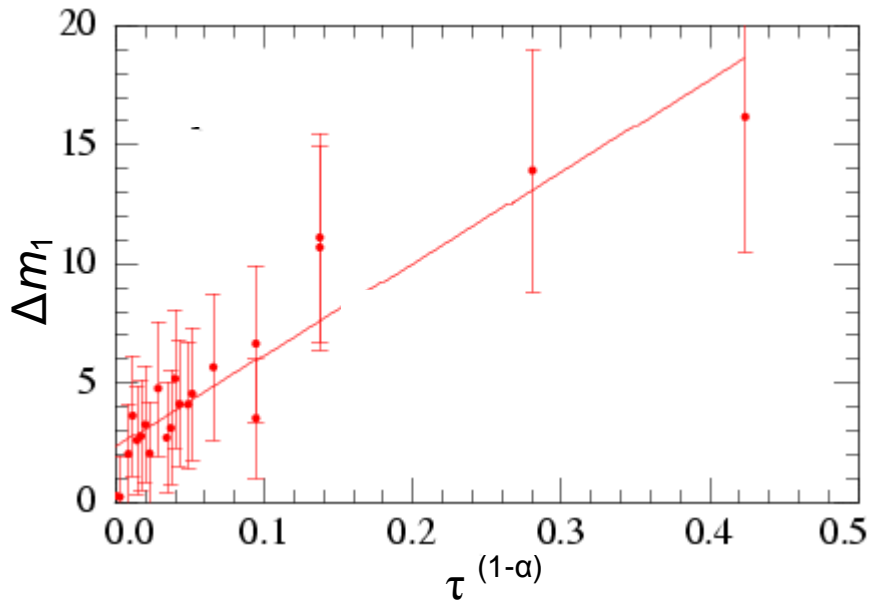


Figure 6-21 It is possible to separate the surface exponent at the ‘extraordinary transition’ by subtracting the contribution of m_c as discussed in the text at T_{cb} according to Refs. 12,13. For an ‘extraordinary transition’ when the data is so described a linear dependence is predicted.

Position of the $5/300$ superlattice reflection

The position of the satellite reflection displays a temperature dependence which is shown in Figure 6-22. In order to reduce the number of variables in the fit, the

positions of the diffuse and Bragg component were coupled in the fit and then allowed to vary together. As both contributions are broad, and little relative change is expected this is a valid restriction.

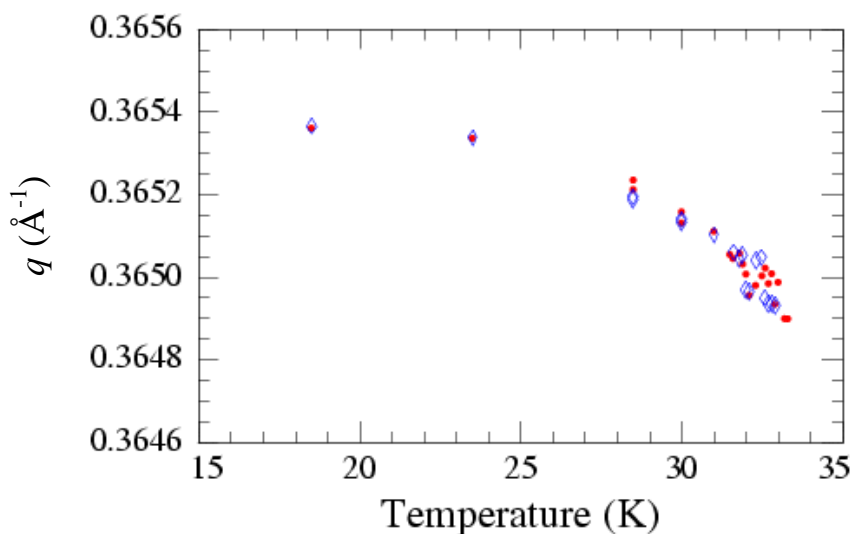


Figure 6-22 The temperature dependence of the $^{5/3}00$ satellite reflection in q for the data collected on the beamline ID1 is plotted. The error in inverse position is 0.00002 \AA^{-1} (blue diamonds bulk, red dots surface).

The position of the CDW satellite structure was found to be incommensurate close to T_c and to move towards a commensurate position on cooling. Yet over the temperature range investigated in these experiment no lock-in transition was observed. This result is consistent with observations of other authors such as Du *et al.*³ and Moncton *et al.*¹. A similar behaviour was observed for both the surface and the bulk charge density wave Bragg positions.

Correlation length

We learn more about the phase transition by looking at the temperature dependence of the FWHM of the $^{5/3}00$ satellite reflection diffuse component. The correlation length of the critical fluctuations is directly related to the width of the diffuse scattering. In Figure 6-23 it is observed that the width of the diffuse scattering decreases as T_{cb} is approached and increases again afterwards. This is the predicted behaviour for a second order phase transition. The data shown is measured in the bulk sensitive geometry. In the surface sensitive geometry it was not possible to determine any temperature dependence effect due to the low intensity.

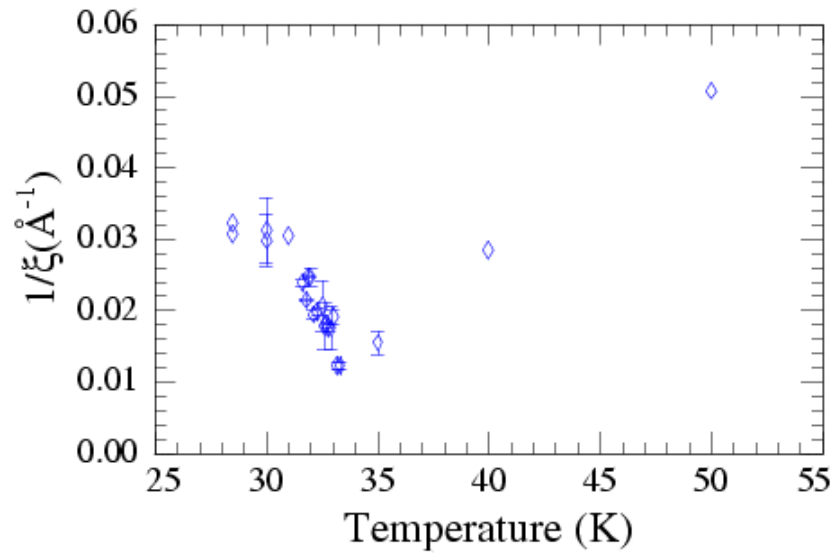


Figure 6-23 The κ or $1/\xi$ values of the diffuse component for the bulk data from 2H-NbSe₂ as obtained from the ID1 data fits are shown in the above figure. A decrease in the width of the diffuse component is observed as T_c is approached. The bulk data exhibit a typical second order like behaviour with a maximum correlation length at T_{cb} (instrumental resolution not removed from the data).

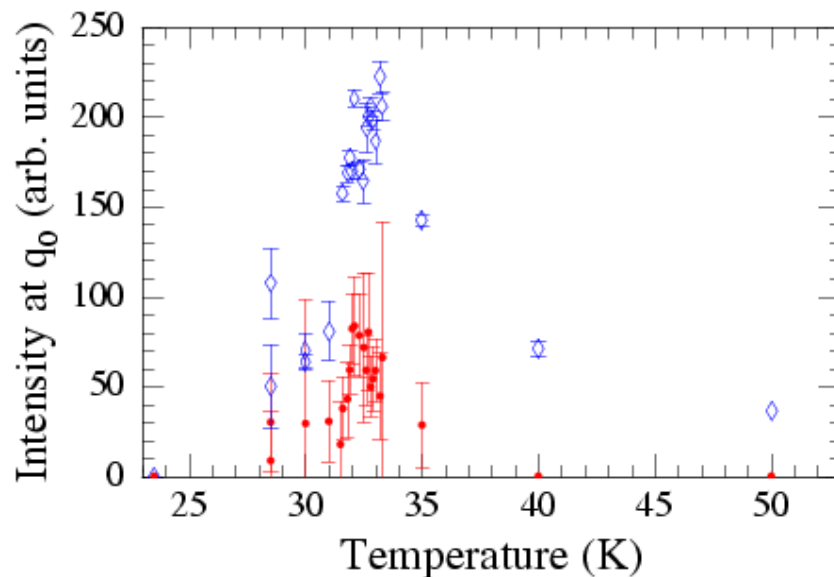


Figure 6-24 The diffuse component of the $5/300$ satellite reflection intensity χ ($q = q_0$) increases rapidly as T_{cb} is approached and decays afterwards in the bulk. This behaviour is consistent with the presence of a second order phase transition. For the surface sensitive data the error bars are of the order of the observed effect (blue diamonds bulk, red dots surface).

Satellite diffuse intensity

The diffuse component of the $^{5/3}00$ satellite reflections intensity $\chi(q = q_0)$ is shown in Figure 6-24 above, where q_0 is the position of maximum intensity. For the bulk on approaching T_{cb} the intensity increases rapidly above 30 K with further heating. The bulk intensity reduces rapidly above the critical temperature but remains visible up to 45 K. The intensity of the surface component is far smaller than that of the bulk as one would expect from the raw data and could not be resolved from background above T_{cs} . An increase in the intensity of the surface data is observed mirroring the bulk behaviour but this could easily be due to the resolution limit of the experiment; the experimental error is large.

It is also important to note that in the fit there is a correlation between the background and the diffuse intensity so one must be cautious in interpreting the fit of the diffuse scattering for the surface data.

Plotting the data shown in Figure 6-24 on a double logarithmic scale, it can be seen that the diffuse intensity also follows a power law behaviour (Figure 6-25).

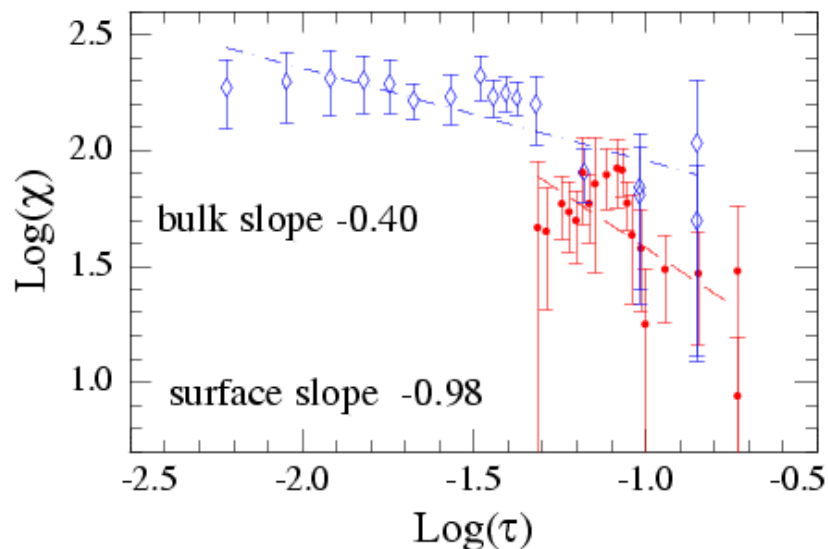


Figure 6-25 Double logarithmic presentation of the diffuse component of the $^{5/3}00$ satellite reflection intensity $\chi(q = q_0)$. It shows a different temperature dependence for the surface and the bulk (blue diamonds bulk, red dots surface).

6.8 Discussion

In the following discussion the significance of the experimental results will be considered. The relevance of the observed (1.6 ± 0.4) K temperature difference between surface and bulk in the CDW phase transition of 2H-NbSe_2 with respect to

other work is explored. The determined critical exponents are then discussed in the framework of the $\frac{1}{2}$ - ∞ Ising model for isotropic systems. In addition we give consideration to how the coupling constants at the surface might change for an anisotropic system.

Modified surface temperature

It is certainly an unusual finding that we observe a higher transition temperature at the surface of 2H-NbSe₂ than in the bulk. In view of this we have repeated the experiment several times to confirm our findings. Though surface temperature effects are predicted by many theoretical considerations of continuous systems, studies on other systems displaying continuous transitions have not reported a temperature difference between the surface and bulk transitions.

The grazing incidence technique provides a depth resolved structural probe that plays a very powerful role in studying the physics of phase transitions at surfaces. There have been many interesting experiments in this area. In an experiment very close to ours in 1990, Zhu *et al.*⁸ performed a GID study of the charge density wave phase transition in K_{0.3}MoO₃ over the depth range 20 – 1000 Å. They found the CDW wave vector at the surface to be the same as that in the bulk. Transition temperature and temperature dependence of the order parameter were found to be depth independent in this material. They postulated that this was due to the weak coupling perpendicular to the (20 $\bar{1}$) surface.

Using surface X-ray scattering, in 1993, Burandt *et al.*¹⁵ observed near surface X-ray critical phenomena from a NH₄Br(1 $\bar{1}$ 0) surface with a penetration depth of 100 Å. A cross-over was observed in the power law behaviour of the order parameter close to T_c . The bulk and surface transition temperatures were identical providing evidence for an ordinary transition.

By using surface sensitive helium atom diffraction, Marynowski *et al.* (1999)⁸³ investigated the antiferromagnetic transition on the NiO(100) surface and claim to have observed an extraordinary transition in a study of the surface order parameter. They were sensitive to a region of 5 – 10 Å from the surface, so only the surface effects could be investigated in this experiment. An order parameter $\beta_I = 0.175$ consistent with predictions for an extraordinary transition was determined. The bulk transition temperature could not be determined directly in this experiment. Therefore, it was determined externally by differential scanning calorimetry. Using this technique it is not possible to measure both surface and bulk behaviour at a single temperature in the same experiment and therefore it is not possible to verify the temperature difference.

Krimmel *et al.*⁸⁴ performed an X-ray scattering study of the continuous B2-A2 order-disorder transition in semi-infinite FeCo(001). They observed that the surface- related

order parameter persists above the bulk critical temperature. This mesoscopically thick surface layer temperature dependence displays a behaviour similar to that of a magnet exposed to an external field. This experiment provided evidence for the presence of a surface field (h_l) which couples to the surface susceptibility. They conclude that the surface layer is not induced by the enhancement of exchange interactions in the surface layer, but rather by surface segregation.

In the case of **first order** phase transitions such temperature effects are more common. Schweika *et al.* (2002)⁸⁵ carried out *in situ* reflectivity measurements of strain-induced wetting in a CuAu(001) single crystal. They observed an ordered layer near the (001) surface well above the bulk transition temperature. They concluded that the incomplete wetting was strain-induced. The order-disorder phase transition at the surface of Cu₃Au(001) by evanescent X-ray scattering was studied by Dosch (1991)⁸⁶. He observed a wetting transition driven by the first order bulk transition. Depth-resolved near-surface relaxation times (minutes) exhibit distinct depth dependence. In 1998, Zhu *et al.*⁸⁷ performed a grazing incidence study of the order-disorder transition in Cu₃Au(111). They observed a first order phase transition in the bulk at 665 K and enhanced surface ordering at a slightly higher temperature. In addition, they found strong diffuse scattering from short range order fluctuations in the bulk, but this effect was much weaker in the surface region. This result is similar to our observations of the short range order in NbSe₂. In 2003, Reichert *et al.*¹⁸ reported a new type of short-range order correlations at the (001) surface of Cu₃Au proposing that this new surface effect was caused by a significant change in strain-induced interactions at the surface. Indeed, one would expect a modified behaviour at the surface to be the result of a structural or electronic behaviour, possibly a combination of both.

As discussed above the surface temperature may be modified by a strain or relaxation. Another factor that could be of influence is the presence of defects at the surface. It has been shown that the critical temperature would be lowered in the presence of defects.^{26,35,78} Therefore, as in our experiments the surface critical temperature is higher than that of the bulk, it is unlikely that the enhancement effect we observe is due to pinning of the CDW by defects.

Considering all the above experiments with respect to our measurements, the temperature difference in T_{cb} and T_{cs} we observe is a significant result. In addition we have seen that the result is reproducible under a variety of experimental conditions. The sample was measured at HASYLAB and ESRF with different equipment. Therefore we can be certain of the temperature difference measured showing the surface T_{cs} at **(1.6 ± 0.4) K** above bulk T_{cb} . This can be understood in the framework of a surface transition arising from an increased coupling constant at the surface (see below).

Critical exponents

In order to explain the behaviour of the surface coupling constants and the underlying physical processes involved in the 2H-NbSe₂ CDW transition, we have determined the critical exponents for this system. We compare the experimentally determined exponents with those found using the Ising model. Why do we use the Ising model to describe a charge density wave system? In a general sense one could better use mean field theory of local density approximation to accurately describe the system. However, in order to obtain a simple model of the system, the Ising model provides a very useful tool. By considering just local interactions even in the case where it is not completely analogous to the spin ½ Ising theory, it is possible to develop a useful model that can be related to our experiment as it allows us to consider the local interactions in a simple manner.

It is always very difficult to determine exponents accurately for a weakly scattering non-perfect system as the intensity in the satellite reflection is very weak and the errors in the region of T_c are consequently large. We have obtained a bulk exponent $\beta_b = 0.18 \pm 0.02$. This exponent is closer to the value expected for a two-dimensional Ising system (0.125) than that for a three-dimensional Ising system (0.325) which is consistent with photoemission experiments where a quasi two-dimensional behaviour was found^{4,5,6}. In keeping with the photoemission experiments there must be 3-D interaction between the layers and this is likely to explain the slightly higher value for the bulk. It is important to note that the bulk value could also be a hint that there is a degree of discontinuity in the charge density phase transition. As Press and Hüller⁸¹ have discussed for a first-order transition, exponents in the range 0.16 – 0.20 are often found in three-dimensional systems which exhibit a small discontinuity close to T_c . However, when we look at the behaviour of the correlation length in Figure 2-1 we see a behaviour consistent with a second order transition, i.e. the inverse correlation length reaches a minimum at T_c . Determining the surface exponents is more difficult as it was not easy to separate the diffuse scattering from the Bragg component in the satellite Bragg reflection. The behaviour of the exponent β_l is extracted here following the theory as described in^{9,10,11}. The exponent for the extraordinary transition was obtained and found to be $\beta_{l,e} = 0.20 \pm 0.04$.

It is very difficult to extract the exponent for the surface transition as one must use data only in the region $T_{cb} < T < T_{cs}$ and here we are extremely intensity limited. However, from the BW2 data a value $\beta_{l,s} = 0.5 \pm 0.3$ was obtained. As the error here is very large this exponent is not very reliable and it does not provide a good agreement with the predicted value of 1/8 from the calculation of Yang⁴⁷. Given that we observe a relaxation of the surface layers from the crystal truncation rod measurements, we propose that the temperature difference we observe results from

the dependency of the perpendicular component of the order parameter on the surface relaxation. The effect of this relaxation on the surface enhancement of the coupling constants is discussed in the following.

Introduction of anisotropy

If we consider that the increase in the critical temperature at the surface is due to the change in the coupling constant in the surface region it is possible to explain this within the framework of a simple Ising model. For the moment, we disregard details of layering and consider the Ising model. As discussed in detail in chapter 2 after Binder, Diehl, Wagner and Dietrich^{9,10,11} consider the Ising model of an infinite 3-D system with interactions changed in the surface plane. In such a system all nearest neighbour interactions (where the restriction is made to neglect second nearest neighbours and beyond) can be described by the coupling constant J . This simple situation is modified in a $\frac{1}{2}$ - ∞ system, with neighbours in the $\frac{1}{2}$ - ∞ limit above the surface missing. The interactions in the surface plane are J_{\parallel} and the coupling between the surface plane and the adjacent plane is J_{\perp} .

In the following a short consideration of the Fermi surface in different dimensions as illustrated in Figure 6-26 is given. If one assumes 2-D Fermi nesting (see chapter 2) within NbSe₂ layers^{4,5,6}, these features would be independent of q_{\perp} and so provide a coupling constant J_{\parallel} in the plane and no coupling in the q_{\perp} or q_z direction. The interactions within the plane are J_{\parallel} and the coupling between planes is J_{\perp} . NbSe₂ has a layered structure, therefore we first consider 2-D perfect Fermi nesting within each layer as a starting point. In this case the Fermi surface would be independent of q_z and so provide a strong coupling constant only in the plane (J_{\parallel}). If there is an interaction J_{\perp} between the layers which is needed for the formation of a 3-D crystal, the Fermi nesting is reduced due to a modification of the parallel coupling constant which results in a weakening of the in-plane coupling constants $-\Delta J$ (see Figure 6-26). In the bulk we obtain $J_{\parallel}' = J_{\parallel} - 2\Delta J$ allowing for 2 neighbouring layers. By relating this to Binder's model and considering a half-infinite system, the coupling constant at the surface is altered so that $J_{\parallel s} = J_{\parallel} - \Delta J$. In the case of TaSe₂ the interaction between the layers is $J_{\perp} \cong \frac{1}{3} J_{\parallel}'$ as measured by Moncton *et al.*². We expect a similar vertical coupling for NbSe₂, hence it is possible to model a mechanism leading to the situation of a surface transition.

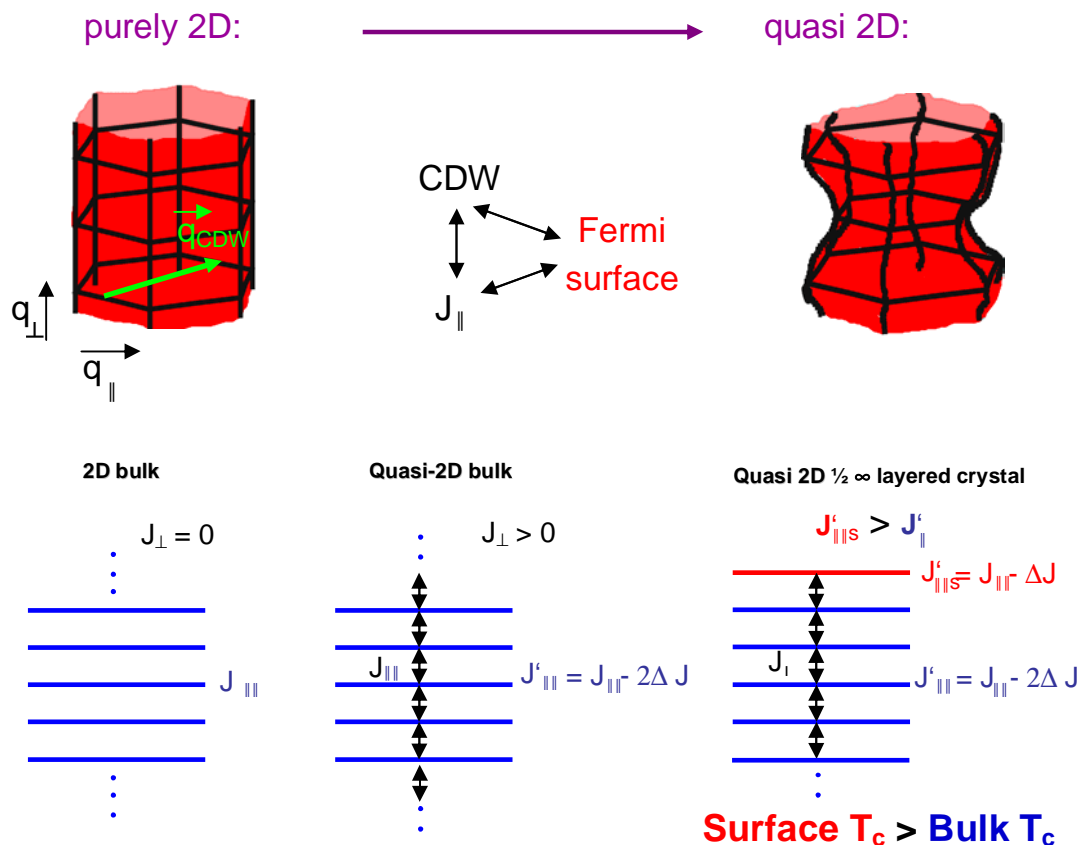


Figure 6-26 A k -space and real space representation of the Fermi surface and nesting of 2D and quasi-2D systems. The sketch above illustrates how the coupling constant is modified close to a surface in a quasi 2D crystal.

6.9 Summary

As can be seen from the above discussion, it is most probable that we have observed a ‘surface transition’ at the surface of 2H-NbSe₂ using GID. We observe that the surface orders at a temperature (1.6 ± 0.4) K higher than in the bulk. Critical exponents have been calculated for the surface and the bulk behaviour. The bulk appears to undergo a two-dimensional-like continuous transition. At the surface a second order phase transition was also observed displaying a different critical behaviour from that observed in the bulk. Considering the anisotropic nature of 2H-NbSe₂ we propose a modified Ising model which would account for the increased coupling constant at the surface. This provides a framework in which the limited interaction between layers may be considered to affect the surface coupling constants. This model is a step towards the understanding this system. The development of a full theoretical model is outside the scope of this thesis.

7 Grazing incidence Inelastic X-ray scattering

7.1 X-ray diffraction

In this chapter the first grazing incidence inelastic X-ray scattering experiment is reported. The experiment was carried out in November 2003. Due to its late nature this chapter is therefore briefer than the other chapters in this thesis.

The technique of inelastic X-ray scattering (IXS) was first shown to work in the late 1980's.^{88,89} It is complementary to the long established inelastic neutron scattering (INS) techniques. Inelastic X-ray scattering has been proven to be particularly useful for cases where samples themselves are too small or the sample environment is unsuitable for neutron work. High pressure research is such an example.⁹⁰ IXS can also overcome kinematic limitations of INS when studying disordered systems at low momentum transfers or with a high speed of sound⁹¹. As we show in this experiment IXS also provides the possibility for depth-resolved measurements.

The study of phonon excitations in condensed matter, which have energies in the meV region, requires a relative energy resolution of at least $\Delta E/E \approx 10^{-7}$ for X-rays. This is

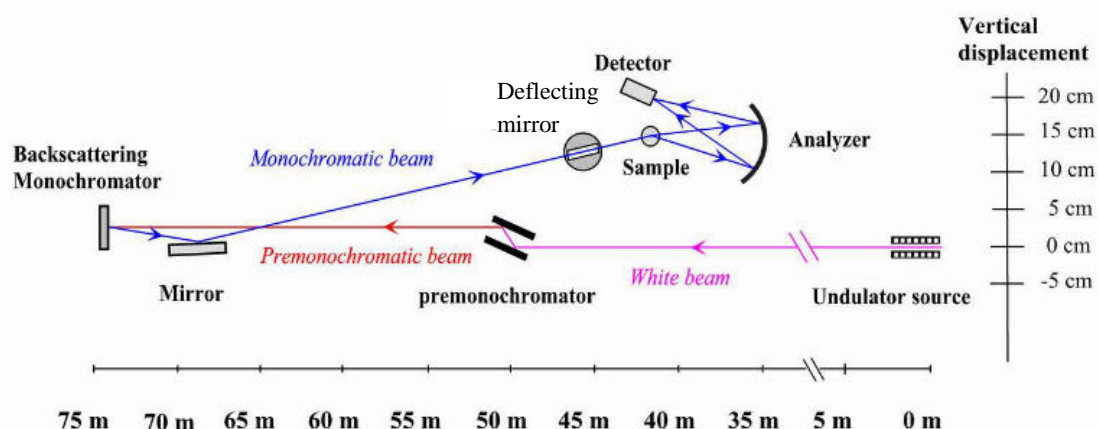


Figure 7-1 Schematic layout of the ID28 inelastic X-ray scattering beamline at the ESRF. For our experiment the incoming X-ray beam was deflected by a mirror in order to achieve grazing incidence geometry (after Ref. 92).

very demanding and requires a special set-up. The high energy resolution is obtained using a backscattering monochromator and analyser crystals also in backscattering condition. Typically, high-order hhh reflections of a Si(111) monochromator are used. We carried out a surface sensitive inelastic scattering experiment on beamline ID28, ESRF (Figure 7-1).

As presented in chapter 2, 2H-NbSe₂ is a quasi-two-dimensional material and displays a Peierls distortion resulting in a charge density wave phase transition at 33.3 K. This transition has been the subject of previous neutron and X-ray studies and is observed to be of second order within experimental accuracy^{1,7}. Using inelastic neutron scattering, Moncton *et al.*¹ measured the room temperature bulk phonon dispersion curve for NbSe₂. They observed a phonon softening of the Σ_1 mode at the charge density wave satellite position in Q -space. Ayache *et al.* have observed a complete mode softening at the CDW phase transition in the bulk⁷. Calculations of the dispersion curve of 2H-NbSe₂ are found in Wakabayashi *et al.*⁹³ who modelled the two dimensional Kohn anomaly in NbSe₂ and Motizuki *et al.*⁹⁴ who reported a theoretical study of 2H-TaSe₂ and 2H-NbSe₂ lattice dynamics and phonon anomalies (see Figure 7-4).

Previously bulk inelastic X-ray scattering has been used to study both lattice phonon branches as well as a Kohn anomaly in CDW-systems like K_{0.3}MoO₃ and NbSe₃^{78,95}. For NbSe₂ the surface behaviour is of interest as elastic grazing incidence X-ray diffraction measurements at ESRF and HASYLAB⁵¹ have shown that the surface of 2H-NbSe₂ exhibits a modified behaviour with respect to the bulk (see also chapter 6). We have observed that the transition on the surface occurs about 1.6 K above that of the bulk. The data are consistent with the occurrence of a ‘surface’ transition^{9,10,11,46}. In addition, Brillouin light scattering measurements have indicated the presence of a possible surface phonon⁹⁶. In order to dismantle the dynamics of the phase transition at the surface a direct method of investigating the phonon behaviour is required. Electron energy loss spectroscopy and Helium atom scattering spectroscopy are purely surface sensitive techniques to measure phonons.⁹⁷ Inelastic X-ray scattering carried out at grazing incidence provided a unique opportunity to investigate the mode softening at the surface of 2H-NbSe₂ and relate it directly to that of the bulk of the same sample.

Considering distorted-wave Born approximation (DWBA) calculations of penetration depth and absorption effects, a factor of 5 is lost in moving from a classical bulk geometry to GID geometry⁹⁸. We allowed for additional losses due to sample mosaicity and instrumental effects in the estimates. Thus based on test measurements on ID28⁹⁹ and our previous experience on other beamlines, we expected a count rate of the order of 0.25 Hz. With an experimental background rate of typically 10⁻² Hz at ID28, this new experiment was considered to be feasible with careful surface alignment.

7.2 Experimental method

These first grazing incidence geometry phonon measurements were performed on the inelastic scattering beamline ID28 at the ESRF. A total flux of 6×10^{10} ph/s (at 200 mA) is available with an instrumental energy resolution of 5.5 meV with a beam size of $60 \mu\text{m} \times 120 \mu\text{m}$. This resolution is provided by the Si 888 backscattering reflection at a photon energy of 15.816 keV. Ideally for the investigation of phonons one would choose a higher resolution. In this case in order to prove the principle we relaxed the resolution in order to maximise the flux. The same single crystal 2H-NbSe₂ sample that was measured using GID (chapters 4, 5), 1 mm thick and with a surface area of $4 \times 8 \text{ mm}^2$, was mounted horizontally in a vacuum chamber. At 15.816 keV the critical angle of NbSe₂ total external reflection is 0.18° . It was possible to achieve grazing incidence geometry, i.e. measure below the critical angle α_c , by inserting a silicon mirror on ID28 before the sample to deflect the primary beam downwards.

Using it in combination with the sample ϕ rotation, an incidence angle and exit angle of 0.18° providing a penetration depth of $\sim 23 \text{ \AA}$ was achieved and hence surface sensitivity. The slits before the sample were closed to $60 \mu\text{m}$ vertically in order to reduce background. The surface alignment was complicated by the beamline design. As the only slits after the sample were the analyser slits, a combination of placing diodes in the beam path and varying the analyser slit openings was used in order to achieve a surface alignment. Following an open-slit reflectivity to determine the critical angle, the sample was oriented at $\alpha_c - 0.027^\circ$. This small change of angle was chosen so that we remained below the critical angle, but still benefited from the enhancement in the transmission function close to α_c as discussed in section 4.4. In this orientation the 200 surface reflection was aligned and constant- q scans on the longitudinal acoustic branch propagating along $(h, 0, 0)$ were carried out at room temperature. h was varied over the range 1.95 to 1.6 scanning an energy range of ± 30 meV for $(1.95, 0, 0)$ and $(1.9, 0, 0)$ and ± 40 meV for the rest of the data. The data were collected with the standard analyser opening of $20 \times 60 \text{ mm}^2$ (H x V) providing a q resolution of about $\Delta q = 0.0216 \text{ \AA}^{-1}$. The data are shown in Figure 7-2 (right). We also measured the bulk phonon spectra at room temperature for comparison in order to develop our understanding of the dynamics of this very interesting system (Figure 7-2 left) and to be more sensitive to eventual changes. For the bulk data a thin layer of the sample ($\sim 12 \mu\text{m}$) was cleaved onto Scotch tape and measured in transmission geometry. The transmission was 60% of the primary beam which is optimal for a transmission measurement. Due to the unstable nature of the Scotch tape as a substrate the sample rocking curve width was measured to be 0.1° . Steps from individual terraces about 1 mm apart were observed when the sample was translated in the beam. The sample was aligned within one of these broad terraces.

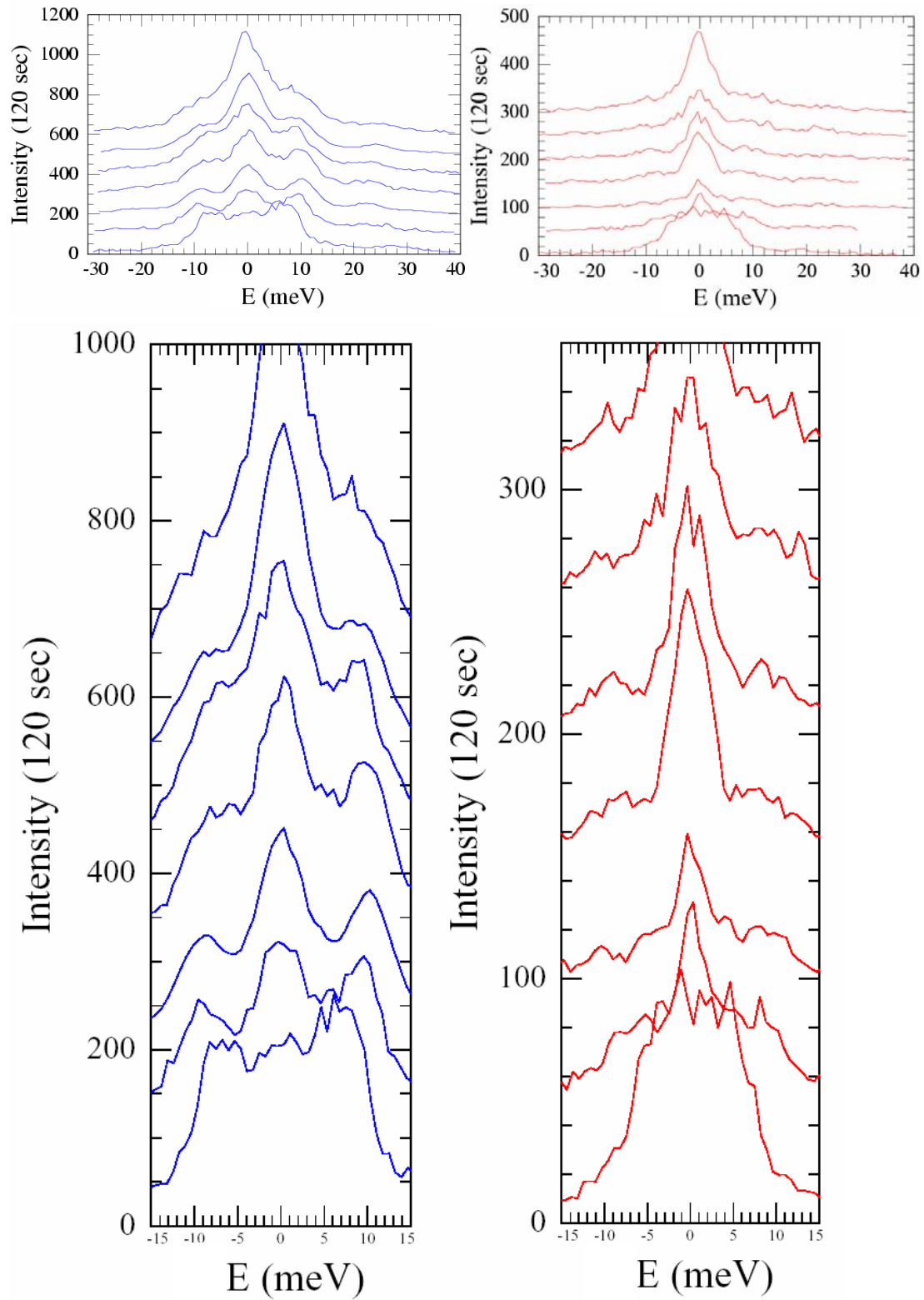


Figure 7-2: Bulk (left) and surface (right) IXS spectra of 2H-NbSe₂, measured on ID28, ESRF. The plots show data collected along the longitudinal acoustic phonon branch in the range 1.9,0,0 to 1.5,0,0 (bulk) and 1.95,0,0 to 1.6,0,0 (surface; from bottom to top).

7.3 Results

We were successful in obtaining the first grazing incidence inelastic X-ray scattering data. In this experiment we showed that it is possible to measure surface phonons with X-rays. The data have been fitted using a damped harmonic oscillator to describe the energy resolution profile. The fit of the spectrum taken at $h=1.67$ is shown in Figure 7-3.

We have observed the Σ_1 modes ω_1 and ω_2 as reported by Moncton *et al.*² and in addition optical bands at higher energy as predicted in the theoretical calculations of Motizuki *et al.*⁹⁴ (see Figure 7-4). We have obtained the surface and the bulk dispersion curve of 2H-NbSe₂ by using grazing incidence inelastic X-ray scattering for the first time (Figure 7-5).

This data shows that inelastic grazing incidence inelastic X-ray scattering is feasible at a high flux beamline such as ID28, on a modern third generation synchrotron source.

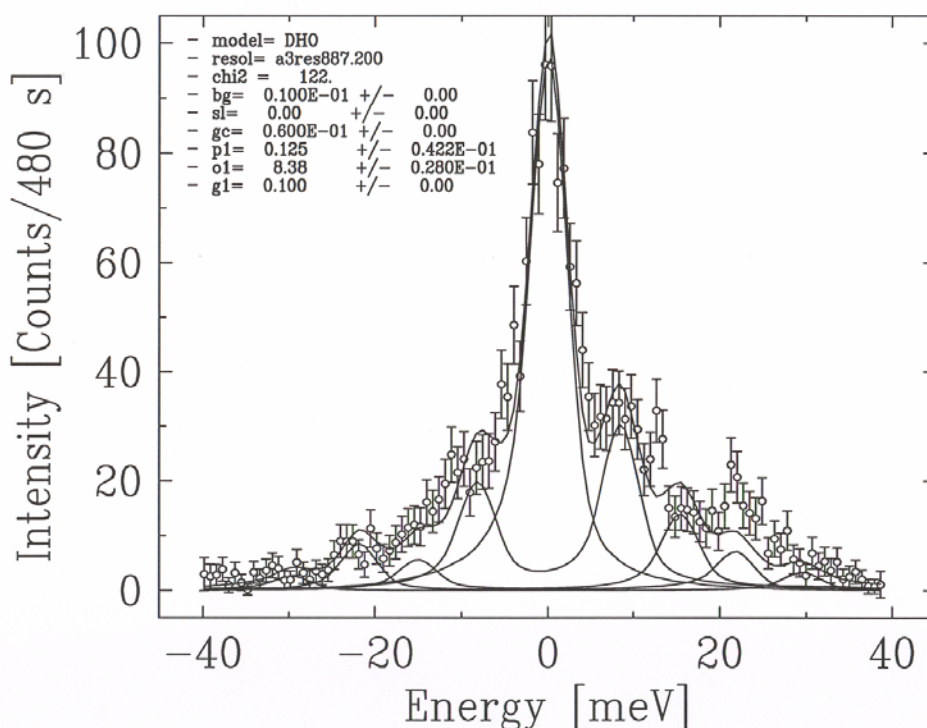


Figure 7-3 IXS spectrum of 2H- NbSe₂ taken at $h=1.67$ on ID28, ESRF. The data have been fitted using a damped harmonic oscillator to describe the energy resolution profile. The fit shown includes convolution with the measured energy resolution profile (width ~ 4.4 meV).

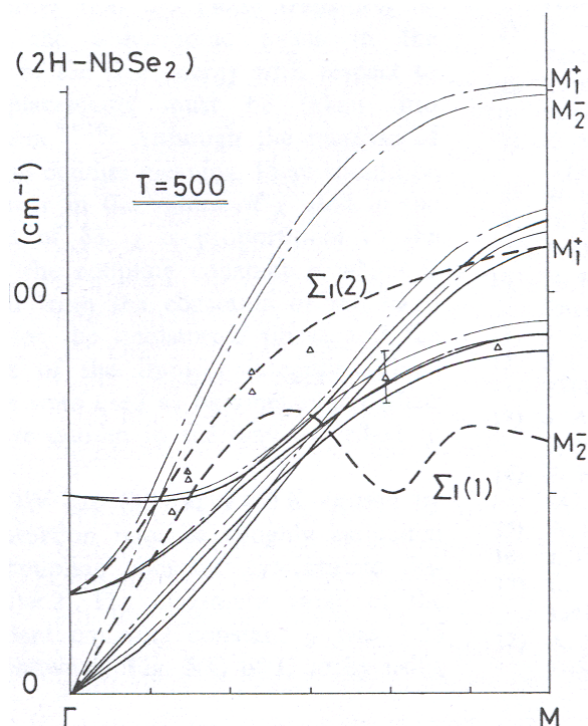


Figure 7-4 The phonon dispersion curve along the ΓM line for $2H-NbSe_2$ at 500 K according to Motizuki *et al.*⁹⁴. Dashed represent the dispersion curves for the Σ_1 modes and solid curves the other modes. These have been calculated using the rigid ion model and by taking account of susceptibility i.e. considering ion-ion interactions caused by electron-lattice interaction. The dot-dashed line shows the dispersion curves calculated by the rigid ion model. The $^{2/3} \Gamma M$ is equivalent to $q = 1.67, 0, 0$.

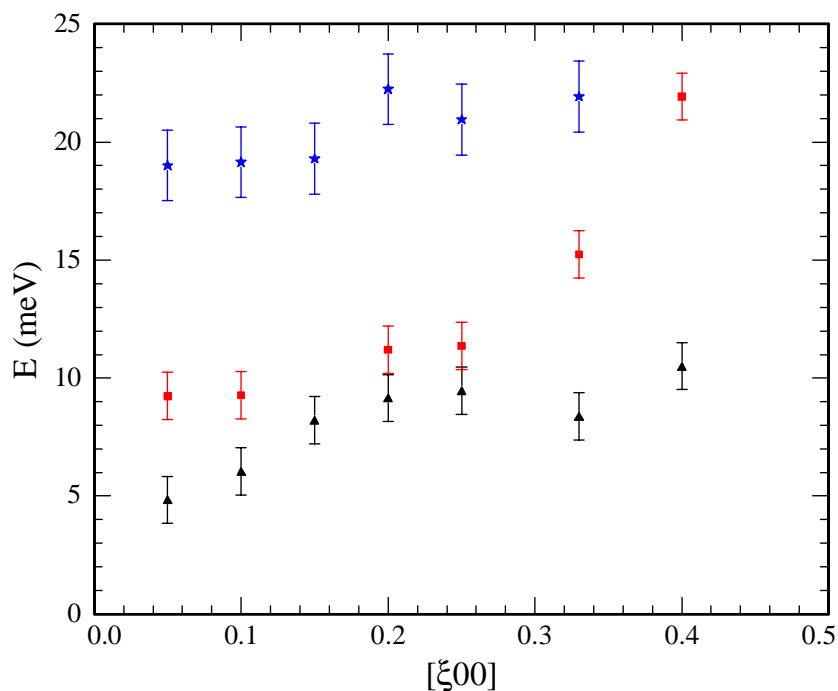


Figure 7-5: Preliminary surface room temperature dispersion curve of $2H-NbSe_2$, as obtained by means of IXS on ID28, ESRF. $\xi = 2 - h$ in reciprocal space units. The errors in the fits are of the order of 1 meV.

8 Conclusions and outlook

The objective of this thesis is to improve the understanding of the role that the surface plays in phase transitions, in particular in the case of layered materials. The quasi two-dimensional transition metal dichalcogenide NbSe₂ was chosen because it undergoes a charge density wave transition. This occurs as a result of a strong electron correlation brought about by the anisotropic structure of NbSe₂. In order to unravel the properties of this transition we used the surface sensitive technique of grazing incidence X-ray diffraction. We isolated the surface charge density wave structure on a high-quality single crystal. Measurements with an X-ray beam impinging at an angle both above and below the critical angle of total external reflection were performed in order to carry out a direct comparison between the surface and bulk behaviour. There is a great amount of theory describing phase transitions in half-infinite systems. This is both useful for guidance during experiment and for analysing the final results.

In this thesis, the quality of the samples turned out to be a central issue, and it was only after a time-consuming search and extensive testing that an appropriate 2H-NbSe₂ sample was found. Even then, well below the transition, the long-range order describing the static CDW modulation does not exceed a coherence length of ~ 800 Å. This is due to defects in the crystal, particularly stacking faults and – related to the latter – the occurrence of different polytypes.

The central finding of this thesis is that the charge density wave transition at the surface occurs at a higher temperature than in the bulk, with T_{cs} (1.6 ± 0.4) K above T_{cb} . We observe that the behaviour of the surface CDW differs from that of the bulk. In addition the transition appears to be continuous. It is likely that we observe the unusual case defined as a “surface transition” and not the usual case of an “ordinary transition”.

Grazing incidence diffraction on superstructures is experimentally difficult as superstructures often provide low-intensity reflections, as is the case for the charge density wave superstructure in NbSe₂. In order to confirm this result which has the restriction of limited counting statistics – particularly due to the very small available

sample area – the experiment was repeated several times and carried out at different instruments.

In order to further characterise the phase transition the critical exponents for the CDW transition of NbSe₂ were determined. In our earlier experiments the errors were too large for a meaningful discussion. From the final measurements at ESRF beamline ID1 we found bulk β_b to be 0.175 ± 0.02 which is between the value of 0.125 predicted for a two-dimensional system Ising model and that of 0.33 for a three-dimensional Ising-like bulk transition (mean field theory predicts 0.5). This value is also close to that one finds if there is a first order component present so we cannot rule out this possibility from our data completely. However, we do observe an increase in short range correlation length close to T_{cb} which is a trait of a continuous transition. The surface exponent $\beta_{l,e}$ was determined with respect to the bulk transition temperature, giving the ‘extraordinary transition’ exponent. We obtained a value of 0.20 ± 0.04 from our data which within the error bars agrees with the value of 0.175 predicted for the ‘extraordinary transition’ of the Ising model. In a further attempt to unravel the surface dynamics we followed the discussion of Diehl¹⁰ and as further outlined by Landau and Binder¹². Our surface data behaves as expected for an extraordinary transition indicating that the bulk is ordering in the presence of an already ordered surface. This finding is in agreement with the presence of a ‘surface transition’ for the CDW critical point at the NbSe₂ surface. Indeed, the difference between the two transition temperatures is very small. It is thus difficult to isolate the characteristic features of a surface transition. This limited our ability to determine the ‘surface transition’ exponent $\beta_{l,s}$. We extracted a value of 0.5 ± 0.3 from our data. The Ising theory predicts a value of 0.125 for a ‘surface transition’.

In the course of our study of the charge density wave structure we considered it would also be useful to measure the phonon behaviour directly at the surface. Previously, X-ray and neutron inelastic scattering techniques have been restricted to bulk studies due to a lack of flux and the complexity of achieving a grazing incidence geometry at an inelastic scattering beamline. With some modifications to the ID 28 beamline at the ESRF synchrotron source and a specially developed alignment process, we have successfully proved the feasibility of inelastic grazing incidence X-ray scattering and thus measured surface phonons in NbSe₂ in a depth of ~ 23 Å. Two transverse acoustic modes were observed and also some optical bands at higher energy. As a result of these test measurements there are plans to modify ID28 for future surface experiments. Also, the technique of grazing incidence INX has been included as part of the scientific case for the proposed IXS beamline on PETRA III, DESY¹⁰⁰.

For the future study of phase transitions especially at surfaces, both high resolution and high intensity are required in an X-ray scattering experiment. For layered crystals

the available effective sample size is restricted due to sample mosaicity, therefore, the small beam size and brilliance delivered by a high resolution beamline on new synchrotron sources such as PETRA III at DESY could provide new opportunities in the study of phase transitions at surfaces and interfaces. The treatment of phase transitions at surfaces by Dietrich and Wagner⁹, Binder¹¹ and Diehl¹⁰ and others is yet to be fully verified experimentally. More recent theory papers such as Landau *et al.*^{12,13} reiterate the importance of being able to measure as close to the critical temperature as possible in understanding critical behaviour at the surface. A combination of improved surface quality of the crystals and improved flux enhancements limitations will allow access to regions much closer to the critical transition temperature.

References

- ¹ D.E. Moncton, J.D. Axe, F. J. DiSalvo, Phys. Rev. Lett. **34**, 732 (1975)
- ² D.E. Moncton, J.D. Axe, F. J. DiSalvo, Phys. Rev. B **16**, 801 (1977)
- ³ C.-H. Du, W.J. Lin, Y. Su, B.K. Tanner, P.D. Hatton, D. Casa, B. Keimer, J. P. Hill, C.S. Oglesby, H. Hohl, J. Phys.: Condens. Matter **12**, 5361 (2000)
- ⁴ T. Straub, T. Finteis, R. Claessen, P. Steiner, S. Hufner, P. Blaha, C.S. Oglesby, E. Bucher, Phys. Rev. Lett. **82**, 4504 (1999)
- ⁵ Y. Yokoya, T. Kiss, A. Chainani, S. Shin, M. Nohara, H. Takagi, Science **294**, 2518 (2001)
- ⁶ K. Rossnagel, O. Seifarth, L. Kipp, M. Skibowski, D. Voß, P. Krüger, A. Mazur, J. Pollmann, Phys. Rev. B **64**, 235119 (2001)
- ⁷ C. Ayache, R. Currat, P. Molinié, Physica B **180**, 333 (1992)
- ⁸ X.-M. Zhu, R. Moret, H. Zabel, I.K. Robinson, E. Vlieg, R.M. Fleming, Phys. Rev. B **42**, 8791 (1990)
- ⁹ S. Dietrich, H. Wagner, Phys. Rev. Lett. **51**, 1469 (1983)
- ¹⁰ H.W. Diehl: in “Phase transitions and critical phenomena”, Vol. 10, edited by C. Domb and J.L. Lebowitz, Academic Press, London (1986)
- ¹¹ K. Binder: in “Phase transitions and critical phenomena”, Vol. 8, edited by C. Domb and J.L. Lebowitz, Academic Press, London (1983)
- ¹² D.P. Landau, K. Binder, Phys. Rev. B **41**, 4786 (1990)
- ¹³ A. Milchev, M. Müller, K. Binder, D.P. Landau, Phys. Rev. Lett. **90**, 136101 (2003)
- ¹⁴ H. Dosch, Phys. Rev. B **35**, 2137 (1987)
- ¹⁵ B. Burandt, W. Press, S. Haussühl, Phys. Rev. Lett. **71**, 1188 (1993)
- ¹⁶ H. Reichert, P.J. Eng, H. Dosch, I.K. Robinson, Phys. Rev. Lett. **78**, 3475 (1997)
- ¹⁷ H. Dosch, L. Mailänder, H. Reichert, J. Peisl, R. L. Johnson, Phys. Rev. B **43**, 13172 (1991)
- ¹⁸ H. Reichert, O. Klein, O. Shchyglo, A. Udanskyy, H. Dosch, K.F. Peters, Phys. Rev. Lett. **90**, 185504 (2003)
- ¹⁹ A. Meerschaut, C. Deudon, Mat. Res. Bull. **36**, 1721 (2001)
- ²⁰ Y. Paltiel, E. Zeldov, Y. Myasoedov, M. L. Rappaport, G. Jung, S. Bhattacharya, M.J. Higgins, Z.L. Xiao, E.Y. Andrei, P. L. Gammel, D. J. Bishop, Phys. Rev. Lett. **85**, 3712 (2000)
- ²¹ H. Katzke, Z. Kristallogr. **217**, 127 (2002)
- ²² T. Shimada, H. Nishikawa, A. Koma, Y. Furukawa, E. Arakawa, K. Takeshita, T. Matsushita, Surf. Sci. **369**, 379 (1996)
- ²³ J.A. Wilson, A.D. Yoffe, “Transition metal dichalcogenides”, Adv. Phys. **18**, 193 (1969)
- ²⁴ O. Seifarth, A. Haiskanen, measured on University of Oulo (Finland) apparatus, unpublished
- ²⁵ R.E. Thorne, Phys. Today, May 1996, 42

-
- ²⁶ G. Gruner, *Rev. Mod. Phys.* **60**, 1129 (1988)
- ²⁷ R.E. Peierls, “Quantum theory of solids”, Oxford University Press, New York, London (1955)
- ²⁸ T. Straub, R. Claessen, T. Finteis, P. Steiner, S. Hüfner, C. S. Oglesby, E. Bucher, *Physica B* **259-261**, 981 (1999)
- ²⁹ P. Mallet, W. Sacks, D. Roditchev, D. Defouorneau, J. Klein, *J. Vac. Sci. Technol. B* **14**, 1070 (1996)
- ³⁰ A. V. Skripov, D. S. Sibirtsev, Y. G. Cherepanov, B. A. Aleksashin, *J. Phys.: Condens. Matter* **7**, 4479 (1995)
- ³¹ A.W. Overhauser, *Phys. Rev. B* **3**, 3171 (1970)
- ³² S.H. Pan, E.W. Hudson, J.C. Davis, *Appl. Phys. Lett.* **73**, 2992 (1988)
- ³³ W. Sacks, D. Roditchev, J. Klein, *Appl. Phys. A* **66**, S925 (1998)
- ³⁴ G.P.E.M. Van Bakel, J.T.M. De Hosson, *Phys. Rev. B* **46**, 2001 (1992)
- ³⁵ W.L. McMillan, *Phys. Rev. B* **14**, 1496 (1976)
- ³⁶ H. Dosch, “Critical Phenomena at surface and interfaces”, Springer Tracts in Modern Physics **126**, Springer Verlag, Heidelberg (1992)
- ³⁷ C.B.P. Finn, “Thermal Physics”, Routledge and Kegan Paul, London, Boston, Henley (1986)
- ³⁸ C. Kittel, “Introduction to Solid State Physics”, 7th ed., John Wiley and Sons, Inc., New York, Chichester, Brisbane, Toronto, Singapore (1996)
- ³⁹ C. Kittel, H. Kroemer, “Thermal Physics” 2nd ed., W.H. Freeman and Company, New York (1980)
- ⁴⁰ L.D. Landau, E.M. Lifshitz, “Statistical Physics”, Vol. 5 of “Course of Theoretical Physics”, Pergamon Press, London, Paris (1958)
- ⁴¹ H. Eugene Stanley, “Introduction to phase transitions and critical phenomena”, Oxford Science Publications, Oxford University Press, New York, Oxford (1987)
- ⁴² E.K.H. Salje, “Phase transitions in ferroelastic and co-elastic crystals”, Student ed., Cambridge Topics in Mineral Physics and Chemistry, Cambridge University Press (1993)
- ⁴³ B. Burandt, PhD thesis, Kiel (1997)
- ⁴⁴ H.W. Diehl, *Essener Unikat* **11**, 80 (1999)
- ⁴⁵ A.J. Bray, M.A. Moore, *J. Phys. A* **10**, 1927 (1977)
- ⁴⁶ T. C. Lubensky, M. H. Rubin, *Phys. Rev. B* **11**, 4533 (1975)
- ⁴⁷ C.N. Yang, *Phys. Rev.* **85**, 808 (1952)
- ⁴⁸ M. Moore, M. Golshan, G. Kowalski, J. Reid, S. Collins, B. Murphy, *J. Phys. D* **32**, A37 (1999)
- ⁴⁹ J.P. Abrahams, A.G.W. Leslie, R. Lutter, J.E. Walker, *Nature* **370**, 621 (1994)
- ⁵⁰ K. Takada, H. Sakurai, E. Takayama-Muromachi, F. Izumi, R.A. Dilanian, T. Sasaki, *Nature* **422**, 53 (2003)
- ⁵¹ B.M. Murphy, J. Stettner, M. Traving, M. Sprung, I. Grotkopp, M. Müller, C.S. Oglesby, M. Tolan, *W. Press, Physica B* **336**, 103 (2002)

-
- ⁵² C. Kumpf, O. Bunk, J. H. Zeysing, Y. Su, M. Nielsen, R.L. Johnson, R. Feidenhans'l, and K. Bechgaard, *Phys. Rev. Lett.* **85**, 4916 (2000)
- ⁵³ E. Dudzik, A.G. Norris, R. McGrath, G. Charlton, G. Thornton, B. Murphy, T. S. Turner, D. Norman, *Phys. Rev. B* **58**, 12659 (1998)
- ⁵⁴ B.E. Warren, "X-ray Diffraction", Dover Books on Physics and Chemistry, Dover, New York (1990)
- ⁵⁵ O.H. Seeck, PhD thesis, Kiel (1997)
- ⁵⁶ E. Vlieg, PhD thesis, Leiden (1988)
- ⁵⁷ I.K. Robinson, D.J. Tweet, *Rep. Prog. Phys.* **55**, 599 (1992)
- ⁵⁸ M. v. Laue, *Ann. Phys.* **26**, 55 (1936)
- ⁵⁹ I.K. Robinson, *Phys. Rev. B* **38**, 3632 (1988)
- ⁶⁰ I.K. Robinson, *Phys. Rev. B* **33**, 3830 (1986)
- ⁶¹ M. Müller, Diploma thesis, Kiel (1992)
- ⁶² M. Tolan, "X-Ray Scattering from Soft -Matter Thin Films", Springer Tracts in Modern Physics **148**, Springer Verlag, Berlin, Heidelberg (1999)
- ⁶³ M.D. Foster, *Crit. Rev. Anal. Chem.* **24**, 179 (1993)
- ⁶⁴ "X-ray and Neutron Dynamical Diffraction – Theory and applications", NATO ASI Series, Series B: Physics, **357**, Plenum Press, New York, London, edited by A. Authier, S. Lagomarsino, B.K. Tanner (1996)
- ⁶⁵ "International Tables for Crystallography", edited by A.J.C. Wilson, Kluwer Academic, Dordrecht, Boston, London (1992)
- ⁶⁶ L.G. Parratt, *Phys. Rev.* **95**, 359 (1954)
- ⁶⁷ S. Dietrich, *Physica A* **168**, 160 (1990).
- ⁶⁸ I.K. Robinson, "Handbook on Synchrotron Radiation", Vol.3, edited by G. Brown (1991)
- ⁶⁹ M. Born, E. Wolf, "Principles of optics", 5th ed., Pergamon, New York (1986)
- ⁷⁰ R. Feidenhans'l, *Surf. Sci. Rep.* **10**, 105 (1989)
- ⁷¹ C.S. Oglesby, E. Bucher, K. Kloc, H. Hohl, *J. Cryst. Growth* **137**, 289 (1994)
- ⁷² G. Margaritondo, *J. Synchrotron Rad.* **2**, 148 (1995)
- ⁷³ P. Duke, "Introduction to synchrotron radiation: Production and properties", Oxford University Press (2000)
- ⁷⁴ S.D. Brown, L. Bouchenoire, D. Bowyer, J. Kervin, D. Laundry, M.J. Longfield, D. Mannix, D. F. Paul, A. Stunault, P. Thompson, M.J. Cooper, C.A. Lucas, W.G. Stirling, *J. Synchrotron Rad.* **8**, 1172 (2001)
- ⁷⁵ W. Drube, H. Schulte-Schrepping, H.-G. Schmidt, R. Treusch, G. Materlik, *Rev. Sci. Instrum.* **66** (1995) 1668
- ⁷⁶ H. Schulte-Schrepping, J. Heuer, B. Hukelmann, *J. Synchrotron Rad.* **5**, 682 (1998)
- ⁷⁷ S. Lequien, L. Goirand, F. Lesimple, *Rev. Sci. Instrum.* **66**, 1725 (1995)
- ⁷⁸ H. Requardt, J.E. Lorenzo, P. Monceau, R. Currat, M. Krisch ., *Phys. Rev. B* **66**, 214303 (2002)

-
- ⁷⁹ S. Antoranz Contera, T. Yoshinobu, H. Iwasaki, K. Kisoda, S. Nakashima, *Appl. Surf. Sci.* **130-132**, 623 (1998)
- ⁸⁰ R.L. Johnson, J.H. Fock, I.K. Robinson, J. Bohr, R. Feidenhans'l, J. Als-Nielsen, M. Nielsen, M. Toney, in: "The structure of surfaces", edited by M.A. Van Howe, S.Y. Tong, Springer, Berlin (1985)
- ⁸¹ W. Press, A. Hüller, in "The Plastically Crystalline State: Orientationally Disordered Crystals", edited by J.N. Sherwood,; John Wiley and Sons, Inc., New York (1979)
- ⁸² D. Mannix, ESRF, Grenoble, France, private communication
- ⁸³ M. Marynowski, F. Franzen, M. El-Batanouny, V. Staemmler, *Phys. Rev. B* **60**, 6053 (1999)
- ⁸⁴ S. Krimmel, W. Donner, B. Nickel, H. Dosch, C. Sutter, G. Grübel, *Phys. Rev. Lett.*, **78**, 3880 (1997)
- ⁸⁵ W. Schweika, H. Reichert, W. Babik, O. Klein, S. Engemann, A. Fattah, W. Caliebe, IFF Scientific Report 2001 / 2002
- ⁸⁶ H. Dosch, L. Mailänder, H. Reichert, J. Peisl, R.L. Johnson, *Phys. Rev. B* **43**, 13172 (1991)
- ⁸⁷ X.M. Zhu, R. Feidenhans'l, H. Zabel, J. Als-Nielsen, R. Du, C.P. Flynn, F. Grey, *Phys. Rev. B* **37**, 7157 (1998)
- ⁸⁸ B. Dorner, E. Burkel, J. Peisl, *Nucl. Instrum. Meth. A* **246**, 450 (1986)
- ⁸⁹ B. Dorner, E. Burkel, T. Illini, J. Peisl, *Z. Phys. B* **69**, 179 (1988)
- ⁹⁰ G. Fiquet, J. Badro, F. Guyot, H. Requardt, M. Krisch, *Science* **291**, 468 (2001)
- ⁹¹ F. Sette, G. Ruocco, M. Krisch, C. Masciovecchio, R. Verbeni, *Phys. Scripta* **T66**, 48 (1996)
- ⁹² <http://www.esrf.fr/UsersAndScience/Experiments/HRRS/ID28/IntroIXS/>
- ⁹³ N. Wakabayashi, H.G. Smith, R. Shanks, *Phys. Lett.* **50A**, 367 (1974)
- ⁹⁴ K. Motizuki, K. Kimura, E. Andō, N. Suzuki, *J. Phys. Soc. Jpn.* **53**, 1078 (1984).
- ⁹⁵ H. Requardt, J.E. Lorenzo, R. Danneau, R. Currat, P. Monceauet, *J. Phys. IV* **12**, Pr9-39 (2002)
- ⁹⁶ S. Mielcarek, University of Poznan, Poland, private communication
- ⁹⁷ G. Benedek, J.P. Toennies, *Surf. Sci.* **299/300**, 587 (1994)
- ⁹⁸ J. Stettner, University of Kiel, private communication
- ⁹⁹ H. Requardt, ESRF, Grenoble, France, private communication
- ¹⁰⁰ M. Müller, University of Kiel, member of PETRA III IXS beamline working group, private communication

Teile der Arbeit wurden bereits veröffentlicht:

Refereed publications

B.M. Murphy, J. Stettner, M. Traving, M. Sprung, I. Grotkopp, M. Müller, C.S. Oglesby, M. Tolan, W. Press, *Physica B* **336**, 103 (2002)

C V

Personal Information

Name: Bridget Murphy
Address: Großer Hof 14a, 24235 Laboe
Nationality: Irish
Parents: John and Cecilia Murphy
Date of Birth: 15/6/1969 Dundalk, Ireland

PROFESSIONAL EXPERIENCE

2000 -	Christian Albrechts-Universität zu Kiel	Kiel, Germany
	<i>Wissenschaftliche Angestellte</i>	
1997 - 2000	CCLRC Daresbury Laboratory	Cheshire, England
	<i>Higher Scientific Officer</i>	
1994 - 1997	CCLRC Daresbury Laboratory	Cheshire, England
	<i>Scientific Officer</i>	
1991 - 1993	Meath Hospital	Dublin, Ireland
	<i>Part-time lecturer</i>	
1991 - 1993	Dublin City University	Dublin, Ireland
	<i>Tutor and Lab demonstrator</i>	
1990 - 1990	Donnelly Mirrors	Co. Kildare, Ireland
	<i>Student Scientist</i>	

EDUCATION

1991 - 1994	Dublin City University	Dublin, Ireland
	<ul style="list-style-type: none">• MSc by research in surface science. Thesis title 'The characterisation of III-V semiconductor materials, principally InP and GaAs'. – in the group of Dr. G. Hughes	
1987 - 1991	Dublin City University	Dublin, Ireland
	<ul style="list-style-type: none">• BSc (Honours) Applied Physics.	
1981 - 1987	Presentation Convent Secondary School	Waterford, Ireland
	<ul style="list-style-type: none">• Leaving certificate	
1973 - 1981	Presentation Convent Primary School	Waterford, Ireland

Eidesstattliche Erklärung

Hiermit erkläre ich an Eides Statt, daß ich diese Arbeit selbständig unter der Beratung meiner wissenschaftlichen Lehrer und nur mit den angegebenen Hilfsmitteln erstellt habe. Diese Arbeit wurde weder ganz noch in Teilen an anderer Stelle im Rahmen eines Prüfungsverfahrens vorgelegt. Frühere Promotionsversuche wurden von mir nicht vorgenommen.

Kiel, den

.....

(Bridget Murphy)

Acknowledgements

I would like to express my thanks to Prof. Dr W. Press for his help, advice and encouragement even when the distances were large. For local supervision, and lots of help and practical advice, thank you to Jochim Stettner. For a thorough introduction to the topic I would like to thank Martin Traving.

In addition I would like to thank all the members of the Press and Müller working groups for their willing help and constructive discussion. Thanks to Klaas Kölln, Julian Baumert, Rüdiger Weber, Wolfgang Prange, Claas Behrend, Arnd Seeger, Karin Griewatsch, Frau Seeger and Frau Müller-Puffe. In addition a special heartfelt thanks those who helped at the many beamtimes, especially Ingo Grotkopp, Martin Müller and again Jochim Stettner who have passed many weeks at the synchrotron in order to help me, and to the all the others who have part taken in beamtimes, Michael Sprung, Metin Tolan, Timo Kurbjuhn. Thanks to Joost Jakobs for setting up the cryostat.

For the super NbSe₂ sample and enlightening discussion I thank Peter Hatton especially given that I did not go to Durham. Thanks also to the members of the Skibowski /Kipp group for supplying samples and updates from the photoemmission world, in particular Olaf Seifarth and Christian Kreis.

At HASYLAB I would like to thank Oliver Seeck for his support in W1 and for many useful tips and bits of essential equipment. I would like to thank Robert Johnson for letting us use his baby chamber and for his collaboration. For assistance with the BW2 diffractometer and the TASCOCOM control system thanks to Oliver Bunk and Robert Feidenhans'l. Thanks also to Wolfgang Drube and Horst Schulte-Schrepping for setting up the BW2 beamline.

At the ESRF I would like to say thanks to the beamline staff of ID1, BM28 and ID28. Especially thanks to Peter Bösecke and Danny Mannix for their skills as local contact and to Herwig Requardt for his preparations and the fruitful collaboration on the grazing incidence inelastic X-ray scattering measurements. Thanks also to Till Metzger, Chris Lucas, Paul Thomson, Simon Brown and to Michael Krisch.

Thanks to Alfred Hüller and Hans Werner Diehl for theoretical guidance and discussion.

For encouraging me to take the plunge in the first place I am indebted to the following of my colleagues and friends at Daresbury SRS: Graham Bushnell-Wye, Steve Collins, David Norman, Tracy Turner, Steve Bennet and Elizabeth McLean.

For funding I would like to thank the DFG “Forschergruppe”, and for the experimental beamtime the director of HASYLAB and of the ESRF.